Functional and Structural Studies on Interactions of the Leukocyte Integrin $\alpha_M\beta_2$ with Cationic Ligands

by

Di Shen

A Dissertation Presented in Partial Fulfillment
of the Requirements for the Degree
Doctor of Philosophy

Approved January 2020 by the
Graduate Supervisory Committee:

Xu Wang, Chair
Jeff Yarger
Wade Van Horn

ARIZONA STATE UNIVERSITY

May 2020

ABSTRACT

Integrins are a family of αβ heterodimeric transmembrane receptors. As an important class of adhesion receptors, integrins mediate cell adhesion, migration, and transformation through bidirectional signaling across the plasma membrane. Among the 24 different types of integrins, which are notorious for their capacity to recognize multiple ligands, the leukocyte integrin $\alpha_M\beta_2$ (Mac-1) is the most promiscuous member. In contrast to other integrins, Mac1 is unique with respect to its preference for cationic ligands. In this thesis, a new Mac-1 cationic ligand named pleiotrophin (PTN) is uncovered. PTN is an important cytokine and growth factor. Its activities in mitogenesis and angiogenesis have been extensively researched, but its function on immune cells was not widely explored. In this research, the cell biology and biochemical evidences show that PTN can regulate various Mac-1-expressing cells functions through the activation of the extracellular signal regulated kinases. Direct interactions between PTN and the α_M I-domain, the major ligand-binding domain of Mac-1, has been shown using biolayer interferometry analyses and confirmed by solution NMR spectroscopy. The binding epitopes and the binding mechanism of PTN and α_M I-domain interaction were further revealed by peptide array analysis and microscale thermophoresis. The data suggested that PTN's thrombospondin type-1 repeat (TSR) domains and α_M I-domain metal-ion-dependent adhesion site (MIDAS) are the major binding sites. In addition, this interaction followed a novel metal-ion independent binding mechanism which has not been found in other integrins. After a series of characterizations of α_M I-domain using both experimental and computational methods, it showed that activated α_M I-domain is

significantly more dynamic than inactive α_M I-domain, and the dynamics seem to modulate the effect of Mg^{2+} on its interactions with cationic ligands. To further explore the PTN induced Mac-1 structure rearrangement, intact Mac-1 was studied by negative stain electron microscopy. The results showed that the Mac-1 exhibited a very heterogeneous conformation distribution in detergents. In contrast, the Mac-1 adopted predominantly the bent conformation in phospholipid nanodisc condition. This Mac-1 nanodisc model provides a new platform for studying intact Mac-1 activation mechanism in a more physiologically relevant manner in the future.

DEDICATION

This dissertation is wholeheartedly dedicated to my parents, my wife, my friends, and my church members who have supported me throughout the process. I deeply appreciate all their physical, emotional, spiritual support.

ACKNOWLEDGEMENTS

I would like to express the deepest appreciation to my advisor, Dr. Xu Wang for his expertise, guidance, assistance, and patience throughout all these years. Without his mentorship, this work would not be possible. Beyond the things that I learned from him how to be a structural biologist, I have learned to be honest, be patient and be curious which will benefit me for my entire life. I also extremely appreciated the chances that he provided me to collaborate with so many other talented scientists from different groups. These collaborations definitely broadened my view and enriched my skills. Second, I would like to thank my committee members, Dr. Jeff Yarger and Dr. Wade Van Horn for their support, advising and guidance in my researches. Especially for Dr. Wade Van Horn, I deeply appreciate his advising in nanodisc project and the suggestions for membrane protein research.

In addition, I am deeply grateful to all my collaborators. I thank Dr. Tatiana Ugarova, Dr. Nataly Podolnikova, and Dr. Valeryi K Lishko for their kindly sharing knowledge and experiences on cell biology and training me to do the cell biology experiments. I would also thank Dr. Po-Lin Chiu and Chloe Truong for their kindly help and suggestions on integrin EM study. I thank Dr. Wei Liu and Chang Liu for their help on the crystallization of the α_M I-domain and PTN complex. I want to thank Dr. Brian Cherry and Dr. Samrat Amin from MRRC for the maintenance of NMR facilities used in the work. I would also thank Dr. Julian Chen and Dr. Dhenugen Logeswaran for their help in MST experiments.

Finally, I would like to thank my colleagues in Dr. Wang's lab. I would like to thank Dr. Wei Feng, Dr. Hanqing Deng, Eathen Ryan and Hoa Nguyen for their help on NMR experiments and protein preparation. None of this would have been possible without you.

TABLE OF CONTENTS

Page

LIST OF TABLES ix

LIST OF FIGURES x

CHAPTER

1 INTRODUCTION 1

1.1 Integrin Family and Diversity 1

1.2 Structure of Integrins 4

1.2.1 The Extracellular Domain 4

1.2.2 Transmembrane Domain and Cytoplasmic Domain 6

1.2.3 The Global Topology of Integrin 7

1.3 Integrin Activation 8

1.4 Integrins on Immune Cell 9

1.5 Integrin $\alpha_M\beta_2$ 13

1.5.1 Integrin $\alpha_M\beta_2$ Ligands 13

1.5.2 Integrin $\alpha_M\beta_2$ α I-domain 15

2 PLEIOTROPHIN, A MULTIFUNCTIONAL CYTOKINE AND GROWTH FACTOR, INDUCES LEUKOCYTE RESPONSES THROUGH THE INTEGRIN MAC-1 18

2.1 Abstract 18

2.2 Introduction 19

2.3 Materials and Methods 22

CHAPTER Page

2.4 Results 28

2.5 Discussion 49

3 THE ROLE OF α_M I-DOMAIN STRUCTURAL DYNAMICS ON ITS INTERACTIONS WITH CATIONIC LIGANDS 57

3.1 Abstract 57

3.2 Introduction 58

3.3 Materials and Methods 63

3.4 Results 69

3.5 Discussion 84

4 ELECTRON MICROSCOPY STUDIES OF FULL-LENGTH $\alpha_M\beta_2$ (MAC-1) INTERGRIN IN DETERGENT AND PHOSPHOLIPID NANODISCS 91

4.1 Abstract 91

4.2 Introduction 92

4.3 Materials and Methods 97

4.4 Results 103

4.5 Discussion 115

5 CONCLUSION AND OUTLOOK 119

5.1 Pleiotrophin Induced Leukocyte Integrin $\alpha_M\beta_2$ Functions 119

5.2 The Role of α_M I-domain Structural Dynamics in Its Interactions with Cationic Ligands 121

5.3 The Characterization of Full-length Integrin $\alpha_M\beta_2$ 122

Page

REFERENCES 125

APPENDIX

A BINDING STUDY BETWEEN PLEIOTROPHIN AND PROTEIN TYROSINE PHOSPHATASE RECEPTOR TYPE Z 141

Abstract 142

Introduction 142

Materials and Methods 147

Results 149

Discussion 153

B PERMISSION FOR TABLE 1.1 156

C PERMISSION FOR TABLE 1.2 158

D PERMISSION FOR FIGURE 1.2 160

LIST OF TABLES

Table Page

1.1 Phenotypes of Integrin Knockout Mice. 3

1.2 Distributions, Ligands, and Functions of Major Integrins in Leucocytes.....12

LIST OF FIGURES

Figure Page

1.1 Integrin Families. 2

1.2 Structure of Integrin. 6

1.3 Illustration of Integrin Activation. 8

1.4 Structure of Integrin $\alpha_M\beta_2$ α I-domain. 17

2.1 PTN Supports Adhesion and Spreading of Mac-1-expresing HEK293 Cells and IC-21 Macrophages. 30

2.2 Effect of Aggrecan on PTN-mediated Adhesion of Mac-1-expressing HEK293 Cells. 33

2.3 Migration of Mac-1-expressing Cells to PTN in a Transwell System. 35

2.4 PTN-induced Phosphorylation of Erk1/2 in Wildtype HEK293 and Mac-1-HEK293 Cells. 37

2.5 Analyses of Binding of the α_M I-domains to PTN by BLI. 40

2.6 PTN Binding to the α_M I-domain Determined From ^{1}H-^{15}N HSQC Spectra of ^{15}N-labeled PTN. 41

2.7 Screening of Peptide Library Spanning the Sequence of PTN for α_M I-domain Binding. 46

2.8 PTN Fragments Support Adhesion, Inhibit Adhesion, and Induce Erk1/2 Activation in Mac-1-expressing HEK293 Cells. 47

2.9 PTN Fragments Inhibit the Adhesion of Mac-1-HEK293 Cells to PTN in a Dose-dependent Manner. 46

Figure Page

2.10 Densitometry Analysis of Western Blot Images of Erk1/2 Phosphorylation Induced by PTN in Mac-1-HEK293 Cells. 48

2.11 Location of the α_M I-domain Binding Residues in NTD and CTD of PTN.. 56

3.1 Integrin α_M I-domain 63

3.2 The Purification of Active and Inactive α_M I-domain 70

3.3 Chromatograms from Tosho HPLC SEC Column 71

3.4 Comparison of Inactive and Active α_M I-domain ^{1}H-^{15}N HSQC Spectra..... 72

3.5 Comparison of the Root-mean-square Fluctuation (RMSF) of the Amino Acid Residues from MD Simulation Trajectories. 74

3.6 The Comparison of α7 Helix Dynamics Between Active and Inactive α_M I-domain 75

3.7 Circular dichroism (CD) Spectra and the Determination of Protein Melting Temperature (Tm) of Active and Inactive α_M I-domain 76

3.8 The Mg^{2+} Effect on Tm of Active and Inactive α_M I-domain 77

3.9 Microscale Thermophoresis of PTN with Active and Inactive α_M I-domain..... 80

3.10 Microscale Thermophoresis of PF4 with Active and Inactive α_M I-domain..... 81

3.11 Mg^{2+} Effects of PTN Binding on Active and Inactive α_M I-domain 82

3.12 Mg^{2+} Effects of PF4 Binding on Active and Inactive α_M I-domain 83

3. 13 Crystals and Diffractions of Active α_M I-domain and PTN complex 84

3.14 The Structures and Electrical Potential Surfaces of Active and Inactive α_M I-domain 90

Figure Page

4.1 Integrin Architecture....93

4.2 SDS-PAGE of 44a IgG Immunoglobulin....104

4.3 FACS of Mac-1 HEK293 with 44a Primary Antibody and Alexa Fluor 488 Secondary Antibody....106

4.4 Purification of Intact Mac-1 Integrin....108

4.5 Class Averages of Intact Mac-1....110

4.6 The MSP1D1 Construct and Its Purification....111

4.7 1D ^{1}H NMR Spectra of OG in the Presence of Bio-Beads....111

4.8 Characterization of Empty Self-assembly MSP1D1 Nanodiscs....112

4.9 Characterization of Integrin Mac-1 Nanodiscs....114

5.1 The Interaction Between PF4 and α_2 I-domain....124

A.1 Architecture of PTPRZ and the Schematic of Proposed Ligand-induced PTPRZ Dimerization....146

A.2 PTPRZ-ac Peptide....149

A.3 Titration of PTPRZ-ac Peptide with PTN....150

A.4 Titration of PTN with PTPRZ-ac Peptide....152

A.5 PTPRZ-ac Peptide Induced Chemical Shift Changes in PTN....153

A.6 Pleiotrophin Structure and Electrostatic Surface Potential....155

CHAPTER 1

INTRODUCTION

1.1 Integrin family and diversity

Integrins are a large family of αβ heterodimeric transmembrane receptors that play essential roles in metazoans. As an important class of adhesion receptor, integrins mediate cell adhesion, cell migration, and cell transformation through bidirectional signaling across the plasma membrane (outside-in signaling and inside-out signaling). In 33 years since the first characterization of integrin at a molecular level by Richard O. Hynes et.al (1), a large amount of work has been performed to elucidate integrin functions and its molecular activation mechanisms on various cells. Although tens of thousands of articles published on integrin studies, there is no unified explanation of the integrin activation mechanism because of the intricacies between different integrins, ligands, and functions.

In metazoan, there are at least 18 types of α subunits and 8 types of β subunits which assemble into 24 different αβ heterodimers in integrin superfamily as shown in Figure 1.1 (2-4). This diversity in the combination of αβ subunits contributes to diversity in ligands binding, activation mechanisms, and coupled signaling pathways, which is further manifested in diversified behaviors on biological systems. Table 1.1 shows the pathological phenotypes observed in integrin knockout mice. With the deepening and accumulation of biological studies, people gradually began to comprehend the way integrins function in different complex biological systems (3). As part of these efforts, structural data acquired form electron microscopy (EM), X-ray crystallography, and

nuclear magnetic resonance (NMR) have provided an in-depth understanding of integrin conformation, ligand binding and subsequent bidirectional signal transduction at the molecular level. With the combination of functional and structural study, it becomes possible for researches to reveal the structural derived functional changes of integrin.

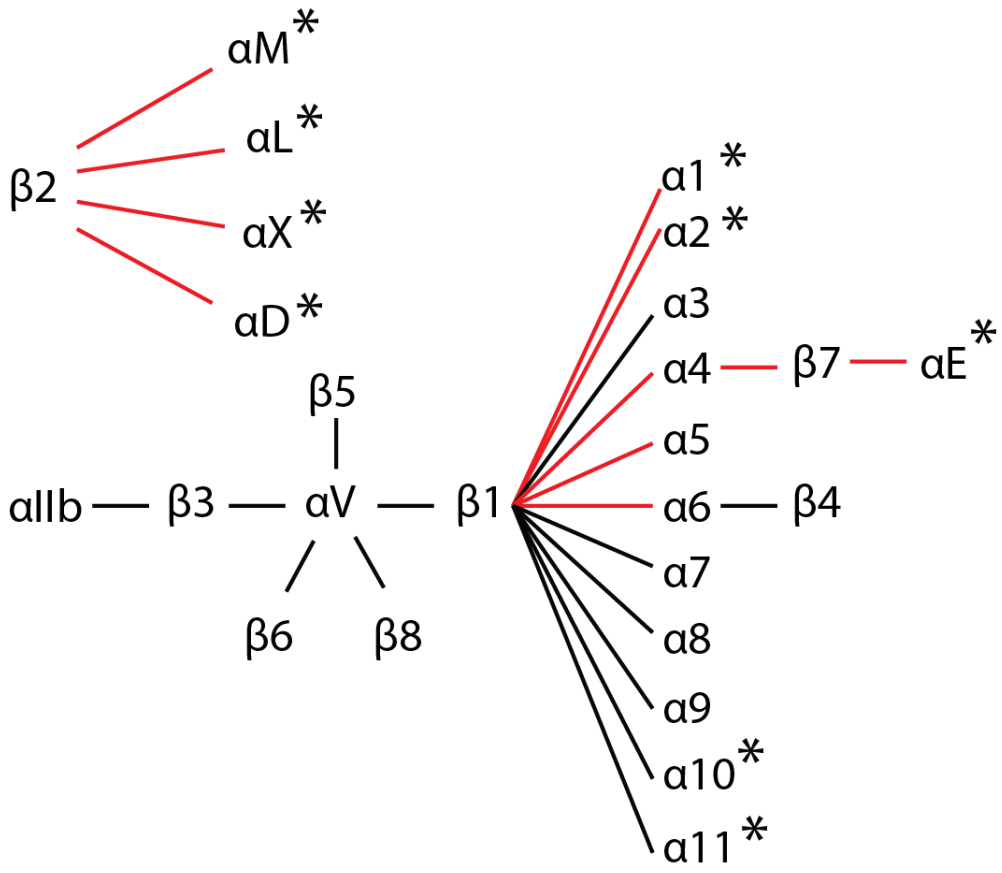

Figure 1.1 Integrin Families.

24 different integrins are composed of heterodimers of 18 types of α subunits and 8 types of β subunits. Known combinations of αβ subunits are connected by solid lines. The α subunit containing an α I-domain is asterisked. The integrins expressed on immune cells are connected with the red line.

Adapted from Bing-Hao Luo, Christopher V. Carman. (2007). Structural Basis of Integrin. Annu. Rev. Immunol, 25:619–47.

Integrin subunit	Mouse phenotype	Effects of loss	Link to human disease
α1	Viable, fertile	Defects in collagen synthesis, tumour angiogenesis, small kidneys, skin hardening	Unknown
α2	Viable, fertile	Defects in platelet adhesion, mammary ductal branching and kidney development	Unknown
α3	Perinatal lethal	Defects in kidney and lung development, skin blistering	Interstitial lung disease, nephrotic syndrome, epidermolysis bullosa
α4	Embryonic lethal	Defects in placenta formation, cardiac development and haematopoietic cell maintenance and homing	Unknown
α5	Embryonic lethal	Defects in neural crest cell survival and mesoderm formation	Unknown
α6	Perinatal lethal	Defects in brain cortex organization, skin blistering	Junctional epidermolysis bullosa with pyloric stenosis
α7	Perinatal lethal	Defects in vascular development and placenta formation, muscular dystrophy	Muscular dystrophy
α8	Perinatal lethal	Kidney defects, deafness	Unknown
α9	Perinatal lethal	Defects in lymphatic valve formation and in the development of the lymphatic system, congenital chylothorax*	Congenital chylothorax
α10	Viable, fertile	Dwarfism, mild chondrodysplasia	Unknown
α11	Viable, fertile	Dwarfism, increase mortality, defective incisor eruption	Unknown
αv	Embryonic or perinatal lethal	Defects in placenta formation and in CNS and GI blood cell development, cleft palate	Unknown
αx	Viable, fertile	T cell defects, increased susceptibility to bacterial infections	Systemic lupus erythematosus
αL	Viable, fertile	Impaired leucocyte recruitment and tumour rejection, defects in osteoclast development	Psoriasis
αD	Viable, fertile	Increased susceptibility to bacterial infections	Unknown
αM	Viable, fertile	Impaired phagocytosis and PMN apoptosis, obesity, defective mast cell development	Systemic lupus erythematosus
αE	Viable, fertile	Reduced lymphocyte numbers	Unknown
αIIb	Viable, fertile	Platelet abnormalities	Glanzmann's thrombasthenia, thrombocytopenia
β1	Embryonic lethal	Inner cell mass deterioration	Unknown
β2	Viable, fertile	Impaired leucocyte migration, skin infections, osteoporosis	LADI
β3	Viable, fertile	Platelet abnormalities, bone defects	Glanzmann's thrombasthenia, thrombocytopenia
β4	Perinatal lethal	Skin blistering	Epidermolysis bullosa
β5	Viable, fertile	No apparent phenotype	Unknown
β6	Viable, fertile	TGFβ activation defect, juvenile baldness, asthma, periodontal disease	Asthma
β7	Viable, fertile	Immunological defects	Inflammatory bowel disease
β8	Embryonic or perinatal lethal	Defects in placenta and in CNS and GI blood cell development, cleft palate	Unknown

Table 1.1 Phenotypes of Integrin Knockout Mice.
Reprinted with permission from Bouvard D, Pouwels J, De Franceschi N, Ivaska J. (2013). Integrin inactivators: balancing cellular functions in vitro and in vivo. Nat Rev Mol Cell Biol, 14(7):430-42 Copyright © 2013, Springer Nature. See Appendix B.

1.2 Structure of integrins

Integrins are composed of two non-covalently associated α and β subunits. Each subunit has a large extracellular domain, a single membrane-spanning helix and a short unstructured cytoplasmic tail (the β_4 subunit is an exception). The exact sizes of different integrins vary, but commonly α and β subunits contain approximately 1000 and 750 amino acids, respectively (5). Over the past decades, more than 400 high-resolution structures of either intact integrin or integrin domains have been published. This valuable structural data helped us gain better insights into the mechanisms of integrin regulations (2, 6-9). This thesis is mainly focused on the study of integrin's extracellular domains, especially the α I-domain on integrin $\alpha_M\beta_2$.

1.2.1 The extracellular domain

As mentioned before, integrin has a large multicomponent extracellular domain which is comprised of α and β subunits as shown in Figure 1.2 (5). Most of the high-resolution structures of integrin extracellular domains are solved by X-ray crystallography. In 2001, the first complete extracellular domain of integrin $\alpha_v\beta_3$ was published which started a deluge of structures of integrin extracellular domains (10).

The data showed that the integrin α subunit consists of a seven-bladed β-propeller domain, a thigh domain and two calf domains (10). Nine of the eighteen integrin α subunits contain an additional 200-residue I-domain, also known as a von Willebrand factor A domain connected to the β-propeller domain (11). This α I-domain plays crucial role in ligand binding and the activation of integrin when it is present. Unlike the other four domains, which have relatively rigid structures, α I-domain manifests high flexibility

in conformational changes within the domain. Ligand binding can alter the α I-domain from a closed, inactive state to an open, active conformation which that, in turn, leads to conformation changes in other parts of the integrin (12). The structure change, ligand binding and activation mechanism of α I-domain will be specifically discussed with more details in this thesis.

The β subunit has eight extracellular domains: a β I-domain, which has a similar structure as α I-domain, a hybrid domain, a plexin-semaphorin-integrin (PSI) domain, four cysteine-rich epidermal growth factor (EGF) domains, and a membrane-proximal β tail (β-T) domain. The β I-domain is homologous to the α I-domain and plays similarly important roles in ligand binding in the integrin heterodimers which lack the α I-domain (13). In these α I-less integrins, ligand binding takes places at the crevice on the head domain interface between β-propeller on the α subunit and β I-domain on the β subunit. Crystal structures suggest that these ligand binding events are dependent on divalent cations (Mg^{2+} and Ca^{2+}) coordinated by residues in MIDAS (metal-ion-dependent adhesion site) and ADMIDAS (adjacent sites MIDAS) on the β I-domain. The ligand-binding causes a structural transition of β I-domain from a "closed" to an "open" conformation along with the β I-domain α7 helix movement. This motion of α7 helix has been shown to induce a global conformation change in the whole integrin and is considered as a necessary activation step (13).

1.2.2 Transmembrane domain and the cytoplasmic domain

Because of the dynamic nature of the transmembrane domain and cytoplasmic domain, much of the structural information of those two domains is based on NMR analysis. For example, the structure of the α_{IIb}/β_3 integrin transmembrane domain was solved by solution NMR in the phospholipid bicelle model (14, 15). α_{IIb} TM domain is a 24 residue α-helix inserted perpendicularly into the membrane. And β_3 TM is a 30 residue α-helix tilted in the phospholipid membranes.

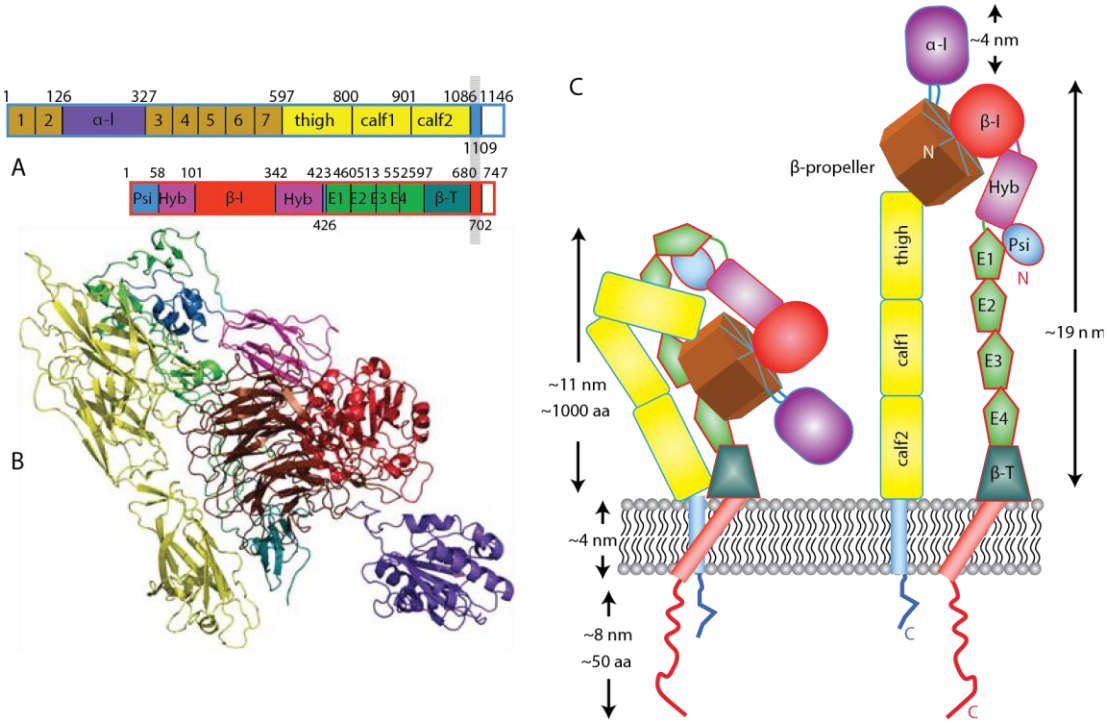

Figure 1.2 Structure of Integrin.
(A) Domain organization of $\alpha_x\beta_2$ (Xie et al. 2009); (B) structure of $\alpha_x\beta_2$ using same color scheme as A (PDB coordinates 3K6S); (C) cartoon representation of bent and upright conformations showing approximate dimensions.
Reprinted with permission from Iain D. Campbell and Martin J. Humphries. (2011). Integrin Structure, Activation, and Interactions. Cold Spring Harb Perspect Biol, 3(3): a004994. Copyright © 2011 Cold Spring Harbor Laboratory Press. See Appendix D.

The cytoplasmic domains of integrins are generally short and structure-less. They are usually only 10-70 amino acid residues in size except for the β_4 subunit, which has more than 1000 amino acid residues (Figure 1.2). Some studies show that the conserved GFFKR and HDR(R/K) E sequences of α and β subunits, respectively, may form a salt bridge which is thought to be important in the regulation of integrin activation (16, 17). Disruption of the salt bridge in β_3 integrins has been shown to alter integrin activation states (18).

1.2.3 The global topology of integrin

Since integrin must transmit information across the membrane, it is important to know how conformational information is transmitted from the extracellular domains to transmembrane domains and to the cytoplasmic domains. From the crystal structure data, such as $\alpha_x\beta_2$ shown in Figure 1.2, investigators found that the extracellular domain of the integrin adopts a severely bent "V" shape topology in which the interaction domain was closely adjacent to the membrane-proximal domain. Many studies have suggested that this bent conformation represents the inactive physiological state in which integrin exhibits low ligand binding affinity (6).

On the other hand, EM data revealed a large global conformational rearrangement of integrin's extracellular parts (19). The EM topology shows that integrin exists in at least two conformational states including bent and extended conformations (Figure1.2 C right). The extended conformation with large separation of α and β legs has been proposed as the active high ligand binding affinity state which associated with many

physiological cell functions (19). In chapter 4, we studied the conformation distribution of intact Mac-1 integrin by single-particle electron microscopy (EM).

1.3 Integrin activation

As mentioned before, the EM topology has shown that integrin exhibits different conformations representing active and inactive states. In the physiological resting state, integrin ectodomains are folded into a bent conformation with low ligand binding affinity (20). However, EM data reveal that ligand or divalent cation binding could cause the integrin conformation to change to an extended structure with high activity.

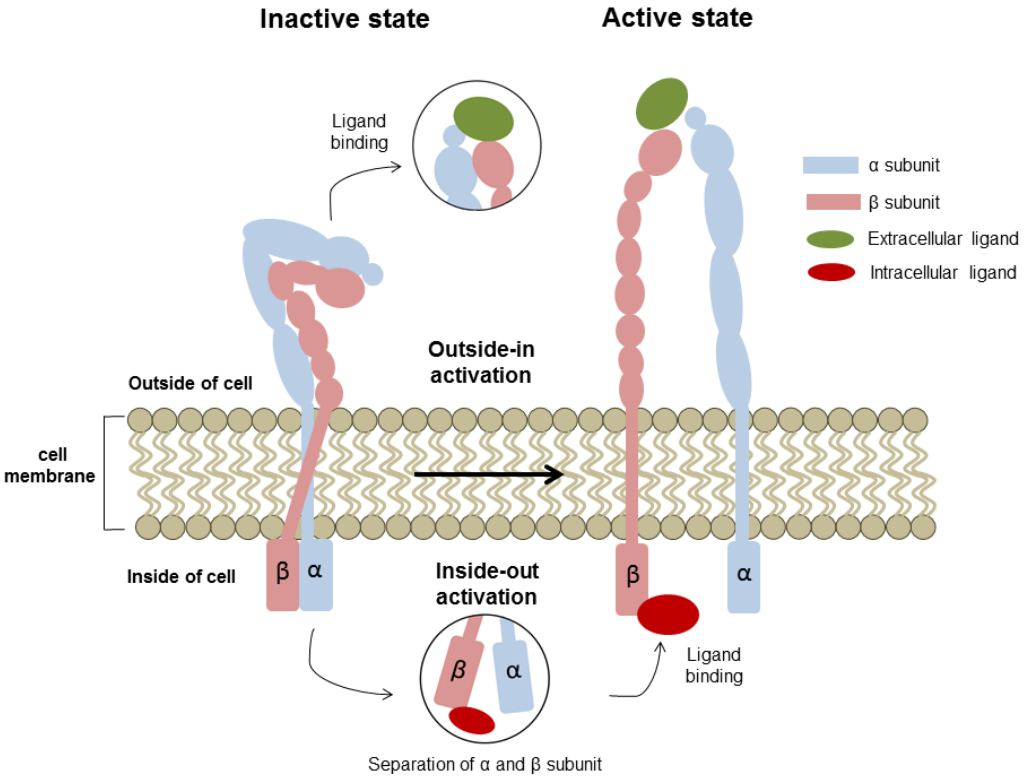

Figure 1.3 Illustration of Integrin Activation.
Integrin in bent conformation with low ligand affinity can be activated by extracellular or intracellular ligand binding and transformed into an extended active conformation through the "inside-out" and "outside-in" signaling.

These conformation changes are the key to signal transduction by integrins. In this way, integrin can transduce the signal from extracellular to intracellular through the extrinsic ligand binding in a process called “outside-in” signaling (extracellular to intracellular). Through this process, ligands bind to low-affinity bent conformer which causes a conformation rearrangement to extended conformer and transfer the signal into the cytoplasmic domain (Figure 1.3).

However, in most cases, integrins adopt a low-affinity state with respect to the extrinsic ligand and rely on intracellular signals to be activated in so called “inside-out” signaling (intracellular to extracellular). It is important that integrins are in a dormant state in physiological conditions until the injury or infection occurs. For example, integrins expressed on platelets and leukocytes, which freely circulate in the blood, are inactive until hemostasis or immunoreaction happens. This inside-out signaling is dependent on the interaction between the integrin cytoplasmic domain and intrinsic ligands such as talin (21). Talin binding directly activates integrin by separating the membrane-proximal region of α and β subunits and induces the extension of the whole integrin shown in Figure 1.3 (22).

In summary, integrin in the bent conformation with low ligand affinity can be activated by extracellular or intracellular ligand binding and transformed into an extended active conformation through the “inside-out” and “outside-in” signaling.

1.4 Integrins on immune cell

In immune cells (or collectively termed leukocytes), integrins, especially β_2 integrins, play essential roles during the immune responses to the injury or infection in

the body. At least 12 types of integrin are expressed on leukocytes and platelets. And Table 1.2 shows the distribution, ligands, and functions of major integrins in leucocytes (23).

Since integrins control cell adhesion, migration, and cytoskeleton rearrangement, they play important roles in regulating many aspects of the immune system, including leukocyte extravasation from the blood vessels to inflammatory sites within tissues, immunological synapse formation, and phagocytosis and so on. Plenty of evidence from human and mouse models show that defects in expression or activation of integrin on immune cells result in immunodeficiency or autoimmune diseases. Leukocyte adhesion deficiency (LAD) and systemic lupus erythematosus (SLE) are two representative examples (24, 25).

LADs are primary immunodeficiency diseases that are manifested in defects in the adhesion-dependent function of immune cells (26). There are different types of LADs (LAD I/ LAD II/ LAD III), which are caused either by expression defects in integrins, fucosylation of selectin ligands, or signaling (activation) of integrins on leukocytes and platelets. In particular, mutations of the ITGB2 gene that eliminate or reduce the expression of β_2 integrins can result in LAD I. LAD II is caused by mutations in the SLC35C1 gene. This genetic alteration decreases the fucosylation of selectin ligands, which impair tethering and rolling of immune cell-mediated by integrins (27). And LAD III is caused by a mutation in the gene of kindlin 3 that is an essential activator of integrins through inside-out activation signaling (28).

Integrins have also been linked to autoimmune diseases such as systemic lupus erythematosus (SLE). SLE is a chronic inflammatory disease resulting from immune cells' mistaken attacks on healthy tissues in the body. The exact cause of SLE is not known, but several genetic studies revealed an association between SLE and ITGAM-ITGAX genes (encoding for integrin α_M and α_X subunits, respectively) (29, 30). Furthermore, the single nucleotide polymorphism (SNP) rs1143679 has been strongly related to SLE development (31). The rs1143679 SNP occurs within the integrin α_M subunit coding region and encodes a histidine instead of an arginine at position 77. Amino acid 77 lies in the β-propeller domain proximal to the ligand-binding domain in the extracellular region of Mac-1. The primary hypothesis is that signal transduction through the integrin is dampened in the H77-Mac-1 variant. However, the exact molecular mechanism involved and the signaling pathways affected by this mutation have not been explicated and more studies to unveil the actual influence of the R77H mutation are still being carried out (32).

Integrin names	Ligands	Expression patterns	Major functions
$a_L b_2$ (LFA-1, CD11a/CD18)	ICAM-1-5, TLN, Type I collagen	T cell, B cell, monocyte/macrophage, NK cell, DC, neutrophil, eosinophil	Migration of T cell, monocyte, neutrophil and eosinophil, activation and adhesion of T cell, DC and B cell, cytotoxicity of CTL and NK cell
$a_M b_2$ (Mac-1, CR3, CD11b/CD18)	ICAM-1, ICAM-2, ICAM-4, iC3b, fibrinogen, factor X, heparin, laminin, LPS, zymosan, oligodeoxynucleotide, collagen, elastase	Monocyte/macrophage, DC, neutrophil, eosinophil, basophil, NK cell	Adhesion, activation and phagocytosis of macro phage, monocyte, neutrophil, eosinophil, basophil, DC and NK cell
$a_X b_2$ (p150/95, CR4, CD11c/CD18)	C3bi, fibrinogen, collagen, CD23 heparin, LPS denatured protein	Monocyte/macrophage, neutrophil, NK cell	Adhesion and phagocytosis of monocyte/macrophage and neutrophil, adhesion of NK cell
$a_D b_2$ (CD11d/CD18)	ICAM-3, VCAM-1	Macrophage, eosinophil, T cell, NK cell	Adhesion and migration of macrophage and eosinophil, adhesion of T cell
$a_4 b_1$ (VLA-4, CD49d/CD29)	VCAM-1, MAdCAM-1, fibrinogen, fibronectin, thrombospondin, pro-vWF, osteopontin, chondroitin	T cell, B cell, DC, monocyte/macrophage, NK cell, neutrophil, eosinophil, basophil	Migration and development of T cell and B cell, migration of monocyte/macrophage, eosinophil, and DC cell, adhesion of NK cell and neutrophil
$a_4 b_7$ (LPAM-1, CD49d/CD-)	MAdCAM-1, VCAM-1, fibrinogen, fibronectin, osteopontin	T cell, B cell, monocyte/macrophage, NK cell, DC, eosinophil, basophil	Migration and development of T cell and B cell, migration of monocyte, macrophage, DC, eosinophil and NK cell
$a_E b_7$ (HML-1, CD103/CD-)	E-cadherin	T cell, Treg, NK cell, DC, macrophage	Adhesion and activation of T cell and DC, cytotoxicity of T cell, suppressive function of Treg, recruitment of NK cell and macrophage
$a_V b_3$ (CD51/CD61)	Vitronectin, ICAM-1, VCAM-1, PECAM-1, fibrinogen, fibronectin, vWF, LAP-TGF- b, thrombospondin	Monocyte, macrophage, DC, neutrophil	Migration of monocyte, macrophage and neutrophil, phagocytosis of DC and macrophage

CR3, complement receptor-3; DC, dendritic cell; HML-1, human mucosal lymphocyte antigen-1; ICAM-1, intercellular adhesion molecule-1; LAP–TGF- b, latency-associated peptide–transforming growth factor-b complex; LFA-1, lymphocyte function-associated antigen-1; LPS, lipopolysaccharide; LPAM-1, lymphocyte Peyer's patch adhesion molecule-1; Mac-1, Macrophage-1 antigen; MAdCAM-1, mucosal addressin cell adhesion molecule-1; NK cell, natural killer cell; PECAM-1, platelet endothelial cell adhesion molecule-1; TLN, telencephalin; Treg, regulatory T cell; VCAM-1, vascular cell adhesion molecule-1; VLA-4, very late antigen-4; vWF, von Willebrand factor.

Table 1.2 Distributions, Ligands, and Functions of Major Integrins in Leucocytes

Reprinted with permission from Yanbo Zhang, H. W. (2012). Integrin signalling and function in immune cells. Immunology., 135(4):268-75. Copyright © 2012 Shanghai Institute of Biochemistry and Cell Biology, SIBS, CAS. Immunology © 2012 Blackwell Publishing Ltd. See Appendix C.

1.5 Integrin $\alpha_M\beta_2$

Integrin $\alpha_M\beta_2$ (also known as macrophage-1 antigen (Mac-1), complement receptor 3(CR3), or CD11b/CD18) is dominantly expressed on myeloid leukocytes, including monocytes, macrophages, neutrophils, dendritic cells, eosinophils, basophils, and natural killer (NK) cells (33). Abundant evidence indicates that Mac-1 plays diverse roles in immune responses such as phagocytosis, cell-mediated cytotoxicity, chemotaxis and cellular activation (34). Because of the significant involvement of Mac-1 in the immune system, it is very important to study the molecular ligand-binding mechanism and activation mechanism of Mac-1.

1.5.1 Integrin $\alpha_M\beta_2$ ligands

As Table 1.2 exhibited, the hallmark of the integrin is the ability to recognize multiple ligands which greatly enhance integrin functional diversity. But on the other hand, this makes it very difficult to produce a unifying ligand-binding mechanism for all integrins. For a number of years, many structural-function studies have strived to deduce the minimal recognition sequence of integrin ligands (35). And the effort is not in vain, many bioactive amino acid sequences have been revealed as recognition sequences of integrin from extracellular matrix proteins (36). Among these sequences, an arginine-glycine-aspartic acid (RGD) sequence has become the prototypic example of a binding motif for several integrins. Besides RGD, several other sequences have been considered as recognition sites of integrins. These include the sequence HHLGGAKQAGDV for $\alpha_{IIb}\beta_3$, CS-1 peptide/CS-5 peptide for α_4 integrin, GFOGER from collagen for $\alpha_1\beta_1$ and $\alpha_2\beta_1$, ICAM peptides for β_2 integrin and so on (35).

Among all the integrins, $\alpha_M\beta_2$ stands out from the crowd in regard to its high ligand-binding promiscuity and low recognition specificity (37). To date, more than 40 protein ligands have been reported to bind to $\alpha_M\beta_2$ integrin. And the complexity of $\alpha_M\beta_2$ functions is believed to be issued from its capability to bind a number of structurally and functionally dissimilar ligands. As shown in Table 1.2, the reported $\alpha_M\beta_2$ ligands include several cellular receptors such as ICAM-1, ICAM-2 and ICAM-4 (38, 39) from endothelial cells and cells of the immune system. $\alpha_M\beta_2$ also binds to numerous proteins that are expressed in the extracellular matrix including fibronectin, laminin, collagens, vitronectin, thrombospondin, Cyr61, and connective tissue growth factor(25, 40-45). It has also been reported that $\alpha_M\beta_2$ can bind to some plasma proteins and vascular cell receptors such as high molecular weight kininogen (46), factor X (47), complement factor H (48), and E-selectin (49). Furthermore, $\alpha_M\beta_2$ is also able to bind several proteases such as elastase (50), myeloperoxidase (51), and plasminogen (52). $\alpha_M\beta_2$ even binds non-protein ligands, such as heparin (53), β-glucan (54) and so on. Every year, more new and unrelated ligands are being discovered to expand this already incredible list. However, this broad binding specificity of $\alpha_M\beta_2$ integrin is not found in other integrins, even the closely related leukocyte integrins such as $\alpha_L\beta_2$, and $\alpha_X\beta_2$ (55). Recently, Tatiana Ugarova's group performed a series of experiments using peptides library and phage display methods to screen known protein ligands for α_M I-domain. Interestingly, they found the key feature of the α_M I-domain recognition motif is a small core consisting of basic amino acids flanked by hydrophobic residue rather than the traditional integrin ligand recognition sites, which contains at least one acidic amino acids (56).

The molecular mechanism by which $\alpha_M\beta_2$ achieves this broad ligand recognition capability is far from clear, either is the relationship between $\alpha_M\beta_2$ ligand recognition promiscuity and its physiological function. However, this unique α_M I-domain recognition ability does allow us to gain a deeper understanding of the molecular binding mechanism of physiological cationic ligands. And this thesis is devoted to demonstrating a novel binding mechanism of $\alpha_M\beta_2$ recognition domain from two newly discovered $\alpha_M\beta_2$ cationic ligands: pleiotrophin (PTN) and platelet factor 4 (PF4) (57， 135).

1.5.2 Integrin $\alpha_M\beta_2$ α I-domain

The α subunit of $\alpha_M\beta_2$ integrin contains an α I-domain, which is connected to the β-propeller domain (Figure 1.2) and plays a pivotal role in ligand binding and integrin activation as mention in the previous section. In 1995, Robert Liddington and his colleagues solved the crystal structure of the α_M I-domain, which was the first integrin I-domain structure determined (58). The crystal structure shows that the α_M I-domain adopts the dinucleotide-binding or Rossmann fold which is composed of a central β-sheets core surrounded by α-helical strands (Figure 1.4). There are six β-sheet strands and seven α-helices arranged in an alternating fashion. In the tertiary structure of α_M I-domain, the α-helices wrap around the β-sheet in counterclockwise order when viewed from the "top" face, where MIDAS is located, and the N, C terminus of α_M I-domain, close to the "bottom" face, are linked to the β-propeller domain.

Canonically, it has been widely accepted that integrin ligands bind to α_M I-domain using interactions with the divalent cation (Mg^{2+}, Ca^{2+}) and metal-coordinating residues in three different loops of MIDAS (Figure1.4). Those metal coordinating residues are

mainly polar and negative charged amino acids. For instance, the first loop, between β_1 and α_1, contains three coordinating residues in a sequence of Asp-Xaa-Ser-Xaa-Ser or DXSXS, the second loop donates a Thr residue and the third loop donates an Asp (Figure 1.4). In this thesis, we discovered a novel mechanism that allows cationic ligands, such as pleiotrophin, platelet factor 4, to bind to α_M I-domain's negatively charged residues in a cation independent manner.

Crystal structure data revealed that the α_M I-domain exists in two conformations termed open and closed (59). Subsequent studies suggest that open and closed conformations represent active and inactive α_M I-domain respectively (60). There is also evidence to indicate that the open and closed forms correspond to the high and low ligand affinity states of α_M I-domain (61, 62). Compared to the closed conformation, the amphipathic C-terminal α7 helix of open conformation has shifted downwards by 10 Å, which generates a more negative electrostatic potentials surface on MIDAS and changes its metal coordination to allow the binding of the acidic amino acid in the ligand to the metal (Figure 1.4). In this thesis, a study of open and closed I-domain was discussed in chapter 3. In addition, we discovered that divalent metal affects the cationic ligands binding to open and closed I-domain in distinct ways which may result from different influences of the metal binding on the two forms.

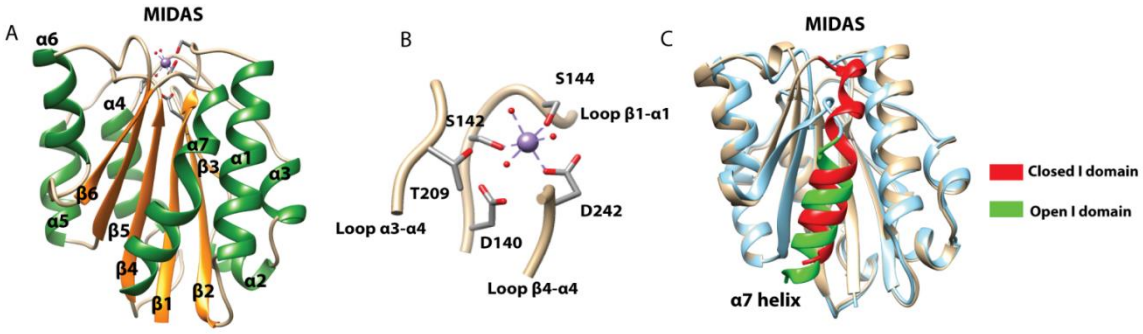

Figure 1.4 Structure of Integrin $\alpha_M\beta_2$ α I-domain.

(A) Ribbon structure of $\alpha_M\beta_2$ α I-domain in closed conformation with Mn^{2+} (pdb: 1jlm); (B) metal coordinating residues in MIDAS of closed α_M I-domain. (C) superimposition of closed (pdb: 1jlm, tan color) and open (pdb: 1ido, cyan color) conformation of I-domain. The major structure change from α7 helix shift is emphasized by two different colors, red color for closed and green color for open.

CHAPTER 2

PLEIOTROPHIN, A MULTIFUNCTIONAL CYTOKINE AND GROWTH FACTOR, INDUCES LEUKOCYTE RESPONSES THROUGH THE INTEGRIN MAC-1

(*Reprinted with permission from Shen D, Podolnikova NP, Yakubenko VP, Ardell CL, Balabiyev A, Ugarova TP, Wang X. Pleiotrophin, a multifunctional cytokine and growth factor, induces leukocyte responses through the integrin Mac-1. J. Biol. Chem. 2017. 17; 292 (46):18848-18861.* *© the American Society for Biochemistry and Molecular Biology or © the Author(s).***)**

2.1 Abstract

Pleiotrophin (PTN) is a multifunctional, cationic, glycosaminoglycan-binding cytokine and growth factor involved in numerous physiological and pathological processes, including tissue repair and inflammation-related diseases. PTN has been shown to promote leukocyte responses by inducing their migration and expression of inflammatory cytokines. However, the mechanisms through which PTN mediates these responses remain unclear. Here, we identified the integrin Mac-1 ($\alpha_M\beta_2$, CD11b/CD18) as the receptor mediating macrophage adhesion and migration to PTN. We also found that expression of Mac-1 on the surface of human embryonic kidney (HEK) 293 cells induced their adhesion and migration to PTN. Accordingly, PTN promoted Mac-1–dependent cell spreading and initiated intracellular signaling manifested in phosphorylation of Erk1/2. While binding to PTN, Mac-1 on Mac-1 expressing HEK293 cells appear to cooperate with cell-surface proteoglycans, since both anti–Mac-1 function-blocking mAb and heparin were required to block adhesion. Moreover, biolayer

interferometry and NMR indicated a direct interaction between the α_M I-domain, the major ligand-binding region of Mac-1 and PTN. Using peptide libraries, we found that in PTN, the α_M I-domain bound sequences enriched in basic and hydrophobic residues, indicating that PTN conforms to the general principle of ligand-recognition specificity of the α_M I-domain toward cationic proteins/peptides. Finally, using recombinant PTN-derived fragments, we show that PTN contains two distinct Mac-1 binding sites in each of its constitutive domains. Collectively, these results identify PTN as a ligand for the integrin Mac-1 on the surface of leukocytes and suggest that this interaction may play a role in inflammatory responses.

2.2 Introduction

Pleiotrophin (PTN) is a glycosaminoglycan-binding cytokine and growth factor with potent mitogenic and angiogenic activities. Together with the related protein midkine, it forms a unique family of cytokines that are normally expressed during embryogenesis and neonatal development but are also produced by injured tissues during repair and regeneration (63, 64). PTN has also been identified as crucial in the maintenance of hematopoietic stem cells (65, 66). Moreover, PTN levels have been shown to be highly elevated in a large number of cancer cell lines as well as being correlated with their metastatic abilities (67-75). Several studies have also associated PTN with inflammation and leukocyte recruitment (75, 76). There are now efforts to both develop PTN inhibitors to treat cancer as well as to use PTN itself for prevention of tissue injury during ischemia (77-80). Several proteins have been proposed as receptors of PTN. The most studied among these include the heparan sulfate proteoglycan (HSPG) N-

syndecan and the chondroitin sulfate proteoglycan receptor-type protein tyrosine phosphatase ζ (PTPRZ) (81-83). Several non-proteoglycan receptors are also known to bind PTN, including nucleolin (84, 85) and the integrin $\alpha_V\beta_3$ (86).

Structurally, PTN is made up of two thrombospondin type-1 repeat (TSR) domains flanked by unstructured termini, both of which are highly basic. (87, 88) The TSR domains also contain a number of basic amino acid clusters with two clusters in the C-terminal TSR domain having the highest affinity for glycosaminoglycans (87, 89). It is thought that the basic nature of PTN is crucial to its ability to interact with receptors and initiate signaling.

Although the role of PTN in mitogenesis and angiogenesis has been extensively researched, its function in inflammation was not widely explored. Given the fact that injured tissues express PTN, it is likely that leukocytes are exposed to it at sites of inflammation. Indeed, some studies suggested that PTN plays a role in recruitment of leukocytes during inflammation (75, 76). However, the identity of the PTN receptor(s) on leukocytes that mediate this response and the role of PTN signaling in these cells remain unknown. We hypothesized that integrin $\alpha_M\beta_2$ (Mac-1, CD11b/CD18, CR3) can serve as a receptor for PTN. This hypothesis was based on our recent finding that Mac-1 binds cationic proteins, many of which, similar to PTN, interact with heparin (44, 56, 90)

Mac-1 is an adhesion receptor expressed on the surface of myeloid cells such as monocyte/macrophages and neutrophils. As an adhesion receptor, Mac-1 is crucial to numerous leukocyte responses, including migration, phagocytosis, degranulation, adherence to microorganisms and others (91, 92). Among integrins, which are in general

notorious for their capacity to recognize multiple ligands, Mac-1 is its most promiscuous member. In contrast to many other integrins that recognize the RGD motif, Mac-1 does not bind this sequence. Instead, as we have recently revealed, Mac-1 has preferences for sequences enriched in basic and hydrophobic amino acid residues (56, 90, 93, 94). The identification of Mac-1 recognition motifs has led to the prediction that other cationic proteins and peptides released from leukocytes and other cells during tissue injury can serve as Mac-1 ligands (56). Most of Mac-1's ligand binding and thus its broad ligand binding specificity can be attributed to the α_M I-domain, a region of ~200 amino acid residues inserted into the αM-subunit, inasmuch as its removal in Mac-1 eliminates ~85% of ligand binding (95).

In this study, we present biochemical and cell biology evidence that PTN is a ligand for Mac-1. Using various Mac-1-expressing cells, we demonstrate that Mac-1 supports adhesion to PTN, promotes spreading and induces activation of the MAP kinase Erk1/2. Furthermore, PTN induces a potent migratory response in Mac-1-expressing HEK293 cells and in isolated murine macrophages. Direct interaction between PTN and the α_M I-domain, the major ligand-binding region of Mac-1, has been shown using biolayer interferometry analyses and confirmed by solution NMR spectroscopy. Finally, using peptide array analysis, we identified the putative α_M I-domain binding sites in both TSR domains of PTN and validated their importance in cell adhesion and signaling assays with individual recombinant PTN fragments.

2.3 Materials and Methods

1, Reagents

The mouse mAb 44a directed against the human α_M integrin subunit was purified from conditioned media of hybridoma cells obtained from the American Type Culture Collection (Manassas, VA) using protein A agarose. Alexa Fluor 546-conjugated phalloidin was purchased from Life Technologies (Eugene, OR). The mouse mAb G3A1, an IgG1 isotype control for mAb 44a were obtained from Cell Signaling Technology (Beverly, MA). BSA, polyvinylpyrrolidone (PVP), EDTA, heparin, and aggrecan were purchased from Sigma (St. Louis, MO). Calcein AM was purchased from Molecular Probes (Eugene, OR). MAbs directed to total Erk1/2 and the phosphorylated form of Erk1/2 were from Cell Signaling Technology (Beverly, MA). Goat anti-rabbit IgG (H+L)-HRP conjugated antibody was from Bio-Rad (Hercules, CA). Protease and Phosphatase Inhibitor Cocktail was from Thermo Scientific (Rockford, IL).

2, Expression and purification of recombinant proteins

Expression and purification of PTN were performed as previously described (87). Briefly, human PTN ORF cloned into the pET-15b vector was transformed into Origami B (DE3) cells (Novagen, Madison, WI, USA). The transformed cells were grown in M9 medium at 37 °C until induction with 0.25 mM IPTG when OD_{600} reached 0.8. The culture was then incubated with shaking overnight at room temperature. The PTN was purified from the supernatant using heparin-affinity chromatography with a 5 ml HiTrap heparin column (GE Healthcare Life Sciences, Little Chalfont, UK). Truncated PTN fragments, PTN-short (residues G1-K114), NTD (residues G1-C57) and CTD (residues

N58-K114) were cloned into the pET-15b vector and expressed as described above. Expression of recombinant active (residues α_M E123-K315) and nonactive (residues α_M Q119-E333) α_M I-domain as well as active α_L I-domain (residues α_L G127-Y307; K287C, K294C) were previously described (96). Alternatively, the α_M I-domain ORF was cloned into pHUE vector (97) as a fusion protein with ubiquitin and transformed into BL21 (DE3) cells (Bioline, MA, USA). The α_M I-domains were purified with 5 mL HisTrap HP nickel columns (GE Healthcare Life Sciences, Little Chalfont, UK). To remove the His-tag ubiquitin, the fusion protein was incubated with the ubiquitinase USP2 overnight at a protein-to-enzyme ratio of 30:1. The pure α_M I-domain was separated from other impurities by size-exclusion chromatography using a Superdex 75 column (GE Healthcare Life Sciences, Little Chalfont, UK). The α_M I-domain was biotinylated with EZ-Link Sulfo-NHS-LC-Biotin (Thermo Fisher Scientific, Inc., San Jose, CA, USA). The efficiency of biotinylation was tested using a biotin quantitation assay kit (Thermo Fisher Scientific, Inc.) with biotinylated horseradish peroxidase as a standard.

3, Screening of peptide libraries for α_M I-domain binding

A peptide library was prepared by parallel spot synthesis on cellulose membranes as described previously (98, 99). Purified recombinant α_M I-domain was labeled with ^{125}Iodine using IODO-GEN (Pierce). The library spanning the sequence of PTN was synthesized as 9-mer overlapping peptides with a 3-amino acid offset. Peptides were C-terminally attached to the cellulose via a $(\beta\text{-Ala})_2$ spacer and were acetylated N-terminally. The membrane with attached peptides was blocked with 1% BSA and then incubated with 10 μg/ml of ^{125}I-labeled α_M I-domain in TBS containing 1 mM $MgCl_2$,

0.05% Tween-20 and 1mM dithiothreitol. After washing, the membrane was dried and the α_M I-domain binding was visualized by autoradiography and analyzed by densitometry.

4, NMR

PTN ^{1}H-^{15}NHSQC NMR data were collected using a Bruker 600 MHz Avance III HD spectrometer (Bruker Instrument, Inc. Bellerica, MA, USA) equipped with a Prodigy probe. The NMR samples contained 40 μM PTN in PBS buffer at pH 7.5 and either 0 μM or 40 μM unlabeled α_M I-domain. Data were processed using NMRPipe (100) and analyzed with NMRView (101).

5, Cells

HEK293 and Mac-1-HEK293 were previously described (55). The cells were maintained in DMEM (Mediatech Inc, Manassas, VA) with 10% fetal bovine serum and antibiotics. The IC-21 mouse macrophage cell line was obtained ATCC. Mouse peritoneal macrophages were isolated from the peritoneal lavage of wild type (C57BL/6J) and Mac-$1^{-/-}$ (B6.129S4-*Itgam*^{tm1Myd}/J) mice three days after thioglycollate (TG) injection using the EasySep Mouse selection kit (StemCell Technologies) with mAb F4/80 conjugated to FITC.

6, Cell adhesion assays

Human embryonic kidney 293 cells (HEK293) and HEK293 cells stably expressing integrin Mac-1 (Mac-1-HEK293) were previously described (55). The cells were maintained in DMEM (Mediatech Inc, Manassas, VA) with 10% fetal bovine serum and antibiotics. The IC-21 mouse macrophage cell line was obtained from ATCC. Mouse

peritoneal macrophages were isolated from the peritoneal lavage of wild type (C57BL/6J) and Mac-$1^{-/-}$ (B6.129S4-*Itgam*^{tm1Myd}/J) mice three days after thioglycolate (TG) injection using the EasySep Mouse selection kit (StemCell Technologies) with mAb F4/80 conjugated to FITC.

7, Cell migration assays

Cell migration assays were performed under sterile conditions using Transwell inserts (Costar, Corning, NY) with a pore size of 8 μm (HEK293 cells) or 5 μm (macrophages) as described (90, 102). Briefly, after coating PTN on the Transwell membrane at 37 ℃ for 3 hours, cells (100 μl) were loaded in the upper chamber of the Transwell system at a concentration of 3×10^6 cells/ml. For inhibition experiments, cells were pretreated with 20 μg/ml anti-α_M mAb 44a or 1 μg/ml heparin for 20 min at 22 ℃ before loading into the upper chamber of the Transwell system. The lower chamber contained 600 μl of DMEM medium. The migration took place at 37 ℃ in a 5% CO_2 humidified atmosphere for 16 hours. For detection, the HEK293 cells were labeled with Calcein-AM for 30 min at 37 ℃ and macrophages were labeled with FITC during isolation. Cells from the upper chamber of the Transwells were removed by wiping with a cotton-tipped applicator. Images of the cells on the underside of the Transwell filter were taken with a Leica DM 4000B microscope camera (Leica, Buffalo Grove, IL).

8, Cell spreading assays

For cell spreading assays, glass coverslips coated with 1.5 μg/mL PTN were plated in 6-well plates (Costar, Corning, NY) and 4×10^5 cells were added to each well. After incubation at 37 ℃ for different time (30 min, 1, 2, 8 and 24 hours), cells were washed

with PBS and fixed with 2% paraformaldehyde for 10 min at room temperature then treated with 0.1% Triton X-100. For actin staining, the cells were treated with 200 μl of 165 mM phalloidin solution for 20 min at room temperature. DAPI was added for DNA staining. The specimens were imaged with a Leica SP5 laser scanning confocal microscope using 63×/1.4 objective. The diameter of 20-50 cells for each time point was counted using ImageJ software from images taken with 20×/0.5 objective. The diameter was defined as the largest distance between two opposite sides of the cell.

9, Biolayer interferometry

The experiments were performed using an Octet K2 instrument (FortéBIO, Pall Corporation). Purified PTN was immobilized on the Amine Reactive Second-generation (AR2G) biosensor using the amine coupling kit according to the manufacturer's protocol. Different concentrations of the active and nonactive forms of α_M I-domain and active α_L I-domain were applied in the mobile phase and the association between the immobilized and flowing proteins was detected. Experiments were performed in 20 mM HEPES, 150 mM NaCl, 1 mM $MgCl_2$, 0.05% (v/v) Tween 20, pH 7.5 or in 20 mM HEPES, 150 mM NaCl, 5 mM EDTA, 0.05% (v/v) Tween 20, pH 7.5. The PTN-coated surface was regenerated with 25 mM NaOH. Analyses of the binding kinetics were performed using ForteBio Data Analysis 9.0 software. The dissociation rate constant (Kd) was obtained by curve fitting of the association and dissociation phases of sensorgrams using a heterogeneous ligand model. BLI experiments were also carried out using PTN biotinylated through glutamate or aspartate side chains with Amine-PEG2-biotin (Thermo Fisher Scientific). Biotinylated PTN at the concentration 50 μg/ml was

immobilized on the Streptavidin Biosensor in 20 mM HEPES buffer supplemented with 150 mM NaCl, 0.1% BSA, 0.02% Tween 20, 1 mM $MgCl_2$ and 1 mM $CaCl_2$ for 15 min that generated saturated level of PTN on the biosensor. After immobilization, the biosensor was washed with HEPES buffer and different concentrations of α_M I-domain were added to the immobilized PTN. After each association-dissociation cycle biosensor was regenerated using 20 mM NaOH.

10, Western blotting

The HEK293 cells and the Mac-1-HEK293 cells were added to the wells of 6-well culture plates at 2×10^6/well and cultured for 2 h in DMEM/F-12+10% FBS. Adherent cells were treated with PTN and PTN fragments (0.7 μM). After 30 min at 37 °C in a humidified 5% CO_2 atmosphere, cells were washed with ice-cold PBS containing a Protease and Phosphatase Inhibitor Cocktail (Thermo Scientific). Next, 200 μl of the lysis buffer (50 mM Tris-HCl, pH 7.4, 1% Triton X-100, 150 mM NaCl, 1 mM EDTA, and Protease and Phosphatase Inhibitor Cocktail) was added to each well, and cells were incubated on ice for 1 h. Protein concentration in the lysates was quantified by a BCA assay (Thermo Scientific) and equal amounts of protein (20 μg) were loaded onto 12.5% SDS-polyacrylamide gels. After the transfer of proteins onto nitrocellulose membranes, the membranes were blocked with skim milk and incubated with anti-Erk and anti-phospho-Erk1/2 (Tyr^{202} and Tyr^{204}) rabbit mAb. The mAb binding was detected using HRP-conjugated goat anti-rabbit antibodies and chemiluminescence (Thermo Scientific).

11, Statistical analysis

All data are presented as the mean ± S.E. The statistical differences were determined using a one-way analysis of variance (ANOVA) using SigmaPlot 11.0 software (Systat Software, San Jose, CA). For multiple comparisons, the Bonferroni correction method was used. Differences were considered significant if the p-value was less than 0.05.

2.4 Results

1, Mac-1 is involved in adhesion of Mac-1-expressing cells to PTN

To assess whether PTN can bind Mac-1 we initially examined the ability of Mac-1-HEK293 to adhere to immobilized PTN. As shown in Figure 2.1A, Mac-1-HEK293 cells adhered to immobilized PTN in a concentration-dependent manner with saturable adhesion achieved with a PTN coating concentration of ~100 nM. Wild-type HEK293 cells also strongly adhered to PTN. Still, the presence of Mac-1 significantly augmented adhesion (Figure 2.1A). Since PTN has a high affinity for glycosaminoglycans and HSPG N-syndecan binds PTN, we examined the possibility that HSPGs on wild-type HEK293 cells mediate adhesion to PTN. Preincubation of cells with heparin (1 μg/ml) almost completely eliminated adhesion (Figure 2.1B), indicating that on the surface of these cells HSPGs are entirely responsible for PTN binding. However, adhesion of Mac-1-HEK293 cells was reduced by only ~60 % suggesting that Mac-1 on these cells may be involved in binding PTN. To investigate this possibility, Mac-1-HEK293 cells were treated with the function-blocking mAb 44a (directed against the α_M I-domain of Mac-1). Although adhesion tended to decrease, it was not significantly altered, with the maximal blocking

effect (19 ± 10%) observed at 10 µg/ml of mAb. Likewise, although heparin inhibited adhesion in a dose-dependent manner, the maximal blocking effect attained did not exceed 59 ± 6%. However, when Mac-1-HEK293 cells were treated with both mAb 44a and heparin, cell adhesion was inhibited by >95%. These results suggest both HSPG and Mac-1 can act as receptors for PTN.

Consistent with the role of Mac-1 in adhesion to PTN, Mac-1-HEK293 cells spread with the formation of actin filaments, as detected by staining with Alexa Fluor 546-conjugated phalloidin (Figure 2.1C, upper panels). By contrast, the spreading of wild-type HEK293 cells was visibly less, even after 24 hours (Figure 2.1C, bottom panels). Quantification of cell spreading confirmed this observation (Figure 2.1D).

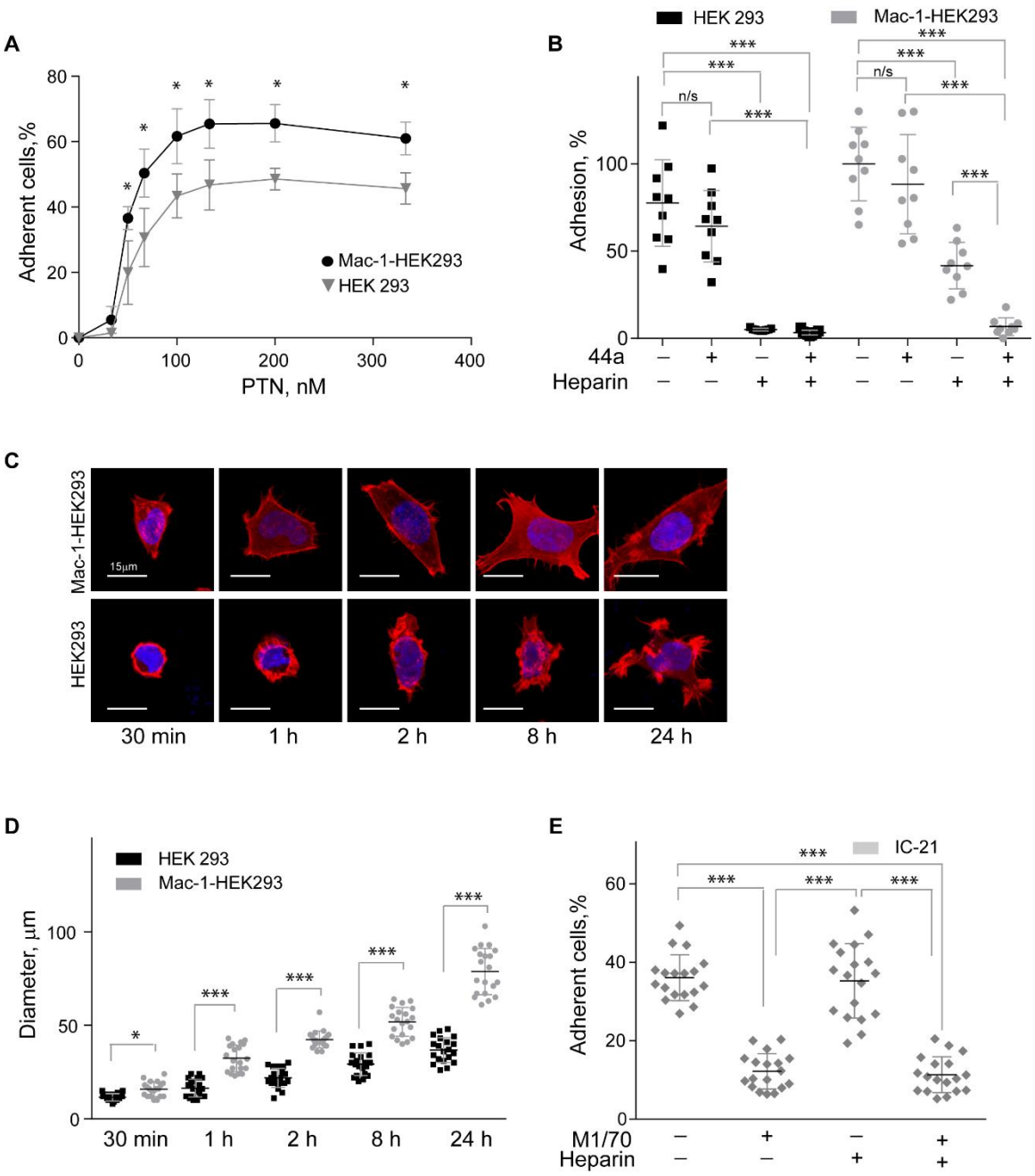

Figure 2.1 PTN Supports Adhesion and Spreading of Mac-1-expresing HEK293 Cells and IC-21 Macrophages.

(A) Aliquots (100μl; 5x10^4/ml) of Mac-1-expressing HEK293 (Mac-1-HEK293) and wild-type HEK293 (HEK293) cells labeled with calcein were added to microtiter wells coated with different concentrations of PTN and post coated with 1% PVP. After 30 min at 37 °C, nonadherent cells were removed by washing and fluorescence of adherent cells was measured in a fluorescence plate reader. Data shown are means ± S.E. from three separate experiments with triplicate measurements.

***p≤0.05, **p≤0.01, ***p≤0.001. Statistically insignificant differences are not labeled. (B) Mac-1-HEK293 cells and HEK293 cells were preincubated with anti-α_M mAb 44a (5 μg/ml), heparin (1 μg/ml) or their mixture for 20 min and added to wells coated with 100 nM PTN. Adhesion in the absence of Mac-1 inhibitors and heparin was assigned a value of 100%. Data shown are means ± S.E. from three separate experiments with triplicate measurements. *p≤0.05, **p≤0.01, ***p≤0.001 compared with control adhesion in the absence of inhibitors. (C) Mac-1-HEK293 (upper panel) and HEK293 cells (lower panel) were plated on glass slides coated with 100 nM PTN and allowed to adhere for different durations at 37 °C. Nonadherent cells were removed and adherent cells were fixed with 2% paraformaldehyde, permeabilized with 0.1% triton X-100 in PBS followed by staining with Alexa Fluor 546 phalloidin (actin) and DAPI (DNA). The cells were imaged with a Leica SP5 laser scanning confocal microscope with a 63x/1.4 objective. (D) the diameter of 20-50 Mac-1-HEK293 and HEK293 cells was calculated for each time point from images captured with a 20x/0.50 objective. Data shown are means ± S.E. from five random images for each time point from one to four experiments. *p≤0.05, ***p≤0.001. (E) IC-21 macrophages were preincubated with anti-mouse α_M mAb M1/70 (10 μg/ml), heparin (1 μg/ml) or their mixture and added to wells coated with 100 nM PTN. Data shown are means ± S.E. from three separate experiments with six measurements. *p≤0.05, ***p≤0.001.**

To investigate the relevance of PTN-Mac-1 interaction in immune cells, we performed adhesion assays using IC-21 cells, a murine macrophage cell line naturally expressing Mac-1. As shown in Figure 2.1E, IC-21 cells adhered to immobilized PTN and ~ 65% of adhesion was inhibited by mAb M1/70 against the murine α_M integrin subunit. This is in contrast to Mac-1-HEK293 cells, whose adhesion to PTN was reduced modestly by mAb 44a (Figure 2.1B). Moreover, heparin, which greatly decreased the adhesion of Mac-1-HEK293 cells to PTN, had little effect on adhesion of IC-21, suggesting that Mac-1 on the surface of IC-21 cells largely contributes to the interaction with PTN. Together, these results identify PTN as an adhesive ligand for Mac-1 and suggest that on the surface of different cells both Mac-1 and HSPGs are involved in PTN adhesion, albeit to a different extent.

2, PTN bound to extracellular matrix (ECM) proteoglycans supports adhesion of Mac-1-HEK293 cells

Because PTN is secreted from cells and deposited into the extracellular matrix (ECM), we explored whether PTN bound to the ECM components is capable of supporting adhesion. Since Mac-1 is known to interact with a number of ECM proteins, including fibronectin, vitronectin, collagens, Cyr61 and others (103), a heterogeneous mixture of these molecules such as those found in Matrigel was not suitable as a substrate for investigations of PTN-Mac-1 interactions. PTN is only known to bind proteoglycans; therefore, the most relevant form of PTN encountered by immune cells *in vivo* is likely to be PTN anchored to ECM proteoglycans. To simulate such an environment, we studied cell adhesion to PTN pre-bound to aggrecan, a common proteoglycan found in the ECM. Figure 2.2 shows that at two concentrations of PTN tested, both Mac-1-HEK293 and HEK293 cells adhered to aggrecan-bound PTN, with Mac-1-HEK293 cells adhering at a significantly higher level than HEK293 cells ($p<0.001$). Neither type of cells had affinity for aggrecan itself. Notably, the binding of PTN to aggrecan did not reduce cell adhesion, indicating that PTN in its aggrecan-bound form remains an efficient Mac-1 ligand.

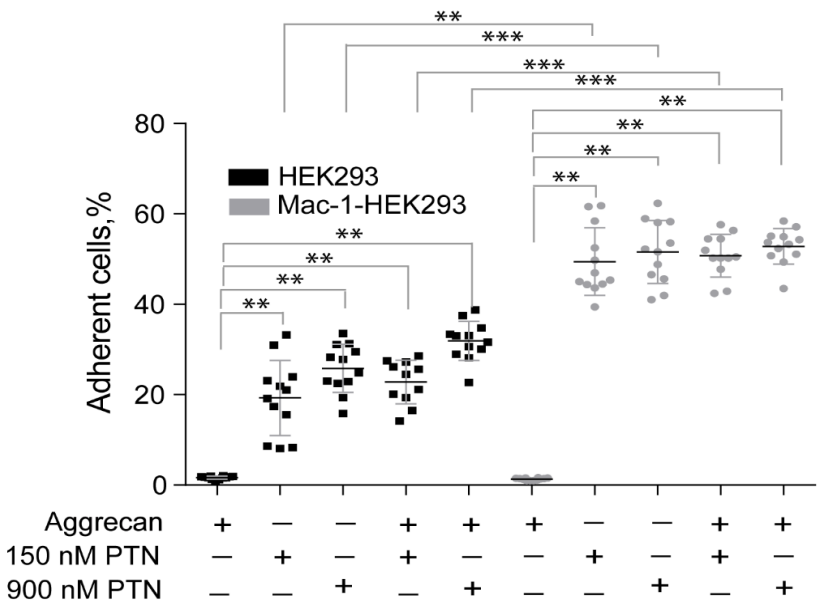

Figure 2.2 Effect of Aggrecan on PTN-mediated Adhesion of Mac-1-expressing HEK293 Cells.
Aggrecan (10 µg/ml) was used to coat the microtiter wells overnight before the addition of PTN (150 and 900 nM). Aliquots (100 µl; $5x10^4$/ml) of Calcein-labeled Mac-1- HEK293 and wild-type HEK293 cells were added to microtiter wells. After 30 min at 37 °C, nonadherent cells were removed by washing and fluorescence of adherent cells was measured in a fluorescence plate reader. Data shown are means ± S.E. from two separate experiments with six measurements. *p≤0.05, **p≤0.01, ***p≤0.001.

3, PTN induces migration of Mac-1-expressing cells

PTN is known to induce cell migration and in some instances, this effect has been shown to be integrin-dependent (104, 105). Therefore, we investigated whether Mac-1 can support PTN-induced migration. In particular, using a Transwell system we compared the ability of wild-type and Mac-1-HEK293 cells to migrate towards PTN. Previous studies reported that these cell lines are a useful system for assessing the role of Mac-1 in migration (102). PTN induced a potent migratory response (Figure 2.3A and 2.3B). In contrast, wild-type HEK293 migrated only slightly. Direct evidence that

migration of Mac-1-HEK293 cells was dependent on Mac-1 was obtained in the experiments in which anti-Mac-1 mAb 44a was tested. While mAb 44a eliminated cell migration, an IgG1 isotype control for this mAb had no significant effect (Figure 2.3B). Heparin (1 μg/ml) also inhibited migration to a modest, but significant degree.

In a separate set of experiments, we tested whether PTN can induce migration of mouse macrophages isolated from the peritoneum of wild-type and Mac-1-deficient mice. Macrophages were purified from a total population of peritoneal cells and their migration was examined in a Transwell system. As shown in Figure 2.3C and 2.3D, PTN induced a strong migratory response in wild-type macrophages. PTN also induced the migration of Mac-1-deficient macrophages. However, compared to wild-type cells, migration of Mac-1-deficient macrophages was significantly impaired (by 76 ± 21%). These results indicate that Mac-1 is a crucial mediator of PTN-induced cell migration. Furthermore, since macrophages lacking Mac-1 can migrate, albeit at a significantly reduced rate, other integrins(most likely $\alpha_V\beta_3$) may contribute to migration.

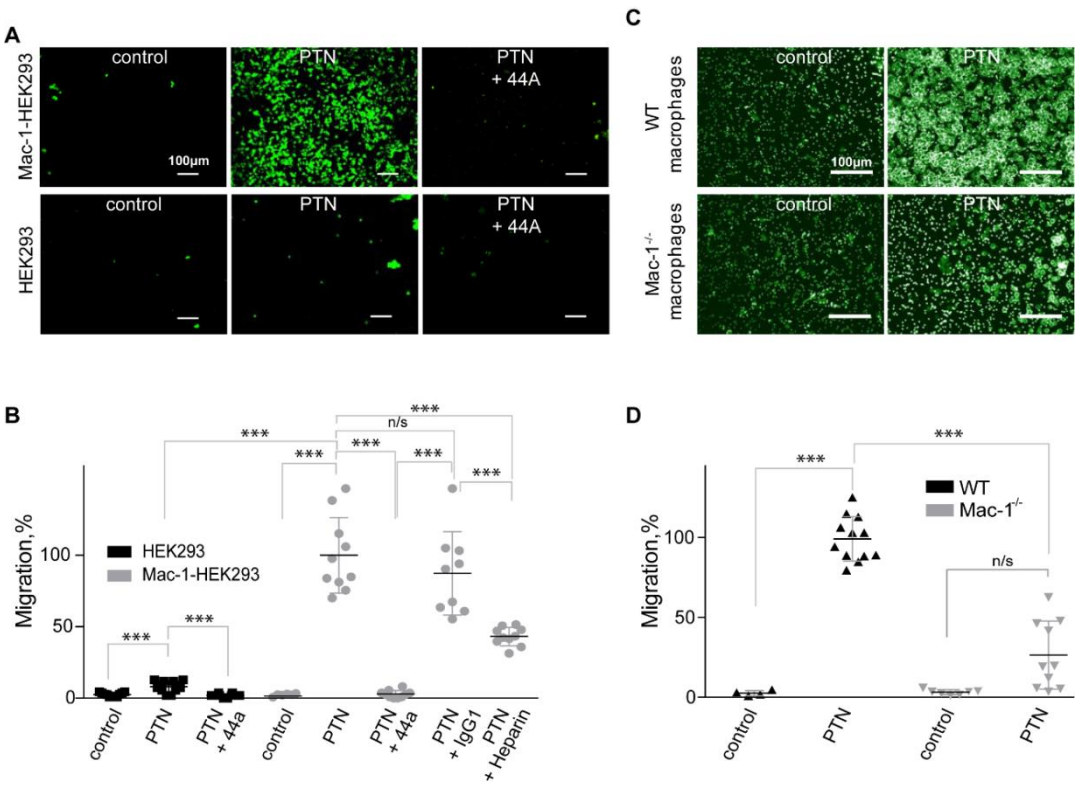

Figure 2.3 Migration of Mac-1-expressing Cells to PTN in a Transwell System.
(A) Transwell inserts were coated with 67 nM of PTN for 3 h at 37 °C. Mac-1-HEK 293 cells (100 µl at 3 × 10^6/ml) were added to the upper wells of the Transwell chamber and their ability to migrate was analyzed. After 16 hours at 37 °C, the cells were labeled with Calcein-AM for 30 min at 37 ℃, and the cells from upper chamber were removed by wiping with a cotton-tipped applicator. Images of the cells on the underside of the Transwell filter were taken with a 10x/0.25 objective. The figure is representative of three experiments. In separate experiments, cells were preincubated with 20 µg/ml of 44a mAb or IgG1 isotype control mAb, or 1 µg/ml heparin for 20 min before loading to the upper wells. (B) quantification of cell migration. The number of migrated cells was determined using NIH ImageJ. Migration was expressed as percentage of pixel intensity of images from at least three random fields per well. The data shown are means and S.E. from three individual experiments. Migration of cells in the absence of inhibitors was assigned a value of 100%. (C) migration of TG-elicited macrophages isolated from the peritoneum of wild-type and Mac-1-deficient mice and purified as described in the Experimental Procedures. 100 µl of macrophages (3x10^6/ ml) were placed in the upper chamber and allowed to migrate through the 5-µm membranes coated with PTN (100 nM) or buffer (control) for 90 min at 37 °C. Images of the cells on the underside of the Transwell filter were taken with a 40x/0.75 objective. (D) quantification of macrophage migration. Data are presented as fluorescence of migrated cells per field ± S.E. for four random fields per well from three individual experiments. *p≤0.05, **p≤0.01, ***p≤0.001.

4, PTN induces activation of MAP kinase (MAPK) Erk1/2

The interaction of integrins with ligands is known to induce activation of MAP kinases. To determine whether PTN activates MAPKs via binding to Mac-1, adherent Mac-1-HEK293 cells were treated with different concentrations of PTN and phosphorylation of Erk1/2 was examined. PTN induced a significant increase in phosphorylation of Erk1/2 and this response was blocked by mAb 44a and heparin (Figure 2.4A, B). The simultaneous use of two reagents increased the inhibitory effect; however, the cumulative effect did not reach a statistical significance. Treatment of control HEK293 cells with PTN did not induce phosphorylation of Erk1/2 (Figure 2.4A). These data suggest that in this system, initiation of intracellular signaling by PTN requires both Mac-1 and HSPGs.

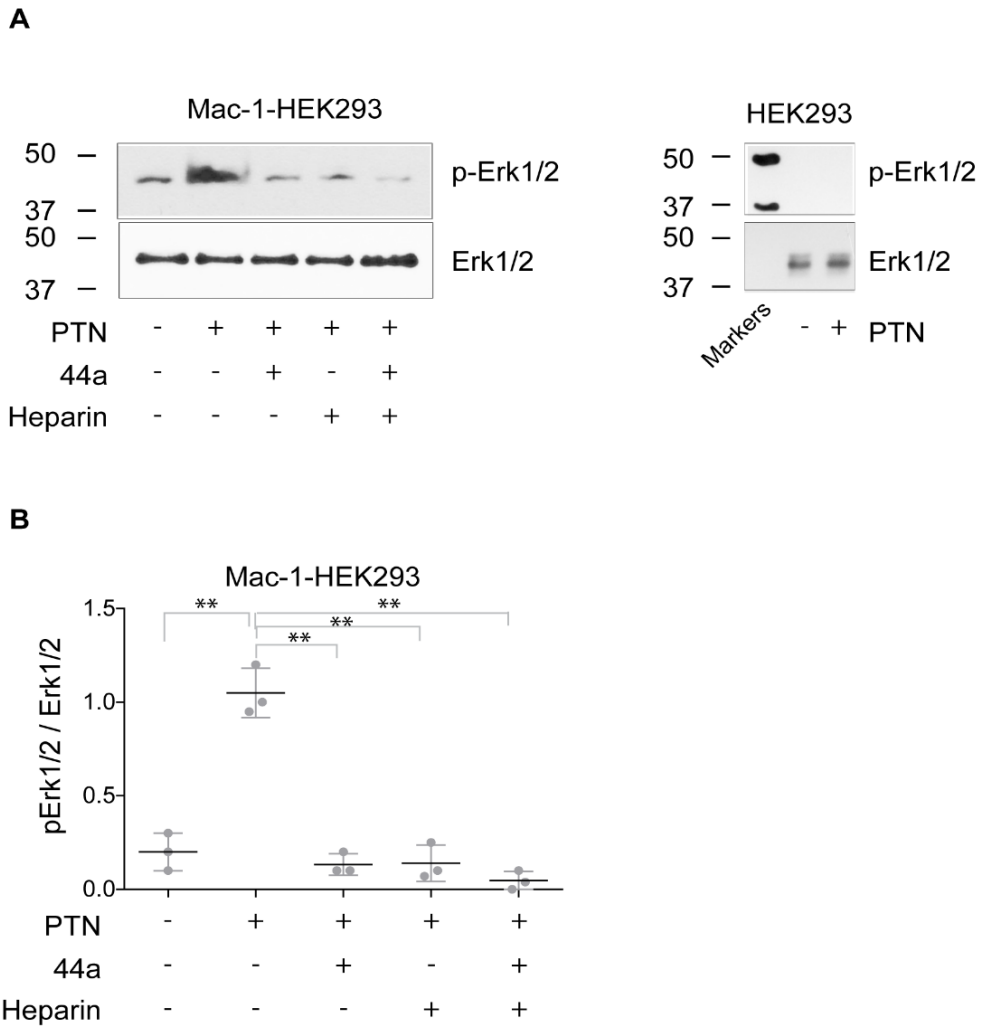

Figure 2.4 PTN-induced Phosphorylation of Erk1/2 in Wildtype HEK293 and Mac-1-HEK293 Cells.

(A) Adherent HEK293 or Mac-1-HEK293 cells were treated with 0.7 µM PTN in the absence and presence of mAb 44a (10 µg/ml), heparin (10 µg/ml) or their combination. After 30 min at 37 °C, cells were washed and lysed. The lysates were separated using 12.5% SDS-PAGE and Western blotting was performed using mAb specific for the phosphorylated form of Erk1/2. The mAb against total Erk1/2 was used to equalize protein loading. A representative of three experiments is shown. The molecular weight markers are shown on the left of each set of blots. (B) densitometry analysis of Erk1/2 phosphorylation for Mac-1-HEK293 cells. Erk1/2 activation data are shown as a ratio of the intensity of the phosphorylated Erk1/2 (pErk1/2) band to the total (Erk1/2) band. The pErk/Erk ratio of the PTN-activated lane was set to 1.0. Data are calculated from three experiments and errors shown are S. E. *p≤0.05, **p≤0.01, ***p≤0.001.

5. Biochemical analyses of the interaction between PTN and α_M I-domain

To further characterize the Mac-1-PTN interactions and determine domains of Mac-1 responsible for PTN binding, we analyzed the binding parameters of the interaction between the α_M I-domain and PTN. We focused on the α_M I-domain since this domain is the major ligand-binding region in Mac-1 and previous studies have shown that several basic proteins and peptides interact with it (56, 90, 94, 96, 106). To measure the affinity of the α_M I-domain-PTN interaction we used biolayer interferometry (BLI) in which PTN has coupled to the matrix coating the biosensor via lysines. The interaction between PTN with both active and nonactive forms of the α_M I-domain was measured in 20 mM HEPES buffer containing 150 mM NaCl, 1 mM $MgCl_2$, 0.05%Tween 20, pH 7.5. When PTN was allowed to interact with various concentrations of soluble active α_M I-domain, a dose-dependent binding was observed (Figure 2.5A and 2.5B). The Kd value determined from the maximal responses achieved in the equilibrium portion of the BLI sensorgrams was 1.2 ± 0.2 μM. The interaction of PTN with nonactive α_M I-domain was also detected (Figure 2.5C); however, binding was lower than that of the active form, which precluded an accurate assessment of the Kd value. In contrast to the α_M I-domains, the active form of the I-domain of integrin $\alpha_L\beta_2$ that has narrow ligand specificity and binds only ICAM and JAM-1 molecules, did not bind PTN (Figure 2.5C). To assess how divalent cations might affect the interaction of PTN with α_M I-domain, the binding of active α_M I-domain was measured in the presence of 5 mM EDTA. As shown in Figure 2.5C, EDTA only modestly decreased binding of active α_M I-domain. The latter result indicates that the α_M I-domain binding to PTN is not dependent on the presence of Mg^{2+}.

Because recognition by the α_M I-domain of many of its ligands depends on basic amino acids, we sought to determine whether immobilization of PTN onto the BLI sensor using lysine side chains may potentially reduce PTN's binding to α_M I-domain. Therefore, we repeated the experiments by randomly biotinylating glutamate and aspartate side chains of PTN and attaching the biotinylated PTN to streptavidin-coated sensors. As determined from the sensorgrams shown in Figure 2.5D, the alternative mode of immobilization did not change considerably the binding affinity of the two proteins (Kd=3.9± 0.1 μM).

We also examined the interaction of PTN with the active α_M I-domain using solution NMR. Figure 2.6A shows the ^{1}H-^{15}N HSQC spectrum of PTN in the presence and absence of one molar equivalent of active α_M I-domain. Addition of the α_M I-domain decreased the signal intensities of residues in the TSR domains of PTN by ~ 40%, whereas PTN residues in the unstructured N- and C-termini were not affected by α_M I-domain (Figure 2.6B). Signal intensity decrease often takes place when a small protein binds a larger protein, or if the interactions between the two are dynamic and the kinetics of the interaction is on the intermediate NMR time scale (107). The observation of signal intensity decreases, therefore, indicates the TSR domains of PTN are involved in binding α_M I-domain. Together, these data indicate PTN has a significant affinity for the active form of the α_M I-domain.

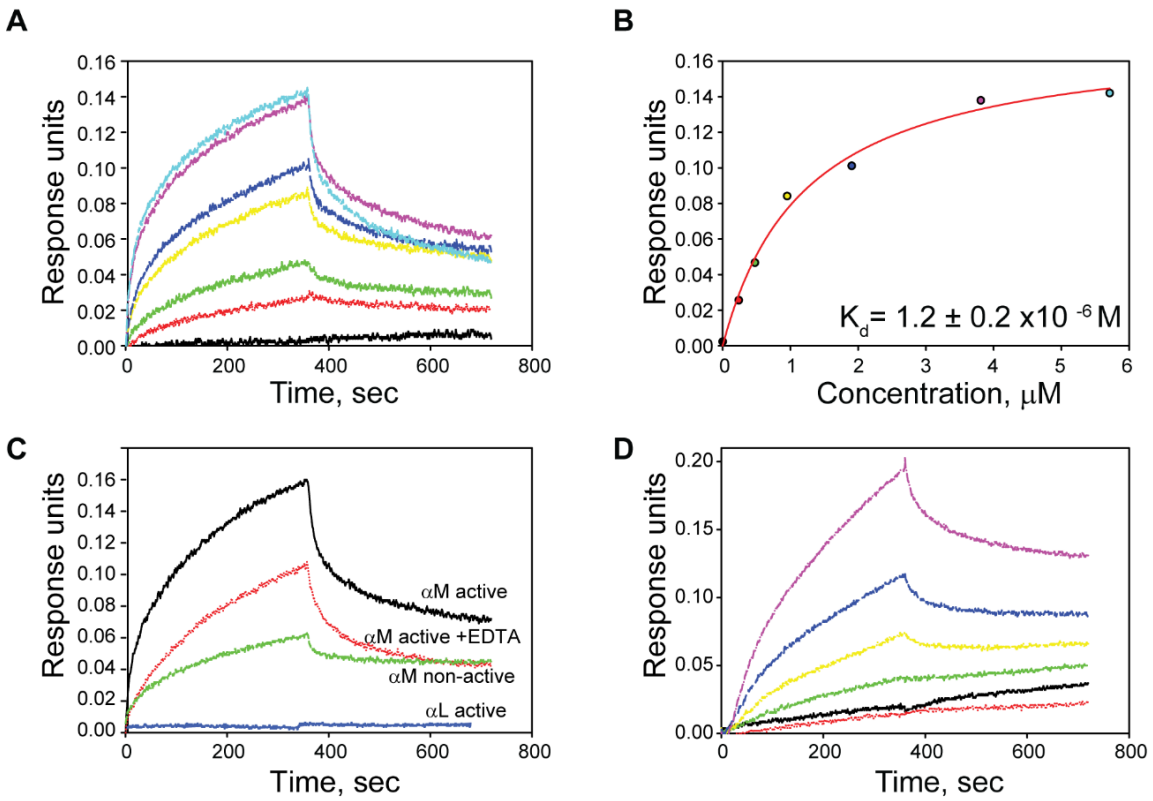

Figure 2.5 Analyses of Binding of the α_M I-domains to PTN by BLI.
(A) Representative sensorgrams of titration of PTN immobilized on the ForteBio sensor with active α_M I-domain (0; 0.24; 0.48; 0.95;1.9; 3.8; 5.7 μM). (B) the saturable binding curve for the interaction of the α_M I-domain with PTN. Representative data from 3 independent experiments are shown. (C) comparison between different I-domains (5.7 μM) for their ability to bind PTN. The interaction between the active α_M I-domain and PTN in the presence of 5 mM EDTA is also shown. Representative data of three separate experiments are shown. (D) representative binding curves of titration of biotinylated PTN immobilized on the ForteBio streptavidin sensor with active α_M I-domain (0; 0.15; 0.3; 0.75;1.5; 3.0 μM).

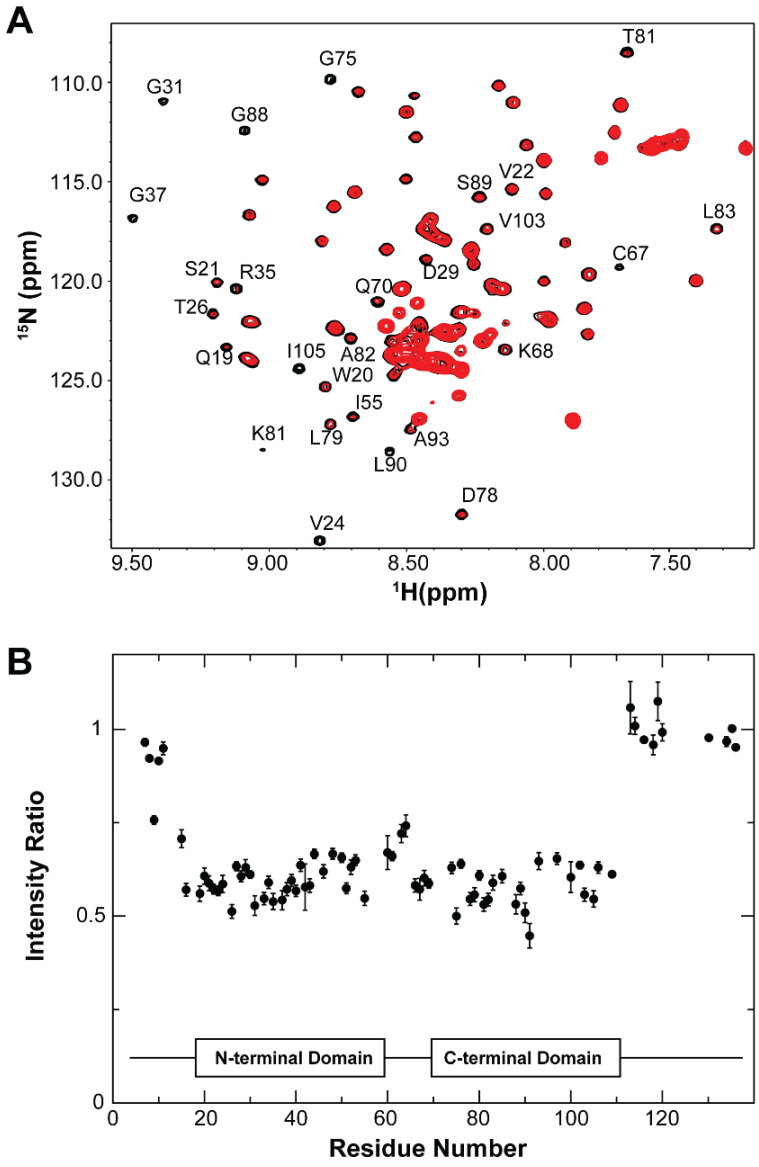

Figure 2.6 PTN Binding to the α_M I-domain Determined From ^{1}H-^{15}N HSQC Spectra of ^{15}N-labeled PTN.

(A) Superimposed ^{1}H-^{15}N HSQC spectra of 40 μM ^{15}N-labeled PTN in the presence (red contour) and absence (black contour) of 40 μM of active α_M I-domain. The presence of the α_M I-domain led to significant decreases in signal intensities of many residues. Residues whose signals were most significantly altered have been labeled with their residue numbers. (B) The ratio of signal intensities for each PTN residue in the presence and absence of active α_M I-domain.

6, Screening of the PTN-derived peptide libraries for α_M I-domain binding

To localize the putative α_M I-domain binding sites in PTN, we screened the cellulose-bound peptide library representing the complete sequence of PTN. The library, consisting of 9-mer peptides with a 3-residue offset (Figure 2.7A), was probed with ^{125}I-labeled recombinant α_M I-domain. The screening identified four peptide clusters that strongly bound the α_M I-domain (Figure 2.7B). These clusters correspond to the following PTN sequences: 1-15 (cluster 1; spots 1-3), 46-69 (cluster 2; spots 16-21), 82-99 (cluster 3; spots 28-31) and 106-132 (cluster 4; spots 36-42). Control spots containing only β-Ala spacer (spots 49 and 50) were negative, as were many other peptides. The α_M I-domain-binding peptides were analyzed by a computer program designed to determine the capacity of peptides to interact with the α_M I-domain (56). The program assigns each peptide an energy value which serves as a measure of the probability that the α_M I-domain binds this sequence: the lower the energy, the higher the likelihood that the sequence binds the α_M I-domain. As previously determined, strong α_M I-domain binding peptides derived from various Mac-1 ligands have energy values in the range of −20 to 2 kJ/mole. The analyses showed a good relationship between the energy scores and the α_M I-binding activity of PTN-derived peptides revealed in peptide scans (Figure 2.7A). In agreement with previous findings (56), peptides enriched in positively charged and hydrophobic residues had the highest affinities for the α_M I-domain (spots 2, 16-19, 29, 38 and 42). For example, the stretch of overlapping peptides KQTMKTQRCKIPCNWKKQ (spots 16-19) and peptide KTRTGSLKR (spot 29) contain several short motifs, HyB and BHy where Hy represents any hydrophobic residue a B (basic) is either arginine or lysine, that have

been shown to be abundant in the α_M I-domain binders (56). When mapped onto the three-dimensional structure, the α_M I-domain-binding sequences were found in both TSR domains as well as the N- and C-terminal tails (Figure 2.7C). These results indicate that in the case of PTN, the α_M I-domain has an affinity for its positively charged regions and thus recognition specificity toward PTN conforms to the general principles of ligand recognition exhibited by Mac-1 toward cationic proteins (56).

7, Individual TSR domains of PTN support Mac-1-dependent cell adhesion and induce activation of Erk1/2

The above data from peptide library screening suggest that PTN may contain several α_M I-domain binding sites. These sites have been mapped to the N- and C-terminal (NTD and CTD) TSR domains of PTN as well as the C-terminal tail. To investigate the contribution of each domain to Mac-1 binding, we prepared truncated PTN fragments corresponding to the NTD (residues 1-57), CTD (residues 58-114) and PTN-short (residues 1-114) with the C-terminal tail deleted (Figure 2.9A) and examined their ability to support cell adhesion and induce MAPK activation (Figure 2.9B-F). The data showed that removing the C-terminal tail of PTN did not reduce significantly the ability of PTN-short to support adhesion of Mac-1-HEK293 cells compared to intact PTN (Figure 2.9B and Figure 2.1A). Furthermore, the pattern of adhesion of HEK293 cells to PTN-short (Figure 2.8B) was similar to that of wild-type PTN (Figure 2.1A). Both NTD and CTD were also able to support adhesion (Figure 2.9C, D). However, removing either one of the structural domains of PTN resulted in the reduction of their adhesion-promoting activity (Figure 2.9C, D). In particular, while a 100 nM coating concentration

of wild-type PTN was sufficient to achieve a saturable level of adhesion, a ~5- and ~10-fold higher concentrations of CTD and NTD, respectively, were required to reach saturation. Furthermore, the maximal level of adhesion mediated by these fragments was lower than that mediated by intact PTN. The effect of the removal of either the structural domain of PTN on proteoglycan binding was even more severe. Specifically, wild type HEK293 cells adhered poorly to NTD and CTD, even at a concentration of 1 μM (Figure 2.9C, D). To rule out the possibility that differences in the adhesion-promoting activity of PTN-derived fragments were due to their different coating efficiencies, we examined the ability of soluble fragments to inhibit adhesion. Wild-type PTN and all fragments blocked adhesion in a dose-dependent manner (Figure 2.8). At 5 μM, wild-type PTN was the most potent inhibitor (78 ± 13% inhibition of adhesion), followed by PTN-short (68 ± 15%), CTD (57 ± 10%) and NTD (38 ± 12%) (Figure 2.9E), thus corroborating the results of adhesion assays. Consistent with the presence of the Mac-1 binding sites in both NTD and CTD domains, the treatment of Mac-1-HEK293 cells with each fragment resulted in the phosphorylation of Erk1/2, whereas only basal phosphorylation was detected in untreated cells (Figure 2.9 and Figure 2.10).

A

	Sequence	Energy, J/mole	Densitometry, %	
1.	MGKKEKPEK	-517	45	Cluster 1
2.	KEKPEKKVK	-4051	80	
3.	PEKKVKKSD	-945	65	
4.	KVKKSDCGE	4355	20	
5.	KSDCGEWQW	7217	0	
6.	CGEWQWSVC	3828	30	
7.	WQWSVCVPT	-800	30	
8.	SVCVPTSGD	8991	0	
9.	VPTSGDCGL	9835	0	
10.	SGDCGLGTR	6519	0	
11.	CGLGTREGT	4326	0	
12.	GTREGTRTG	415	60	
13.	EGTRTGAEC	7519	0	
14.	RTGAECKQT	944	10	
15.	AECKQTMKT	1085	15	
16.	KQTMKTQRC	-6619	100	Cluster 2
17.	MKTQRCKIP	-7631	100	
18.	QRCKIPCNW	-5249	90	
19.	KIPCNWKKQ	-6133	100	
20.	CNWKKQFGA	-3449	100	
21.	KKQFGAECK	-1660	95	
22.	FGAECKYQF	450	0	
23.	ECKYQFQAW	-343	0	
24.	YQFQAWGEC	3288	10	
25.	QAWGECDLN	11475	0	
26.	GECDLNTAL	12300	0	
27.	DLNTALKTR	723	55	
28.	TALKTRTGS	-3339	90	Cluster 3
29.	KTRTGSLKR	-10906	100	
30.	TGSLKRALH	-3555	95	
31.	LKRALHNAE	-809	70	
32.	ALHNAECQK	5103	0	
33.	NAECQKTVT	4428	0	
34.	CQKTVTISK	-3055	80	
35.	TVTISKPCG	671	50	
36.	ISKPCGKLT	-2141	70	Cluster 4
37.	PCGKLTKPK	-3543	90	
38.	KLTKPKPQA	-4255	90	
39.	KPKPQAESK	-247	40	
40.	PQAESKKKK	-3323	80	
41.	ESKKKKKEG	-2616	80	
42.	KKKKEGKKQ	-8339	90	
43.	KEGKKQEKM	-612	35	
44.	KKQEKMLDA	2657	10	
45.	EKMLDAAAA	8050	0	
46.	LDAAAAAAA	8698	0	
47.	AAAAAAAAA	4247	30	

B

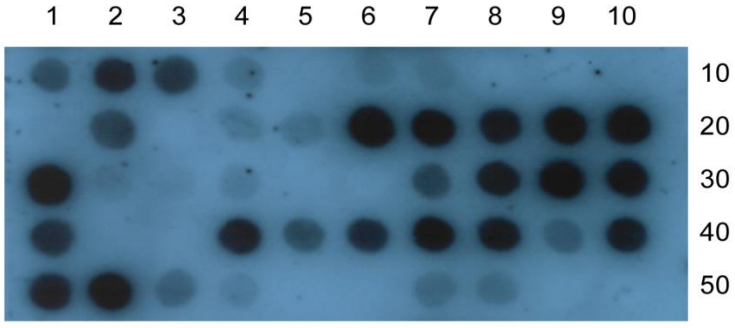

C

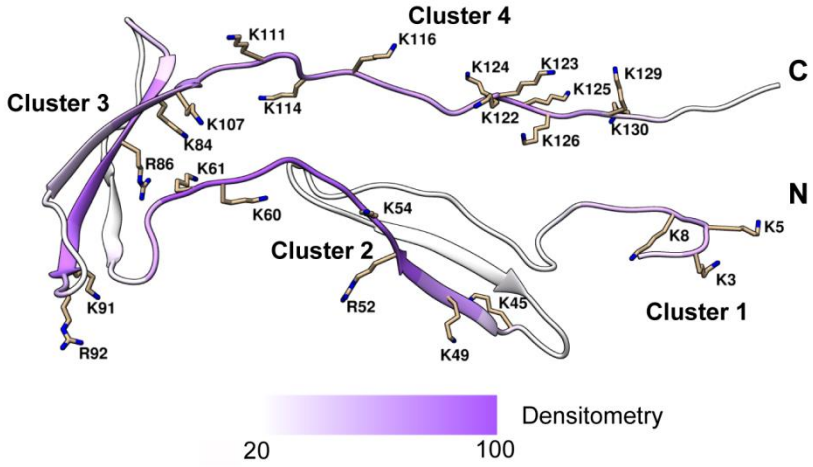

Figure 2.7 Screening of Peptide Library Spanning the Sequence of PTN for α_M I-domain Binding.

The assembled peptide library spanning the sequence of PTN consisting of 9-mer peptides with three-residue offset (A) was incubated with ^{125}I-labeled active α_M I-domain (residues E^{123}-K^{315}) and subjected to autoradiography (B). The α_M I-domain binding was observed as dark spots. Spots 49 and 50 contain only the β-Ala spacer. The numbers in the *right columns* in (A) show the relative binding of the α_M I-domain to peptides determined by densitometry and expressed as a percentage of the intensity of the most active peptide KTRTGSLKR (spot 29). Peptide energies (*middle columns* in A) that serve as a measure of probability each peptide can bind the α_M I-domain was calculated as described (29). (C) The ribbon model of PTN based on PDB Id: 2N6F. Sidechains of Arg and Lys are shown in stick representations. The four clusters with peptides identified as positive for the α_M I-domain binding are shown in purple.

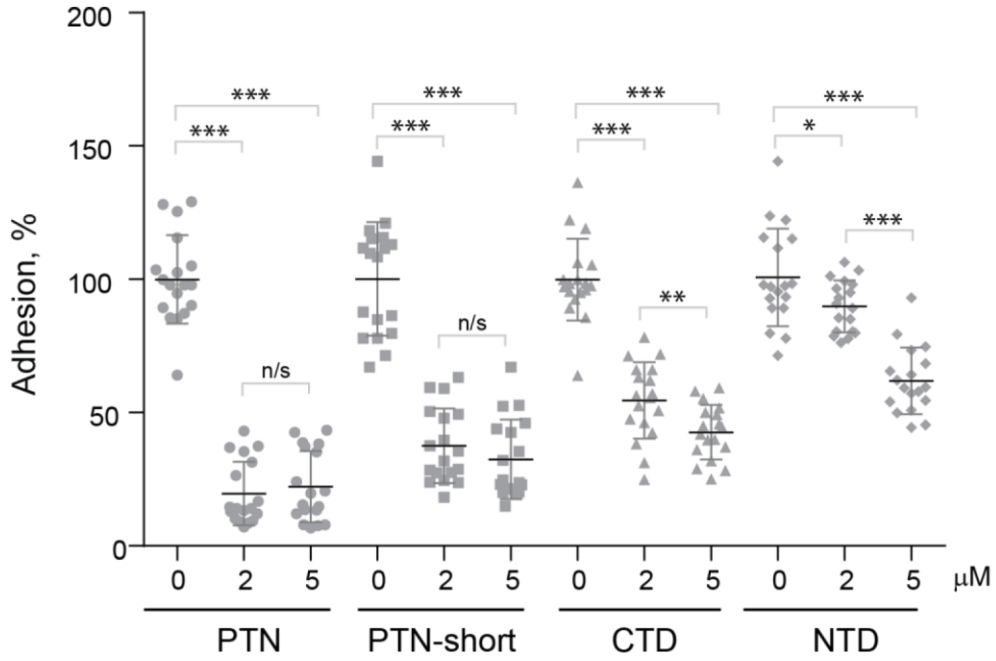

Figure 2.8 PTN Fragments Inhibit the Adhesion of Mac-1-HEK293 Cells to PTN in a Dose-dependent Manner.

The 96-wells 4HBX plates were coated with 100 nM of PTN and post-coated with 1% PVP. Different concentrations of PTN or PTN fragments were preincubated with cells for 20 min before loading into wells. The adhesion assay was performed as described in the Experimental Procedures. Adhesion in the absence of soluble PTN or PTN fragments was assigned a value of 100%. Data shown are means ± S.E. from three separate experiments with sextuplicate measurements. *p≤0.05, **p≤0.001 ***p≤0.001 compared with control adhesion in the absence of fragments.

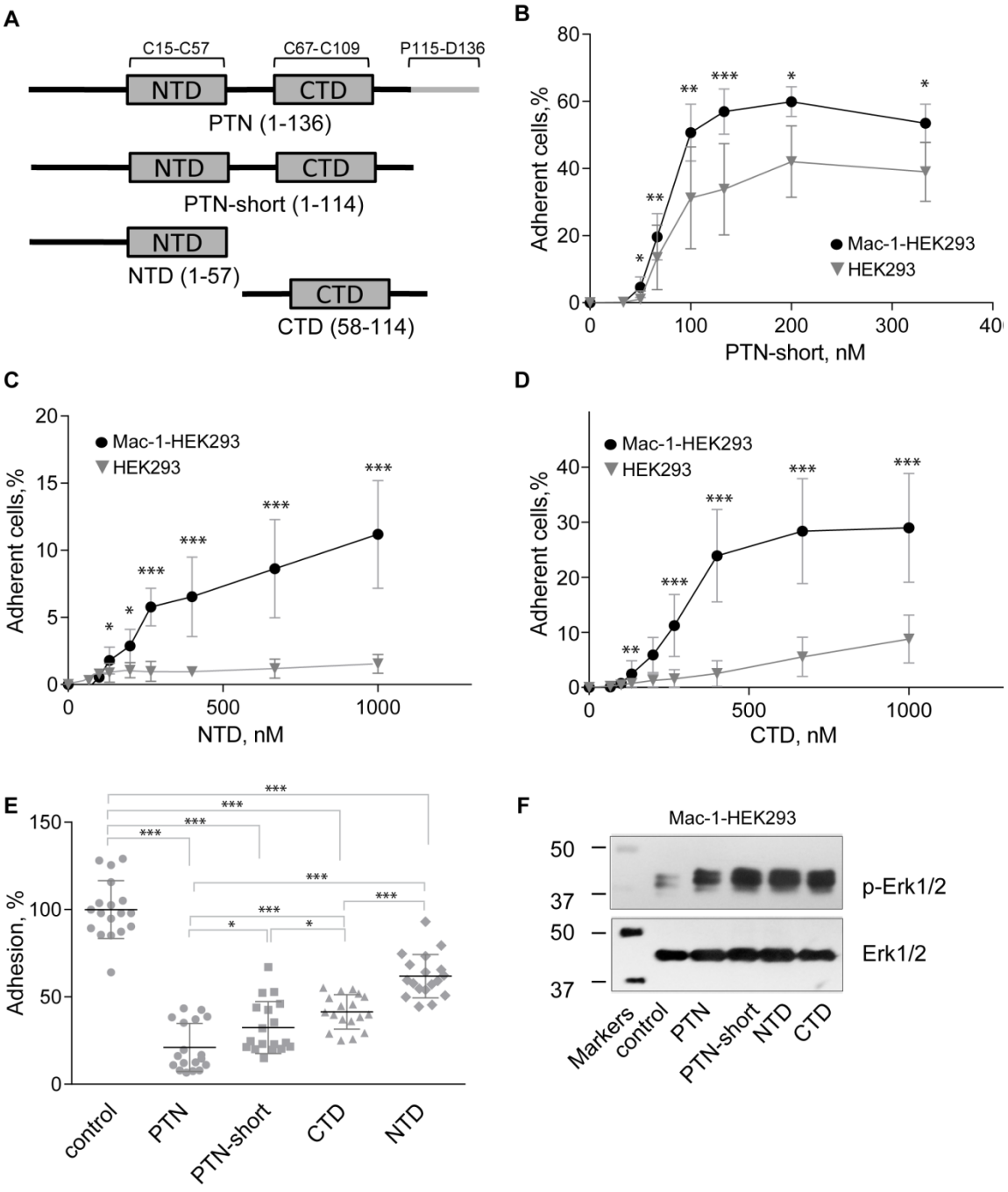

Figure 2.9 PTN Fragments Support Adhesion, Inhibit Adhesion, and Induce Erk1/2 Activation in Mac-1-expressing HEK293 Cells.

(A) A schematic representation of the domain structure of PTN and recombinant fragments used in the adhesion and Erk1/2 activation assays. (B) Aliquots (100 µl; $5x10^4$/ml) of Mac-1-HEK293 and wild-type HEK293 cells labeled with calcein were added to microtiter wells coated with different concentrations of truncated PTN without the C-terminal tail (PTN-short) and post coated with 1% PVP. After 30 min

at 37 °C, nonadherent cells were removed by washing and fluorescence of adherent cells was measured. Data shown are means ± S.E. from three separate experiments with triplicate measurements. *p≤0.05, **p≤0.01, ***p≤0.001. (C,D) adhesion assays with immobilized NTD (C) and CTD (D) were performed as described in (B). (E) Mac-1-HEK293 cells were preincubated with 5 µM PTN or PTN fragments for 20 min before loading into wells coated with 100 nM PTN and post coated with 1% PVP. Adhesion in the absence of soluble PTN or PTN fragments was assigned a value of 100%. Data shown are means ± S.E. from three separate experiments with sextuplicate measurements. *p≤0.05, ***p≤0.001 compared with control adhesion in the absence of inhibitors. (F) Mac-1-HEK293 cells were treated with 0.7 µM PTN or PTN fragments. After 30 min at 37 °C, cells were lysed, and lysates were separated using 12.5% SDS-PAGE. Western blotting was performed using the mAb specific for the phosphorylated form of Erk1/2. The mAb against total Erk1/2 was used to equalize protein loading. A representative of three experiments is shown.

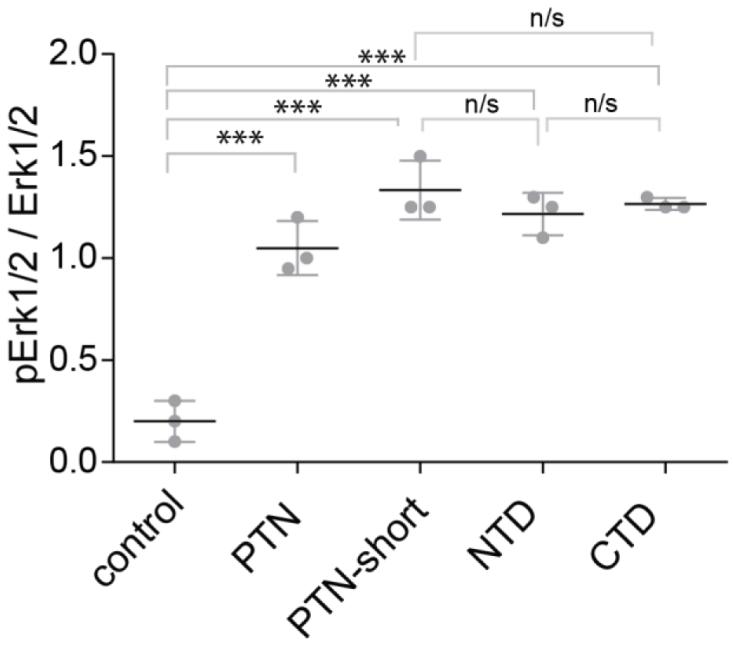

Figure 2.10 Densitometry Analysis of Western Blot Images of Erk1/2 Phosphorylation Induced by PTN in Mac-1-HEK293 Cells.
Erk1/2 activation data are shown as a ratio of the intensity of the phosphorylated Erk1/2 (pErk1/2) band to the total (Erk1/2) band. The pErk/Erk ratio for the PTN-activated lane was set to 1.0. Data shown are means ± S.E. from three separate experiments. ***p≤0.001.

2.5 Discussion

PTN is a 15-kDa basic heparin-binding protein that induces proliferation, cell growth and angiogenesis in a wide variety of cells by interacting with specific receptors, including RPTPb/ζ, ALK, N-syndecan and $\alpha_V\beta_3$ (65-67, 71, 86). PTN has also been implicated in mediating inflammation based on its ability to trigger *in vivo* migration of neutrophils and monocyte/macrophages (75, 76). In this study, we demonstrated that PTN induces a potent migratory response in macrophages in vitro and identified integrin Mac-1 as the major receptor mediating cell migration. In support of this finding, we showed that PTN induces migration of Mac-1-expressing HEK293 cells and wild-type mouse macrophages, but not wild-type HEK293 cells or Mac-1-deficient macrophages. Mac-1 expressed on HEK293 cells also augmented adhesion to PTN compared to wild-type HEK293 cells and specifically promoted cell spreading. Similarly, PTN also supported adhesion of IC-21 mouse macrophages in a Mac-1-dependent manner. In addition, Mac-1 was essential for PTN-induced activation of Erk1/2. Finally, we showed direct interaction between α_M I-domain, the ligand-binding region of Mac-1, and PTN using BLI and NMR. These observations establish PTN as a novel ligand for integrin Mac-1 and suggest a role for this protein in the pathophysiologic functions of myeloid leukocytes that specifically express this receptor.

Integrin Mac-1 is a member of the β_2 subfamily of integrin adhesion receptors and is the major receptor on the surface of neutrophils and monocytes/macrophages. This receptor contributes to leukocyte adhesion to and diapedesis through the inflamed endothelium and controls leukocyte migration to sites of inflammation. Moreover, ligand

engagement by Mac-1 initiates a variety of cellular responses, including phagocytosis, neutrophil degranulation and aggregation, expression of cytokines/chemokines and many other pro- and anti-inflammatory molecules (91, 92, 108). Innumerable roles played by Mac-1 in leukocyte biology arise from its multiligand-binding properties. Indeed, this receptor exhibits broad recognition specificity and is capable of binding an extremely diverse group of protein and nonprotein ligands. We recently showed that within its many ligands, Mac-1 binds not to a specific amino acid sequence but rather has a preference for the sequence patterns consisting of a core of positively charged residues flanked by hydrophobic residues (56). In particular, the binding motifs for Mac-1 can be coded as HyBHy, HyHyBHy, HyBHyHy, and HyHyBHyHy, where Hy represents any hydrophobic residue and B (basic) is either arginine or lysine. Other amino acids can also be found, but in general, their proportion within the Mac-1-binding motifs is very small and negatively charged (acidic) residues are largely omitted.

Analyses of the PTN sequence by a previously developed program (56) that predicts the Mac-1-binding sites in its ligands showed that PTN contains several potential α_M I-domain recognition sequences, and this prediction was confirmed experimentally (Figure 2.7). Screening of the peptide library spanning the sequence of PTN demonstrated the presence of four clusters composed of overlapping α_M I-domain binding peptides (Figure 2.7A and 2.7B). The α_M I-domain-binding peptides in clusters 2 and 3 correspond to the segments that form structural N- and C-terminal (NTD and CTD) TSR domains of PTN. Sequences in the C-terminal part of cluster 2 correspond to the segment in the hinge region (residues 58-66) connecting the TSR domains (Figure 2.7A and 2.7C).

In addition, the α_M I-domain-binding sequences identified within clusters 1 and 4 are present in the N- and C-terminal tails, respectively (Figure 2.7C). The PTN structure shows that each PTN domain possesses large basic surfaces formed by segments enriched in lysine and arginine that are brought into close proximity by PTN folding (Figure 2.11) (87). Within CTD, K68, K84, R86, K91, R92 and K107 contribute to the formation of an extended basic surface (Figure 2.11B). Within NTD, R35, R39 and K49 contribute to the basic surface on one side of the β-sheet forming the domain (Figure 2.11A). Side chains of Y69, L90, V103 and I105 in CTD form a small hydrophobic cluster in the middle of CTD (87). Furthermore, F63 in the hinge segment that connects NTD and CTD has significant contacts with side chains of residues in the hydrophobic cluster. Because of these interactions, the bend formed in the hinge places K60 and K61 close to the basic surface in CTD (Figure 2.7C). Interestingly, all of the residues forming the basic surfaces in CTD and NTD as well as those found in the hydrophobic cluster and the hinge were found in the α_M I-domain binding clusters 2 and 3, and two residues (V103 and K105) in the beginning of cluster 4. Since basic and hydrophobic amino acid residues were shown to be the main contributors to the interaction between the α_M I-domain and peptides in the previously screened libraries of Mac-1 ligands (56, 90, 109) it is possible that the basic surfaces in CTD and NTD form the binding sites for the α_M I-domain. The identification of the majority of the α_M I-domain binding residues in NTD and CTD is in agreement with the NMR data showing many residues in these domains were perturbed in the presence of α_M I-domain (Figure 2.6).

To validate the relevance of the proposed Mac-1 binding sites, we investigated the adhesion of Mac-1-expressing HEK293 cells to truncated PTN fragments. The results showed that immobilized NTD and CTD can independently support Mac-1-dependent adhesion and soluble NTD and CTD can inhibit cell adhesion to intact PTN, albeit to a lower extent than soluble intact PTN (Figure 2.9B-E). Interestingly, removal of each NTD or CTD domain reduced PTN's affinity for cell surface proteoglycans to a greater extent than its affinity for Mac-1 (Figure 2.9C, 2.9D), suggesting that proteoglycans are involved but not absolutely required for adhesion. Based on these data, it is reasonable to propose that each of the two structural domains of PTN can bind Mac-1 independently. Furthermore, it appears that both domains of PTN are required for the optimal proteoglycan binding and thus, the enhanced adhesion of Mac-1-expressing cells to intact PTN may result from the cooperative binding of Mac-1 and proteoglycans.

Consistent with the role of proteoglycans in Mac-1-mediated cell adhesion, previous studies demonstrated that soluble heparin partially blocks the adhesion of Mac-1-expressing cells, including human monocytes to various ligands (44, 90, 109). Moreover, the inhibitory effect of anti-Mac-1 function-blocking reagents has been potentiated by heparin. We observed similar effects of heparin and anti-Mac-1 function-blocking mAb 44a on the adhesion of Mac-1-HEK293 cells to PTN (Figure 2.1). Heparin also partially inhibited the migration of Mac-1-HEK cells. However, in contrast to adhesion, mAb 44a completely inhibited migration even in the absence of heparin, indicating that Mac-1 was absolutely required for migration (Figure 2.3C and 2.3D). These findings suggest that although HSPGs may influence cell migration in this system,

PTN engagement by Mac-1 is indispensable for triggering intracellular signaling that initiates migration. Heparin may exert its inhibitory effect by binding to the heparin-binding sites in PTN or by interacting with Mac-1. Indeed, both NTD and CTD of PTN contain sites that bind heparin with high affinity (89, 110). Furthermore, heparin has also been shown to interact with the α_M I-domain of Mac-1 (111), although the binding site(s) remains uncertain. These findings suggest that, if present, HSPGs on leukocytes may participate in optimal adhesion and migration to PTN. Moreover, PTN has a high affinity for chondroitin sulfate (CS) A and E with a Kd in the low nM range (89, 110). This suggests that CS, which, similar to heparin, is covalently attached to several core proteins creating a variety of CSPGs on the cell surface, can act cooperatively with Mac-1. The complex relationship between PTN, Mac-1 and cell surface HS/CS proteoglycans remains poorly understood. Since PTN contains two glycosaminoglycan-binding sites in NTD and CTD and can bind the α_M I-domain through the same basic surfaces, it may potentially bridge Mac-1 and proteoglycans inducing their clusterization. The additional binding site for glycosaminoglycans in the C-terminal tail of PTN may also participate in the formation of complexes between Mac-1 and HS/CSPG, further increasing the complexity of multi-molecular clusters. Given noticeable differences in the affinity of PTN domains for glycosaminoglycans, it is reasonable to propose that this variability may influence the interactions of PTN with Mac-1 on leukocytes and thus affect cell adhesion, migration and other Mac-1-dependent leukocyte responses. Interestingly, while HSPGs on Mac-1-expressing HEK293 cells and human monocytes (44) cooperate with Mac-1 in PTN binding, their role in adhesion of IC-21 mouse macrophages appears to be

less important since heparin alone does not inhibit adhesion while anti-Mac-1 mAb produces a strong inhibitory effect (Figure 2.1E). The reason for the differential involvement of proteoglycans in PTN recognition is unclear but may stem from differences in the composition of glycosaminoglycans expressed on various cells. In addition to cell surface proteoglycans, ECM proteoglycans may also play a role in the storage and presentation of PTN to migrating cells. In this regard, we showed that PTN bound to aggrecan, a well-known CSPG in the ECM, supports adhesion, suggesting that PTN deposited in the ECM remains an active Mac-1 ligand.

Binding of several ligands to Mac-1 is controlled by the activation state of the receptor. Previous studies demonstrated that the α_M I-domain exists in two different conformations, active and nonactive, with the position of the C-terminal α7 helix regulating its activation state (59). In contrast to such Mac-1 ligands as C3bi, recognition of which requires the active state of the α_M I-domain (112), the nonactive form of the α_M I-domain bound PTN, albeit to a lower extent than active α_M I-domain (Figure 2.5C). This finding suggests that the α_M I-domain binding to PTN is not strictly activation-dependent. Furthermore, in contrast to other integrin ligands, binding of PTN to the active α_M I-domain still occurred in the absence of Mg^{2+} or in the presence of EDTA (Figure 2.5C). Similar characteristics, i.e. the lack of dependence on the activation state of the α_M I-domain and divalent cations, have been noted with some Mac-1 ligands, including opioid peptide dynorphin A (90), fibrinogen peptide P2-C (96) and cationic proteins myeloperoxidase and elastase (unpublished data). Since all these molecules are highly positively charged and their binding to the α_M I-domain is mediated by sequences

enriched in basic residues (56), it is tempting to speculate that cationic peptides/proteins represent a unique group of Mac-1 ligands that bind the α_M I-domain through activation- and cation-insensitive mechanisms. Further structural studies of the α_M I-domain-PTN complex may help to define the mechanism of this interaction.

Although the biological significance of leukocyte interaction with PTN remains to be established, the expression of PTN in different cells during regeneration after injury (64, 113) suggests that it may play a role in inflammatory responses. In this regard, PTN has been shown to promote neutrophil and monocyte/macrophage recruitment during liver regeneration and peritoneal fibrosis (75, 76). Our *in vitro* studies showing that Mac-1 can mediate migration of macrophages and Mac-1-expressing HEK293 cells to PTN suggests that leukocyte migration in vivo may also be driven by this receptor. Furthermore, the only known PTN homolog, midkine (MK), which shares 50% sequence identity and a similar tertiary structure with PTN, is expressed in damaged tissues and has a comparable pro-inflammatory profile (114). It has been reported that MK enhances the migration of inflammatory leukocytes in a number of pathological conditions induced in experimental animals (76, 115-119) MK receptors responsible for triggering these responses are not known, but MK has been shown to activate both β_1 and β_2 integrins (119, 120). Furthermore, adhesion to immobilized MK was shown to be mediated by β_2 integrins, although the nature of α subunit pairing with the β_2 subunit has not been determined. Both PTN and MK have also been shown to induce the expression of inflammatory cytokines in peripheral blood monocytes (114, 121). Since ligand engagement by Mac-1 is known to initiate intracellular signaling that regulates numerous

leukocyte responses, including expression of cytokines, a receptor that mediates this effect upon PTN and MK binding is most likely to be Mac-1. The potential role of PTN in inducing other reactions of monocyte/macrophages that are known to be mediated by Mac-1 merits further investigation.

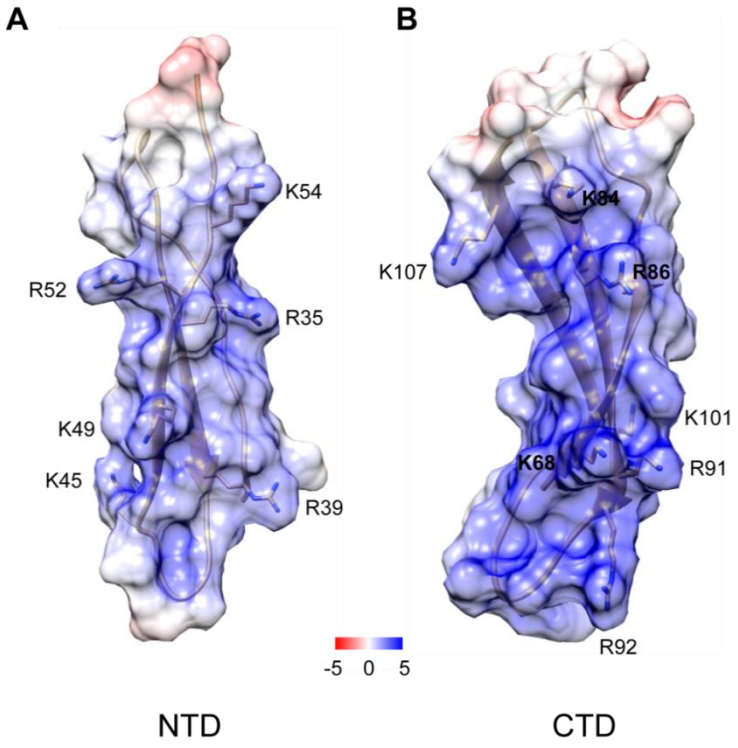

Figure 2.11 Location of the α_M I-domain Binding Residues in NTD and CTD of PTN. Electrostatic potential mapped onto the ribbon diagram of NTD (A) and CTD (B). The unit of potential is in kT·e-1. Positively charged residues identified in the α_M I-domain binders using peptide libraries are shown. The PTN models are based on PDB: 2N6F.

CHAPTER 3

THE ROLE OF α_M I-DOMAIN STRUCTURAL DYNAMICS ON ITS INTERACTIONS WITH CATIONIC LIGANDS

3.1 Abstract

α_M I-domain, the crucial ligand-binding domain on the leucocyte integrin $\alpha_M\beta_2$, exists in open and closed conformations, which have been proposed to represent active and inactive conformations, respectively. Canonically, it has been widely accepted that ligands bind to α_M I-domain's metal ion-dependent adhesion site (MIDAS) through the coordination of a divalent cation such as Mg^{2+}. However, for $\alpha_M\beta_2$, the most promiscuous integrin, this metal-dependent binding mechanism cannot explain all the interactions between $\alpha_M\beta_2$ and ligands. By performing biophysical binding assays, we found that a unique class of cationic ligands, including the cytokine: pleiotrophin and the chemokine: platelet factor 4, could bind to α_M I-domain through a metal independent mechanism. In addition, the divalent metal exerts opposite influences on the ligand binding of active and inactive α_M I-domains. Specifically, Mg^{2+} inhibits ligand binding of inactive α_M I-domain but enhances the ligand binding of active α_M I-domain. Protein stability and conformation dynamic studies confirmed that the active α_M I-domain displayed a higher dynamic and less thermostability compared to the inactive α_M I-domain. We propose that divalent metal affects the dynamics of active and inactive α_M I-domain in distinct ways. In particular, metal ion stabilizes the active conformation without completely eliminating the electronegativity of MIDAS required to bind the ligands while its interaction with the inactive α_M I-domain neutralizes the charges in MIDAS. As a result, adding the proper

amount of Mg^{2+} improved the cationic ligand binding for active α_M I-domain while hindering the cationic ligand binding for inactive α_M I-domain. These studies defined a novel binding mechanism for cationic ligands, established the structure-function-dynamics correlation for α_M I-domain, and demonstrated the versatile roles of metal ions on integrin.

3.2 Introduction

Integrins are cell surface adhesion receptors formed by two non-covalently associated αβ heterodimers that play many crucial roles in cellular functions including cell adhesion, cell migration, cell differentiation and immune response (122). As the previous chapter introduced, both integrin αβ subunit consists of a large multicomponent extracellular domain, a single membrane-spanning helix and a short unstructured cytoplasmic tail (5). Half of the integrin α-subunits contain an inserted domain at the top of the extracellular region referred to as the α I-domain or von Willebrand factor A-type domain, which is believed to be the major ligand-binding site for these integrins (123-125). In integrins lacking the α I-domain, the homologous β I-domain plays a similar role as α I-domains in ligand binding (126). Thus, the study of the ligand and I-domain interaction mechanism becomes essential to understanding the activity of integrins.

Integrin $\alpha_M\beta_2$ (Mac-1, CR3, CD11b/CD18) is an α I-domain-containing integrin expressed on leukocytes like the myeloid, natural killer, and T cells (127-129). $\alpha_M\beta_2$ mediates diverse functions on immune cells such as cell extravasation, phagocytosis and immune synapse formation (130). Similar to other α I-domains, the α_M I-domain plays a pivotal role in $\alpha_M\beta_2$ integrin activation. To better understand the function mechanism of

the α_M I-domain, researchers naturally turned their focus to the structure of the α_M I-domain. α_M I-domain adopts a classic dinucleotide binding or Rossmann fold in which a core of β-sheets are surrounded with several α-helices (58). In particular, there are 6 β-strands and 7 α-helices in the protein, and they are arranged in an alternating fashion linked by flexible loops (Figure 3.1A). At the top face of the α_M I-domain, there is the well-known ligand binding site called metal ion-dependent adhesion site (MIDAS) which coordinates a divalent metal ion and forms the ligand-binding site. α_M I-domain has been crystallized in two conformations termed closed and open (58, 59). And additional studies demonstrated that the close and open conformations correspond to the low ligand affinity inactive state and high-affinity active states, respectively (61, 131). The crystal structures show two major differences between inactive and active α_M I-domain: the position of α7 helix and the metal coordinating residues in the MIDAS (Figure 3.1). Compared to inactive α_M I-domain, the α7 helix of active α_M I-domain is shifted downward by 10 Å as shown in Figure 3.1B. This axial displacement of the α7 helix has been proposed as the critical step for the transmission of a conformational signal between the α I-domain and other integrin domains (95). When this shift happens, glutamate in the C-terminal region of α I-domain moves and is inserted into the β I-domain as an intrinsic ligand and induces structure rearrangement of the entire integrin, resulting in integrin activation.

In addition, this large movement of α7 helix also causes metal coordination changes of the residues in MIDAS. In the active α_M I-domain MIDAS, five residues are involved in metal cation binding (Figure 3.1A). In the active conformation, three neutral

amino acids (threonine 209, serine 142 and serine 144) directly coordinate cations and 2 acidic amino acids (aspartic acid 140 and aspartic acid 242) are free. However, in an inactive conformation, threonine 209 is replaced by aspartic acid in MIDAS. This change in MIDAS also results in electrostatic potential surface changes. Thus, the active α_M I-domain exposes more negative charges than inactive α_M I-domain because of the free acidic amino acids.

A previous study has shown that deleting a short sequence after I316 forces the α_M I-domain to adopt the active conformation (132). And the data showed that this truncated active α_M I-domain can bind to the ligand with ~500-fold stronger than wild type inactive α_M I-domain. The researchers believed that the disruption of I316 hydrophobic intramolecular socket is essential to activating the α_M I-domain.

Base on the crystal structure, the electrostatic potential surface of the α_M I-domain can be calculated in the absence of metal. As shown in Figure 3.1C, most of the α_M I-domain solvent-exposed surface exhibited positive charges, whereas a negative charge patch is found in the MIDAS of the α_M I-domain. It is commonly accepted that the binding of divalent cations (such as Mg^{2+} or Mn^{2+}) to MIDAS is essential for many ligand binding (58, 112, 123, 125, 133). And many physiological ligands bind to the α_M I-domain in a divalent cation-dependent manner. As mentioned before, three polar and two acidic amino acids coordinate the divalent cation in the MIDAS (Figure 3.1A) of active α_M I-domain. When the ligand binds to an α I-domain, the divalent cation binds to MIDAS with those coordinating residues, and then the solvent-exposed glutamic acid

from the ligands binds to the cation embedded in MIDAS (134). In this mechanism, the cation serves as a bridge between ligand and α_M I-domain.

As the most promiscuous integrin, the $\alpha_M\beta_2$ has a really broad recognition specificity of many dissimilar ligands, many of which contain no acidic amino acids (37). The molecular mechanism of why $\alpha_M\beta_2$ has this diversified ligand recognition ability is not clear. Compared to other integrins, $\alpha_M\beta_2$ integrin is unique in that it not only binds to those metal-dependent ligands but it also can bind to different cationic ligands which contains a lot of basic amino acids, such as pleiotrophin and platelet factor 4 (57, 135). In fact, a recent study showed that a key feature of the α_M I-domain recognition motif is a small core composed of basic amino acids flanked by hydrophobic residues (56). This raises the question of what the binding mechanism for those cationic ligands is and how does divalent cation affect this binding.

In this research, we have studied the α_M I-domain and ligand interaction from two aspects. First, we have characterized and compared the dynamics and stability differences between active α_M I-domain and inactive α_M I-domain. And second, we investigated the binding mechanism between α_M I-domain and two cationic ligands, PTN and PF4. Our data showed that, compared to the inactive α_M I-domain, the active α_M I-domain is more dynamic and less stability, especially on α7 helix. These results proved that disrupting the I316 hydrophobic core and the C-terminal causes the increase of flexibility to α_M I-domain. We also studied the thermostability difference between the two conformations of α_M I-domain in the presence and absence of Mg^{2+}. The results revealed that the active α_M

I-domain is less stable than inactive α_M I-domain in both conditions, but the Mg^{2+} presented stronger stabilization effect on active α_M I-domain than on inactive α_M I-domain.

Furthermore, we explored the binding mechanism between the α_M I-domain and two cationic ligands. And our data showed that both PTN and PF4 bind to α_M I-domain through a novel metal independent mechanism in which metal is not required for the binding. Surprisingly, although the divalent cation is not necessary for cationic ligand binding, Mg^{2+} shows different effects on active and inactive α_M I-domain's interactions with cationic ligands. For active α_M I-domain, Mg^{2+} played a positive role by increasing cationic ligand binding affinity. In the case of inactive α_M I-domain, Mg^{2+} inhibited the cationic ligand binding. These studies established the structure-function-dynamics correlation for integrin α_M I-domain, defined a novel binding mechanism for cationic ligands, and demonstrated the versatile roles of metal ions on integrin which enhanced our understanding of integrin $\alpha_M\beta_2$ functional diversity.

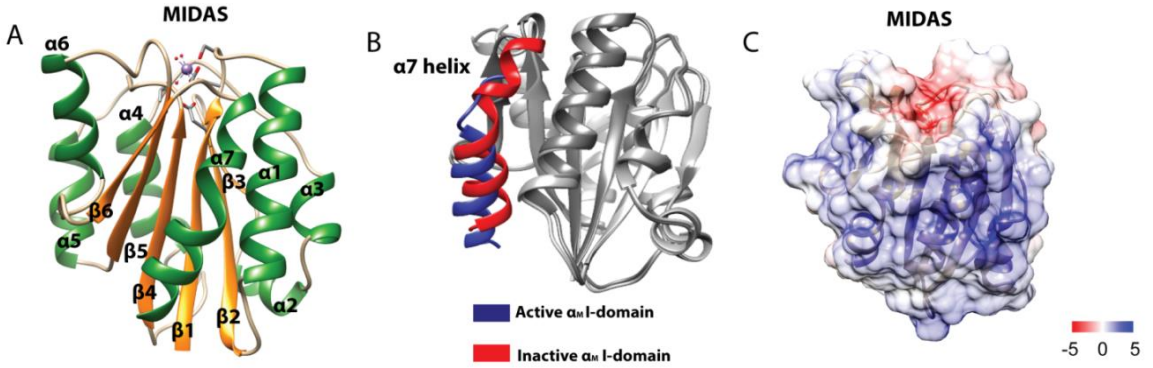

Figure 3.1 Integrin α_M I-domain
(A) Ribbon structure of inactive integrin α_M I-domain with Mn^{2+} in MIDAS (PDB code: 1jlm). The secondary structures of α helix and β stand are labeled with green color and orange color separately. (B)The comparison between active and inactive α_M I-domain. Active α_M I-domain α7 helix (blue) shifts downward by 10 Å compared to inactive α7 helix (red). (C) The inactive α_M I-domain electrostatic potential surface mapped onto the ribbon diagram. The negative charge was labeled by red color and the positive charge was labeled by blue color. The electrostatic potential was calculated in absence of metal ion. The unit of potential is in $kT \cdot e^{-1}$.

3.3 Materials and Methods

1, Expression and purification of recombinant proteins

The open reading frame (ORF) of the human inactive α_M I-domain (Q119-E333) and active α_M I-domain (E123-K315) were cloned into the pHUE vector as a fusion protein with His-tagged ubiquitin at its N-terminus using SacII and HindIII as restriction sites(97). The expression vectors were transformed into BL21 (DE3) cells. For inactive α_M I-domain expression, the BL21 (DE3) cells were grown to OD_{600} of ~ 0.8 in the M9 medium at which point the culture was induced with 0.5 mM IPTG and harvested after overnight expression at 23 °C. In the case of active α_M I-domain, 0.25mM IPTG was applied at cell OD_{600} of ~ 0.5 with the overnight culture at 20 °C. To prepare isotopically

labeled proteins, NH_4Cl was replaced by $^{15}NH_4Cl$ in M9 media. Cell pellets were centrifuged and resuspended in lysis buffer (20 mM sodium phosphate, 0.5 M NaCl, 10 mM imidazole, 5% glycerol, 0.01% NaN_3). Further, the cells were treated with1mg/mL lysozyme and incubated for 20 min on ice followed by sonication and centrifugation. Then, the supernatant was collected and subjected to Ni-affinity chromatography using a 5mL HisTrap column (GE Life Sciences). The protein was eluted with an imidazole gradient of 35 to 500 mM at a flow-rate of 3 mL/min. The eluted fusion proteins (His-tagged-ubiquitin-integrin α_M I-domain) were buffer exchanged into the USP2 digest buffer (25 mM Tris and 100 mM NaCl, pH 8.0) and digested by 1/20 molar equivalent of His-tagged USP2 ubiquitinase overnight at room temperature to remove the ubiquitin-His tag from the fusion protein (97). Then, the mixture was passed through a second Ni-affinity column to isolate the cleaved α_M I-domain from ubiquitin, USP2 ubiquitinase, and undigested fusion protein. The cleaved α_M I-domain was collected from flow-through and further applied on Superdex 75 size exclusion chromatography column (GE Life Sciences) to remove the aggregation and other impurities. The purity of the final product was confirmed using SDS-PAGE electrophoresis.

PTN expression and purification were performed in the same way as mentioned in chapter 2 (87). Briefly, the pET-15b vector containing human PTN ORF was transformed into Origami B (DE3) cells (Novagen, Madison, WI, USA). Cells were grown in M9 medium and induced with 0.25 mM IPTG at OD_{600} of 0.5. The PTN was released from the cell pellets and purified with 5mL HiTrap SP HP column and 5mL HiTrap Heparin

HP affinity columns (GE Healthcare Life Sciences). The purified PTN was buffer exchange to 20 mM sodium bicarbonate buffer pH 7.0 and lyophilized before use.

Platelet factor 4 (PF4, CXCL4) (E1-79S) ORF was cloned into pET-15b in a similar manner as PTN and recombinantly expressed in Origami B (DE3) using the same procedure (87). PF4 was purified using a 5mL HisTrap Heparin HP affinity column (GE Life Sciences) and eluted with a 0.1 to 2 M NaCl gradient. The fractions containing PF4 were buffer exchanged to a buffer of 20 mM acetate, 150 mM NaCl, pH 5.0. The purified PF4 was verified with SDS-PAGE and lyophilized before use.

2, Microscale thermophoresis (MST)

The binding between different versions of α_M I-domain and PTN or PF4 was measured by microscale thermophoresis (MST) in the presence and absence of Mg^{2+}. The MST experiments were performed on the Monolith NT.115 instrument (Nanotemper). First, the α_M I-domains were labeled with DyLight 488 NHS Ester dyes (Thermo Scientific) following the protocol provided by the manufacturer. In brief, the powder of fluorescent dye (DyLight 488 NHS-Ester) was dissolved to 10 mg/ml in DMF before use. The α_M I-domain was buffer exchange to labeling buffer (0.05M sodium borate, pH 8.5) and concentrated to 5 mg/ml. For the optimal labeling efficiency (1~2 fluorophores per protein molecule), the protein was mixed with five molar equivalents of DyLight 488 NHS-Ester and incubated at room temperature for one hour. Too much dye or incubate too long will cause the over-labeling. The crosslink reaction was stopped by adding 1M Tris. The free dyes were then removed by buffer exchange to 20 mM HEPES and 100mM NaCl, pH 7.0 buffer. The degree of labeling was measured based on the protocol

from the manufacturer. For PTN binding test, each titration sample was made by 50 nM DyLight 488-labeled α_M I-domain and 0 to 400 μM PTN in the buffer of 20 mM HEPES, 100 mM NaCl, 0.05% Tween 20, pH 7.0 with or with Mg^{2+}. For PF4 titrations, the samples were prepared in 10mM HEPES, 10 mM acetate, 125mM NaCl, pH 6.0 buffer. The low pH condition is necessary for preventing PF4 precipitation. The samples were loaded into standard treated MST capillaries (Nanotemper) and tested at room temperature. Data were collected from at least three trials and the error was representing the standard deviation from different trials. The dissociation constant (Kd) was calculated by fitting the plot of normalized changes in fluorescence (ΔF_{norm}) versus the concentrations of the ligand with the equation of $f(L) = Unbound + \frac{(Bound-Unbound)\times(L+P+Kd-\sqrt{(l+P+Kd)^2-4\times L\times P)}}{2\times P}$ in which "Bound" represents the MST response value of saturated point, Unbound is the response value of with no ligand, L was the ligand concentration, P was the concentration of α_M I-domain.

3, HPLC size exclusion liquid chromatography

To characterize the aggregation state of different versions of α_M I-domain, analytical size exclusion liquid chromatography was performed on a Shimadzu HPLC system (Columbia, MD). The purified protein was concentrated to 50μM and loaded on to Tosho TSKgel G3000SW column. The mobile phase consisted of 20 mM HEPES, 300 mM NaCl, 0.02% sodium azide in pH 7.0. The column was maintained at 25°C and performed at a flow rate of 0.5 ml/min. All the elution was monitored by UV absorbance at 280 nm. To estimate the size of protein, the Protein Standard Mix (15-600 kDa) (Sigma-Aldrich) was used for comparison.

4, Circular dichroism (CD) spectroscopy

The thermostability of the α_M I-domain was characterized by circular dichroism (CD) spectroscopy using Jasco J-710 spectropolarimeter (Jasco Inc., Japan). For measuring the complete spectra of folded active and inactive α_M I-domain, 20 μM of protein sample, in 20 mM HEPES, 100 mM NaCl, pH 7.0 buffer, was loaded in a 0.1 cm cuvette and the spectra were recorded in a wavelength range of 200–250 nm at a 50 nm/min scan rate at room temperature. The HEPES buffer was used as negative control. Each spectrum was obtained by repeating five scans. Further, the temperature-induced protein unfolding was studied by measuring the intensity change of the CD signal at the wavelength of 222 nm with the increasing of the temperature. Because 20 μM α_M I-domain would precipitate at higher temperatures, the protein concentration was lowered to 2 μM to keep protein soluble. In order to obtain sufficient signal-to-noise, a 0.2 cm cuvette was used in protein unfolding experiments. During the test, the sample was heated from 25℃ to 65℃ with a rate of 1℃ per minute, and the sigmoid fitting curve of ellipticity as a function of temperature was used to determine the melting temperature (Tm) of protein by the PRISM software.

5, Molecular dynamics (MD) simulation

The initial structures for MD simulation of active α_M I-domain and inactive α_M I-domain were from crystal structure with PDB code 1ido and 1jlm. All the simulations were conducted using the AMBER 16 software package (136). The original PDB file was converted to AMBER recognized PDB file using pdb4amber from AMBER 16 package. The force field ff15ipq was applied (137), the protein was solvated in TIP3P water and

$6Cl^-$ $2Na^{2+}$ ions were added using the LEap program. The solvated proteins were equilibrated with a short simulation (50ns). Then, ~1 μs MD simulations with a time-step of 2 fs were performed for both protein systems. The simulation trajectories were analyzed with VMD software. The atom's root-mean-square deviation (RMSD) and (root-mean-square fluctuation) RMSF, from trajectories during the time change, were calculated with tools in VMD.

6, NMR

^1H-^{15}N HSQC NMR data of different versions of α_M I-domain were collected using a Bruker 600 MHz Avance III HD spectrometer (Bruker Instrument, Inc. Billerica, MA, USA) equipped with a Prodigy probe. For the NMR sample, ~0.1-0.5 mM of isotropic labeled protein sample was dissolved in HEPES buffer containing 20mM HEPES, 100mM NaCl, pH 7.0 and 5% D_2O. The 2D HSQC were processed using NMRPipe (100) and analyzed with NMRView (101).

7, Crystallization of active α_M I-domain and PTN complex

Recombinant active α_M I-domain and PTN were expressed and purified as described previously. 10mg/ml of α_M I-domain and 10mg/ml of PTN were mixed in 20mM HEPES, 2mM $MgCl_2$, 300mM NaCl, pH7.0 buffer. The crystal was grown by sitting-drop vapor-equilibration against 0.1 M Potassium chloride, 0.025 M Magnesium chloride hexahydrate, 0.05 M Sodium cacodylate trihydrate pH 6.0, 15% v/v 2-Propanol at 12 °C. And the crystal scattering pattern data was collected from the Advanced Photon Source (APS) at Argonne National Laboratory (IL, US).

3.4 Results

1, Purification and characterization of active and inactive α_M I-domain

We have successfully cloned active α_M I-domain (E123-K315) and inactive α_M I-domain (Q119-E333) ORF into the pHUE vector and expressed them in the *E.Coli* BL21(DE3) cells. Although both constructs showed a high level of expression (Figure 3.2A), much of the active α_M I-domain was insoluble and accumulated in inclusion bodies compared to inactive α_M I-domain. In order to make more soluble active α_M I-domain, we optimized several parameters in culture conditions. During active α_M I-domain expression, 2 g/L of glucose which is half the amount of glucose in regular M9 medium was used. And a low concentration of IPTG (0.25mM) was used for induction. In addition, the lower growth temperature (18°C) was applied to farther decrease the rate of cell growth in order to reduce protein synthesis rate and reduce inclusion body formation. Although these optimizations improved protein solubility to a certain degree, the yield of active α_M I-domain is still much less than inactive α_M I-domain. This may be because of the low stability of the active α_M I-domain. The fusion protein was first purified by Ni-column and then digested with USP2 ubiquitinase to remove the His-Tags. The digested proteins were further purified using the Superdex75 size exclusive column to remove remnants of ubiquitin, α_M I-domain aggregation or other impurities (Figure 3.2B). The eluted fractions were run on SDS- PAGE to identify the target protein (Figure 3.2C). As shown in the size exclusive chromatogram (Figure 3.2B), there were much more large size impurities in active α_M I-domain samples than inactive α_M I-domain labeled as peak 1. From the SDS-PAGE, we can see that the target protein α_M I-domain

was eluted as the major peak (peak 2), and the residual ubiquitin was eluted later at peak 2. The fractions from peak 2 were combined and used for further studies.

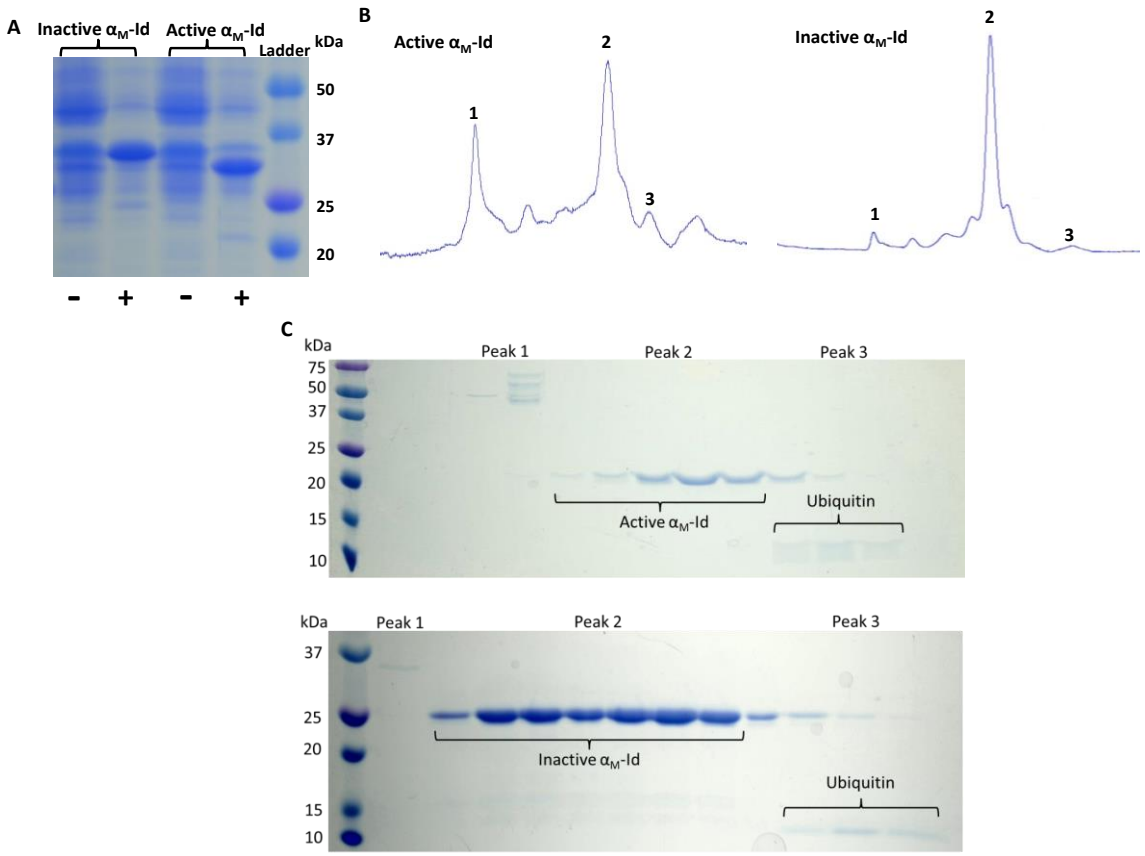

Figure 3.2 The Purification of Active and Inactive α_M I-domain
(A)The gel electrophoresis of before and afterinduction from active an inactive α_M I-domain culture. (-) and (+) represent the cell culture with and without IPTG induction respectively. (B) Chromatogram of active and inactive α_M I-domain on Superdex 75 SEC column, the α_M I-domain was eluted at peak 2. (C) The gel electrophoresis of the fractions from Superdex 75 SEC column.

In addition, the oligomerization states of purified active α_M I-domain and inactive α_M I-domain were analyzed by the analytical HPLC size exclusive chromatography. The Monomeric active and inactive α_M I-domains have a molecular weight of 22 and 25 kDa respectively. By comparing α_M I-domain retention time to the retention time of protein standards, we can estimate the size of the α_M I-domain. Here, we observed that both active and inactive α_M I-domain chromatograms contained a single peak at retention time at around 22 min. And these results indicated that both active and inactive α_M I-domain should be in the monomeric state (Figure 3.3).

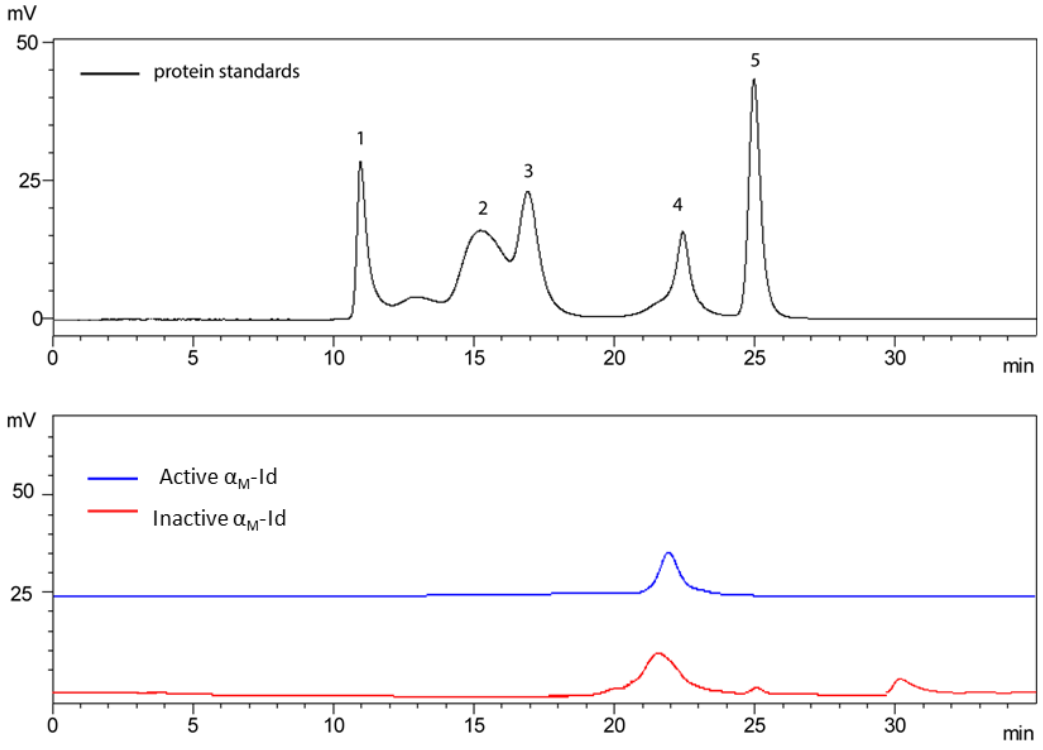

Figure 3.3 Chromatograms from Tosho HPLC SEC Column
The first chromatogram is from the protein standards and the number on each peak indicates different proteins as followed: 1. Thyroglobulin (670 kDa), 2. γ-globulins (150 kDa), 3. Albumin (44 kDa), 4. Ribonuclease A(14 kDa), 5. 4-Aminobenzoic acid (0.137 kDa). The bottom chromatogram shows the elution of active α_M I-domain (22kDa) in blue color and the inactive α_M I-domain (25kDa) in red color. The molecular weights here are theoretical molecular weights.

3, The dynamics of active and inactive α_M I-domain

Because we noticed that active α_M I-domain displayed much lower solubility and stability compared to inactive α_M I-domain, we were interested in investigating the source of the discrepancy between active and inactive α_M I-domain. The previous crystal structures had shown that active α_M I-domain and inactive α_M I-domain exhibited a remarkable difference in the position of α7 helix (Figure 3.6C) (59). However, there is no research on differences in the dynamics of active α_M I-domain and inactive α_M I-domain in the solution state. Here, we collected the solution NMR spectra from active α_M I-domain and inactive α_M I-domain. Surprisingly, the active α_M I-domain demonstrated much worse ^{1}H-^{15}N HSQC spectral quality comparing with inactive α_M I-domain HSQC (Figure 3.5) considering the peak dispersion, line widths, and the numbers of the observable peaks. We proposed that the poor spectral quality of the active α_M I-domain is caused by the structural dynamics.

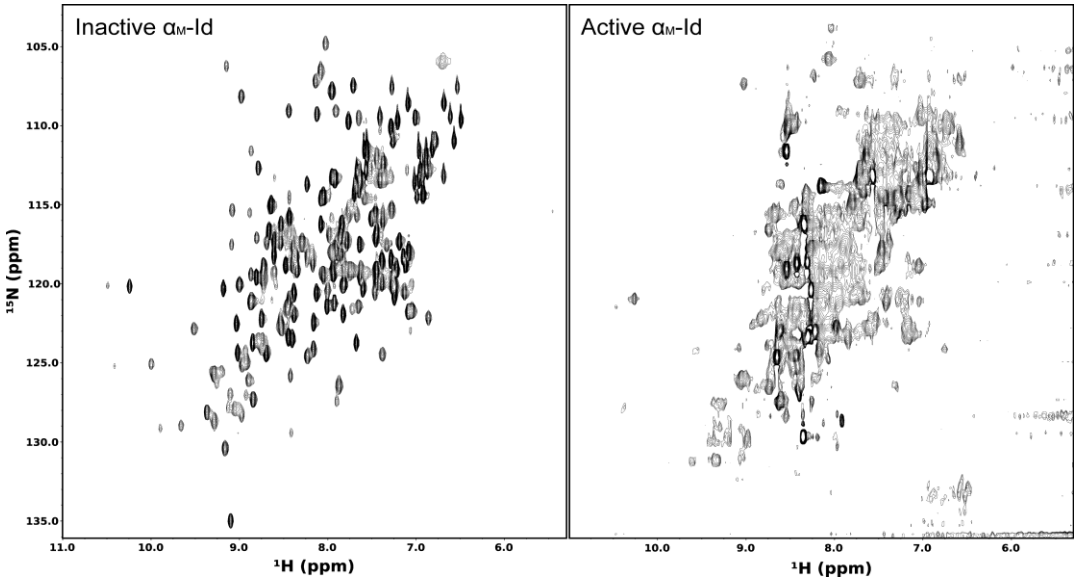

Figure 3.4 Comparison of Inactive and Active α_M I-domain ^{1}H-^{15}N HSQC Spectra.

To further confirm the theory that the active α_M I-domain is more dynamic than the inactive α_M I-domain which caused the NMR spectra quality to decline, we performed MD simulation on active and inactive α_M I-domain using their crystal structures as the initial structures. The simulations were carried out for 1μs with the AMBER MD simulation packages. To analyze the protein stability in the simulation data, we calculated the root-mean-square fluctuation (RMSF) on different parts of protein through all the trajectories (138). Figure 3.5 shows the RMSF results from the MD simulation ensemble of 1 μs trajectories. The amplitudes in the plots are indicators of the atom fluctuations in certain regions, which are labeled with various color boxes and on structures. Generally, the high RMSF values were seen in the loop regions in both active and inactive α_M I-domain. However, the active α_M I-domain showed more residues with higher RMSF values compared to the inactive α_M I-domain. This indicated that active α_M I-domain is globally more flexible than inactive α_M I-domain.

Moreover, active α_M I-domain exhibited strong dynamic motions on α7 helix which has not occurred in inactive α_M I-domain MD simulation. To illustrate this difference, we calculated the root-mean-square deviation (RMSD) value of residues in α7 helix for both simulation trajectories (Figure 3.6A). The mean value of α7 helix residue RMSD of active was 3.91Å and for inactive α_M I-domain, the value was 1.77 Å. Figure 3.6B shows the RMSD probability distribution from two simulations. It is obvious that the RMSD distribution of α7 helix on active α_M I-domain shifted significantly to right with lager value than inactive α_M I-domain.

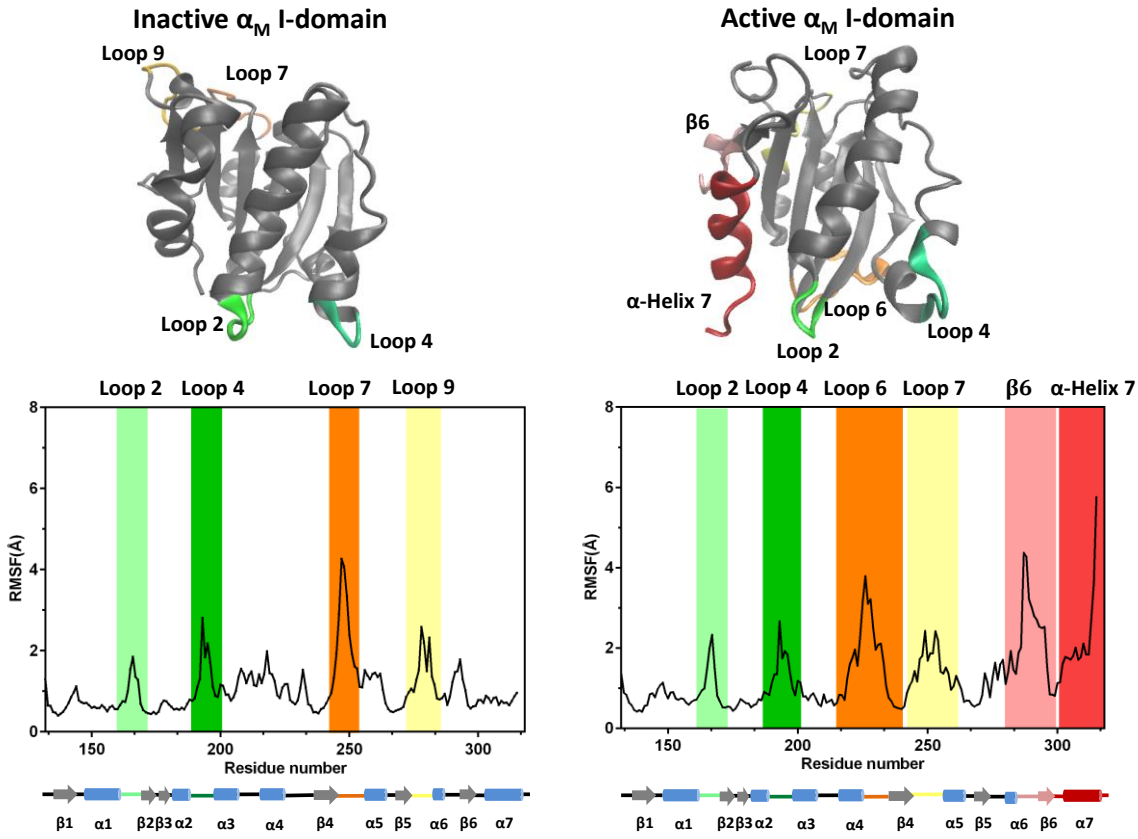

Figure 3.5 Comparison of the Root-mean-square Fluctuation (RMSF) of the Amino Acid Residues from MD Simulation Trajectories.
The regions with RMSF ≥ 2 Å are highlighted with different colors and labeled in structures. The data from inactive α_M I-domain are shown on left side and the active α_M I-domain are on right side.

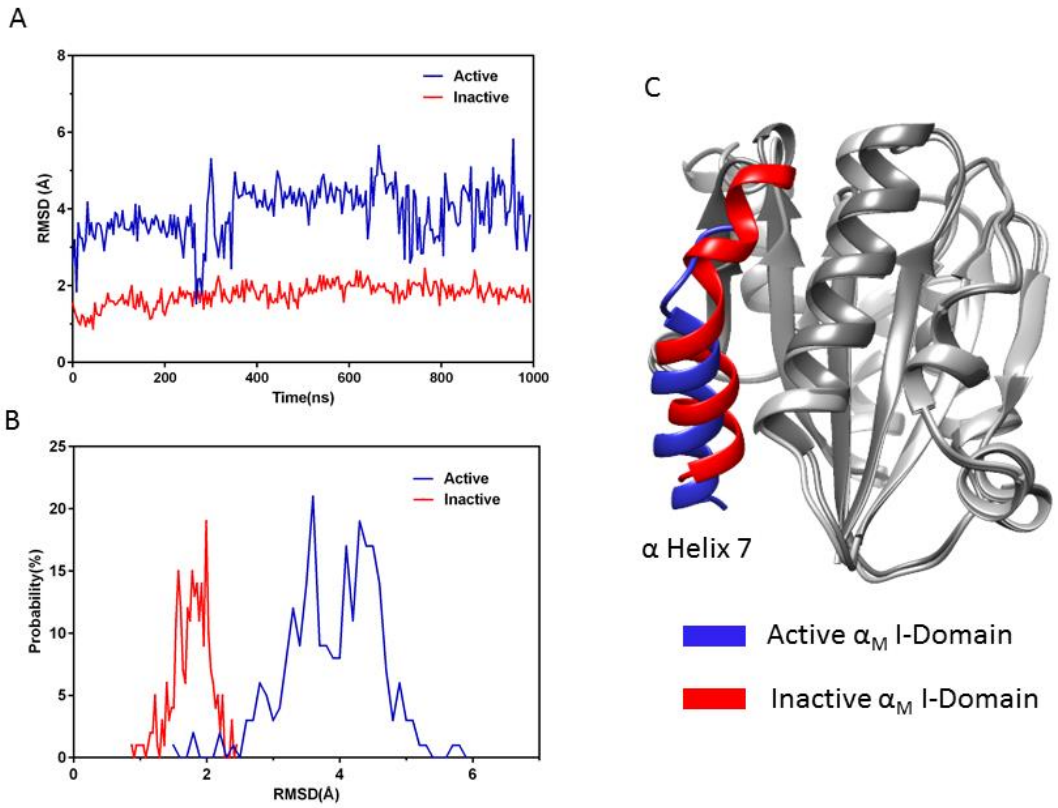

Figure 3.6 The Comparison of α7 Helix Dynamics Between Active and Inactive α_M I-domain
(A) The root-mean-square deviation (RMSD) of α7 helix Cα atoms with simulation time in active and inactive α_M I-domain (B) probability distribution of RMSD values. (C) the structure comparison between active and inactive α_M I-domain, the α7 helix is distinguished with different colors.

4, The thermostability of active and inactive α_M I-domain

We also tested the secondary structure stability of different versions of α_M I-domain with circular dichroism (CD) spectroscopy. CD spectrum can give us the information about protein folding and unfolding (139). We collected the CD spectra for active and inactive α_M I-domain shown in Figure 3.7. Both active and inactive α_M I-domain showed the classical features of an α-helical protein, with two downward peaks at 208 nm and 222 nm, in their CD spectra (139). Then, we determined the thermostability

of the two proteins by measuring the change in CD as a function of temperature. Protein can be denatured by heat. And as temperature increases, the natively folded protein loses the secondary structures which resulted in the change of the CD signal (Figure 3.7C). As Figure 3.7D showed, the active α_M I-domain manifested much lower thermostability than inactive α_M I-domain, which is reflected in lower protein melting temperature (Tm). Specifically, the data showed that the Tm of active α_M I-domain (41°C) is 14 °C lower than inactive α_M I-domain (55°C) in the absence of divalent cations.

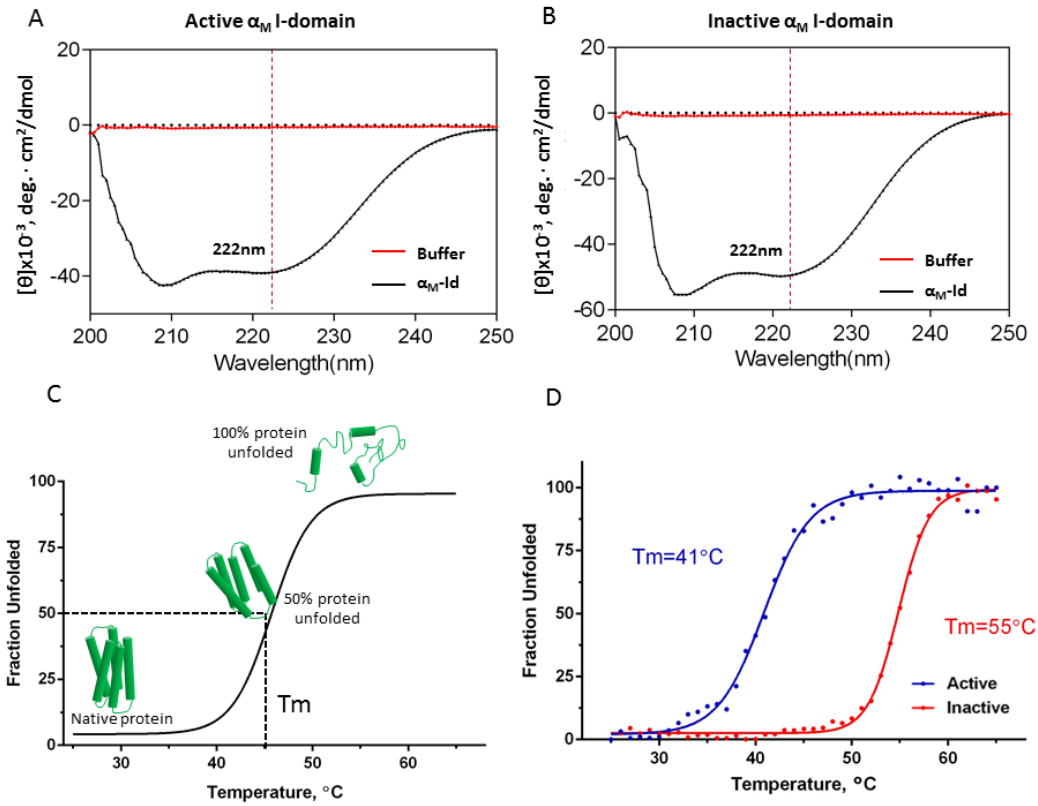

Figure 3.7 Circular dichroism (CD) Spectra and the Determination of Protein Melting Temperature (Tm) of Active and Inactive α_M I-domain
(A, B) The CD spectra of active and inactive α_M I-domain in the buffer of 20 mM HEPES, 100 mM NaCl, pH 7.0. (C) the schematic representation of Tm determination. The protein Tm is the temperature where 50% of the protein was unfolded. (D) the Tm determination of active and inactive α_M I-domain.

We also determined the effects of Mg^{2+} on α_M I-domain thermostability. The melting temperatures were measured in the same way as before. And we observed that with the increase of Mg^{2+} concentration, both active and inactive α_M I-domain melting temperatures were raised. However, the active α_M I-domain showed a higher increase of Tm than inactive α_M I-domain. As shown in Figure 3.8, adding 10 mM Mg^{2+} increased active α_M I-domain Tm by 5 °C from 41°C to 46 °C, and inactive α_M I-domain Tm was just increased by 3 °C from 55°C to 58 °C. Nevertheless, the inactive α_M I-domain is still more stable than the active α_M I-domain at 10 mM Mg^{2+} condition. This differentiation Mg^{2+} effects on α_M I-domain thermostability also motivated us to further study the Mg^{2+} effects on α_M I-domain and cationic ligand binding which will be discussed in following sections.

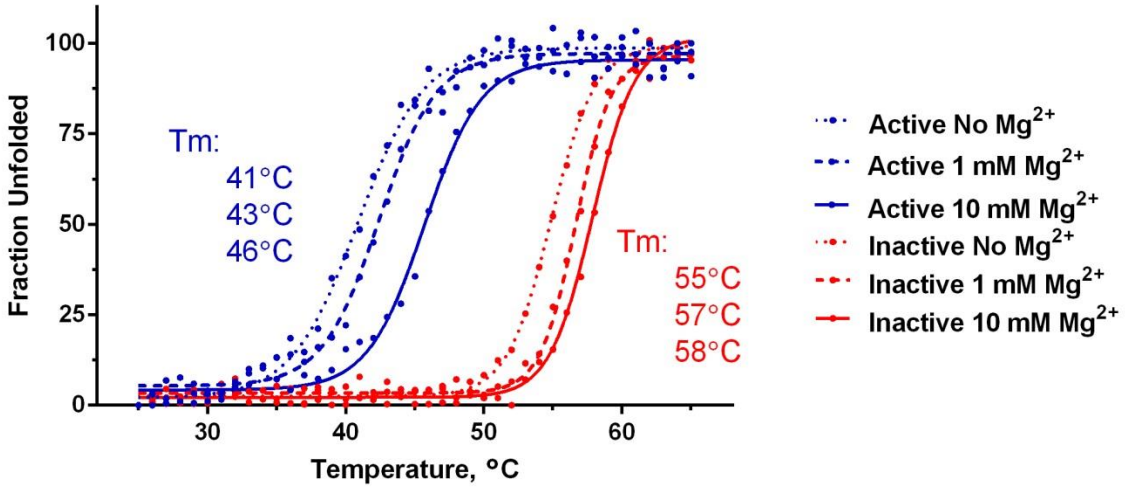

Figure 3.8 The Mg^{2+} Effect on Tm of Active and Inactive α_M I-domain
The α_M I-domain melting temperatures were measured in the different concentration of Mg^{2+}. The dot, dash and solid lines represent the conditions of 0 mM, 1mM Mg^{2+}, and 10mM Mg^{2+} respectively.

5, Metal independent binding of cationic ligands and α_M I-domain

It is widely accepted that divalent cations such as Mg^{2+}, Mn^{2+} or Ca^{2+} are essential in α I-domain and ligand interaction (95). Removal of cations could reduce ligand binding dramatically (140). The unique cationic ligand recognition specificity of α_M I-domain places this assumption in doubt and raises the question of whether divalent cations are necessary for the interaction between cationic ligands and α_M I-domain (56). To answer this question, we tested the α_M I-domain binding affinity to two cationic ligands (PTN and PF4) in the absence of any divalent cations using microscale thermophoresis (MST). And the binding tests were applied on both active and inactive α_M I-domain. From the MST trace plots (Figure 3.9A, 3.9B and Figure 3.10A, 3.10B) we saw that both PTN and PF4 induced significant thermophoresis changes when they bind to active or inactive α_M I-domain. In particular, cationic ligands significantly slowed the migration of fluorophore-labeled α_M I-domain away from the heat. By fitting the MST signal as the function of ligand concentration, we estimated the binding affinity by calculating the values of disassociation constants (Kd) (Figure 3.9C, 3.9D and Figure 3.10C, 3.10D).

From MST binding analysis, there were three interesting results observed. First, both PTN and PF4 can bind to both active and inactive α_M I-domain with the Kd range of 0.6 μM~ 64 μM in the absence of divalent cations. So, these cationic ligands were using a novel metal independent binding mechanism in contrast to the traditional metal coordinating binding mechanism. Second, both active and inactive α_M I-domain exhibited a higher binding affinity to PTN than PF4. And third, compared to inactive α_M I-domain,

active α_M I-domain showed lower binding affinity on both cationic ligands (Figure 3.9C, 3.9D and Figure 3.10C, 3.10D). For PTN binding, the Kd of inactive α_M I-domain (0.6μM) is ~7 times lower than active α_M I-domain (4.4μM). And for PF4, the binding Kd of inactive α_M I-domain (5μM) is ~13 times lower than active α_M I-domain (64μM). In addition, the active α_M I-domain probably has not been saturated by PF4 because of the low binding affinity. And because we are limited by PF4 solubility, the higher PF4 concentration could not be reached in this case. These results were unexpected, and the reason maybe because of the structural dynamics of active α_M I-domain is much higher than inactive α_M I-domain in the absence of divalent cations which caused the binding affinity to decrease. It has been shown that divalent cations can stabilize the integrin α I-domain in previous research (141). And we have also shown Mg^{2+} can stabilize active and inactive α_M I-domain thermostability to different degrees. We are curious about how does Mg^{2+} affects cationic ligand binding on the α_M I-domain, so the binding affinities in the presence of Mg^{2+} were measured by MST.

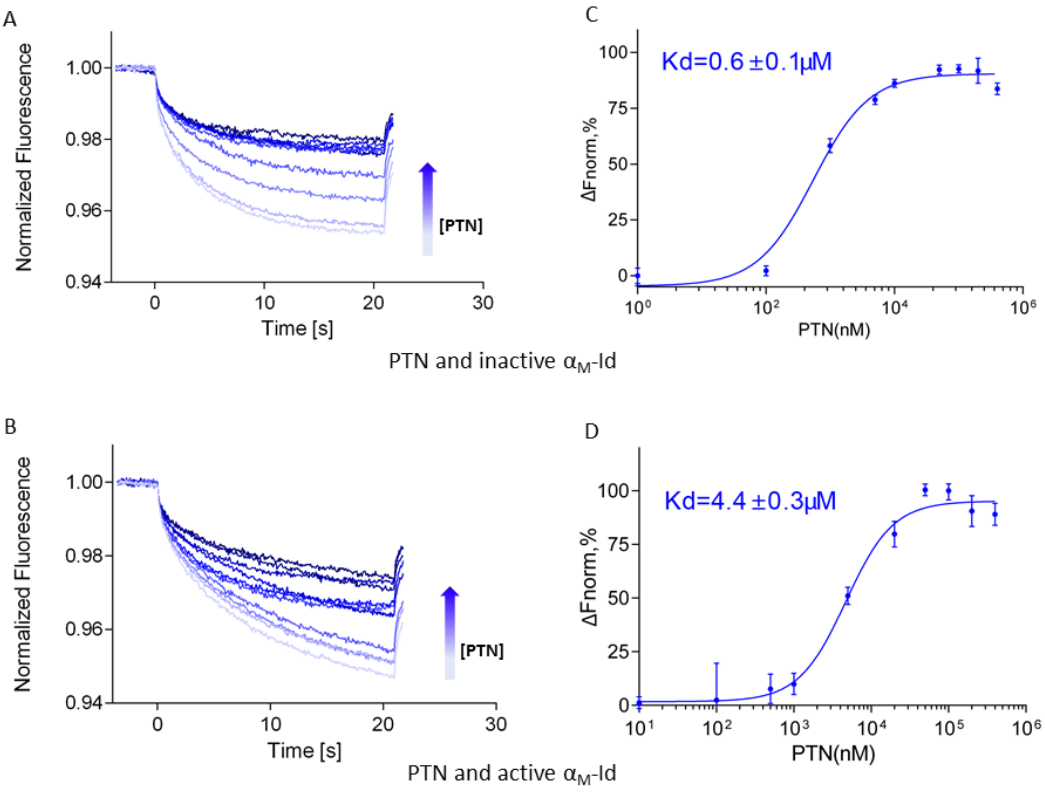

Figure 3.9 Microscale Thermophoresis of PTN with Active and Inactive α_M I-domain (A-B) The thermophoresis traces of Dylight 488 labeled inactive (A) and active (B) α_M I-domain at various concentration of PTN. The color gradient represents the increase in PTN concentration. The no PTN sample is labeled with light blue color and the most concentrated PTN samples is labeled with dark blue color. (C-D) the inactive (C) and active α_M I-domain and PTN binding curve fitted by thermophoresis signals in different concentration of PTN. The binding Kd is labeled on the left corner on binding curves.

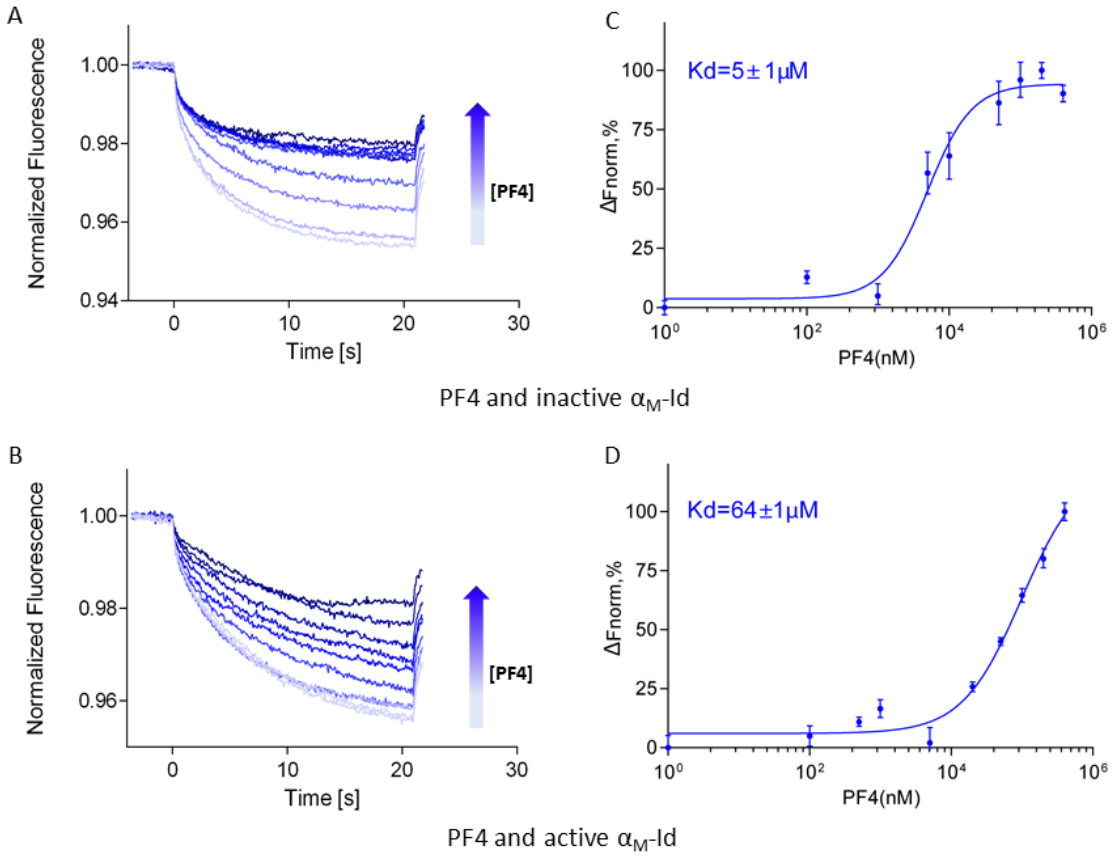

Figure 3.10 Microscale Thermophoresis of PF4 with Active and Inactive α_M I-domain
(A-B) The thermophoresis traces of Dylight 488 labeled inactive (A) and active (B) α_M I-domain at various concentration of PF4. The color gradient represents the increase of PF4 concentration. The no PF4 sample is labeled with light blue and the most concentrated PTN sample is labeled with dark blue color. (C-D) the inactive (C) and active α_M I-domain and PF4 binding curve fitted by thermophoresis signals in different concentration of PF4. The binding Kd is labeled on the left corner on binding curves.

6, Distinct ligand binding effects of Mg^{2+} on active and inactive α_M I-domain

In order to study the Mg^{2+} effect on cationic ligand binding to active and inactive α_M I-domain, a set of experiments with different Mg^{2+} concentrations were applied on both PTN and PF4 individually. From MST data, it showed that active and inactive α_M I-domain expressed different cationic ligand binding properties in the presence of Mg^{2+}.

Figure 3.11 shows the results of PTN binding. When Mg^{2+} concentration increased, the inactive α_M I-domain exhibited a slight decrease of binding affinity to PTN, whereas the active α_M I-domain showed a significant increase of binding to PTN. Compared to the control with no Mg^{2+}, adding 10 mM Mg^{2+} increased active α_M I-domain binding affinity for PTN by around 12 times (Kd decreased from 4.4 μM to 0.37 μM). And interestingly, we have observed similar outcomes when we performed the same type of experiments on PF4 (Figure 3.12). 10 mM Mg^{2+} reduced the inactive α_M I-domain's affinity for PF4 by 2.8 times but enhanced the active α_M I-domain and PF4 binding by 3.4 times (Figure 3.12).

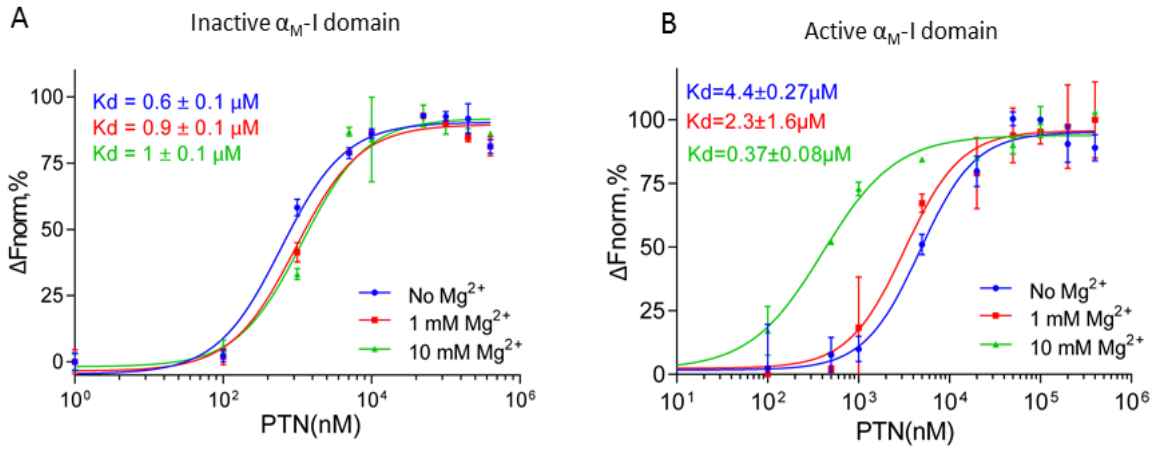

Figure 3.11 Mg^{2+} Effects of PTN Binding on Active and Inactive α_M I-domain
The difference of Mg^{2+} concentration was represented by colors, blue for no Mg^{2+}, red for 1mM Mg^{2+}, green for 10mM Mg^{2+}. (A) the binding between PTN and inactive α_M I-domain. (B) the binding between PTN and active α_M I-domain.

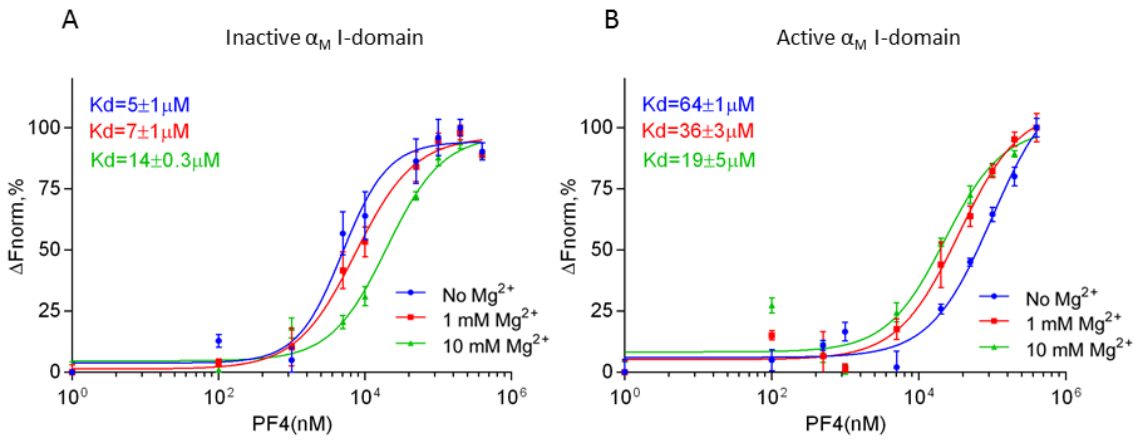

Figure 3.12 Mg^{2+} Effects of PF4 Binding on Active and Inactive α_M I-domain
The difference of Mg^{2+} concentration was represented by colors, blue for no Mg^{2+}, red for 1mM Mg^{2+}, green for 10mM Mg^{2+}. (A) the binding between PF4 and inactive α_M I-domain. (B) the binding between PF4 and active α_M I-domain.

7, Crystallization of active α_M I-domain and PTN complex

Because poor NMR spectral quality prevented us from studying the structure of the active α_M I-domain using NMR, we tried to investigate the PTN and active α_M I-domain complex structure with X-ray crystallography. We started crystallization trials with 1152 different conditions by using 6 different screening kits. And the crystals were observed in the condition of 0.1 M potassium chloride, 0.025 M magnesium chloride hexahydrate, 0.05 M Sodium cacodylate trihydrate pH 6.0, 15% v/v 2-propanol (Figure 3.13A). The crystals were harvested and sent to Advanced Photon Source (APS) at Argonne National Laboratory for data collection. The X-ray diffraction data were shown in Figure 3.13B. Although the diffraction patterns were observed at acceptable resolution (3.02Å), problems such as double lattice and fast crystal damage persisted. Optimization of the crystallization process is ongoing with the goal of collecting high-quality data to solve the PTN-active α_M I-domain complex structure in the future.

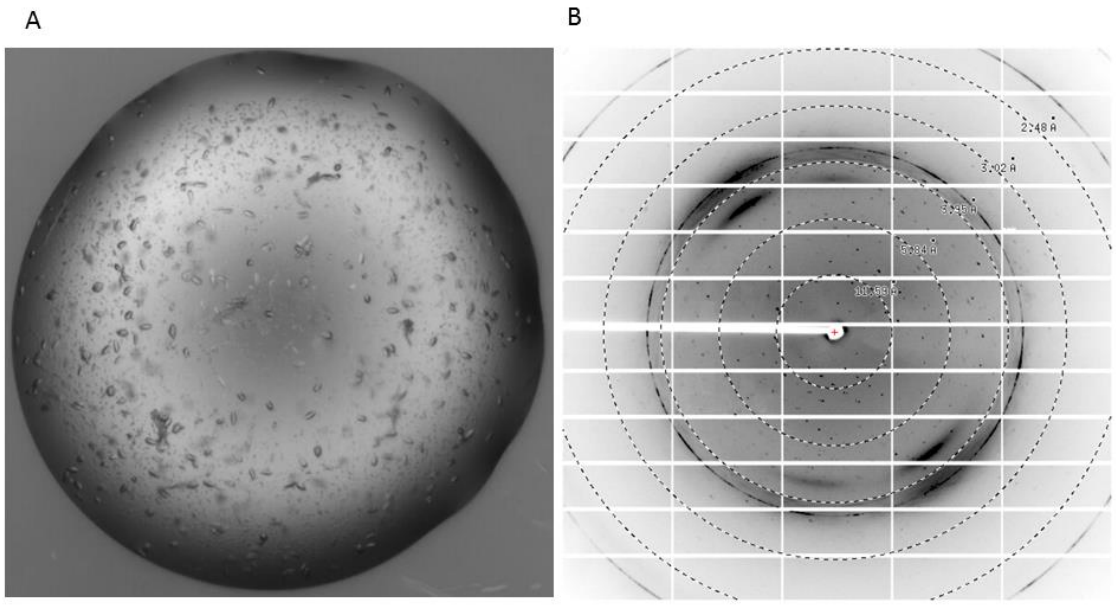

Figure 3. 13 Crystals and Diffractions of Active α_M I-domain and PTN complex (A) Active α_M I-domain and PTN complex crystals formed by sitting drop vapor diffusion. (B)X-ray diffractions of active α_M I-domain and PTN complex crystal.

3.5 Discussion

As the most promiscuous integrin, the complexity of the $\alpha_M\beta_2$ function is believed to be issued from its capability to bind a number of structurally and functionally dissimilar ligands. So far, more than 40 different ligands have been reported to interact with $\alpha_M\beta_2$ integrin (56). But there is no conclusive explanation for its diverse ligand binding ability. α_M I-domain in the role of the ligand-binding domain on integrin $\alpha_M\beta_2$ is believed to be essential for its multi-ligand binding properties (142). Although lots of work has been done to study the α_M I-domain activation and ligand binding mechanism, the reason causing its promiscuity is still unclear. Specifically, the previous study revealed that the α_M I-domain has a distinctive basic amino acid recognition preference which is not observed in other integrins (56). The molecular mechanism of why α_M I-domain has this special ligand recognition is unknown. In this study, we tried to elucidate

the mystery of α_M I-domain functional complexity from the perspectives of dynamics, binding mechanism and the role of metal in cationic ligand binding.

The previous study showed that the C-terminal truncation can cause the α_M I-domain conformation change and activation (132). And to the best of our knowledge, here we provided the first detailed demonstration of the dynamic difference between truncated active and wild type inactive α_M I-domain using a combination of different techniques including NMR, CD, and MD simulation. Initially, we want to characterize the difference between C-terminal truncated active α_M I-domain and inactive α_M I-domain using solution NMR. Although the poor NMR spectrum quality of active α_M I-domain prevented us from doing so, it forced us to adopt a new direction in the project. From the analytical size exclusive column data, we knew both active and inactive α_M I-domain is in monomer states. Thus, we speculated that the dynamic was the reason behind the spectral quality decline in the active α_M I-domain NMR spectrum. The CD data revealed that the truncated active α_M I-domain exhibited much less global thermostability than inactive α_M I-domain. In the buffer without divalent cations, active α_M I-domain's melting temperature is 14°C lowers than inactive α_M I-domain. And during the NMR experiments, we noticed that active α_M I-domain showed poorer solubility and was easily precipitated than inactive α_M I-domain. Put all these observations together, we can reach the conclusion that active α_M I-domain is less stable and more dynamic than inactive α_M I-domain.

The MD simulation enabled us to glimpse the dynamics of the α_M I-domain in a structure-based-way. Fortunately, previous researches have already determined the

crystal structures of active and inactive α_M I-domains (58, 59, 132). Without spending too much effort, we simulated the dynamics of active and inactive conformations based on crystal structures. And as we expected, the active α_M I-domain is more dynamic than inactive α_M I-domain in MD simulation. In particular, the flexibility of α7 helix on active α_M I-domain is especially conspicuous. In inactive α_M I-domain, the α7 helix is stationary on an up position as shown in Figure 3.6C. However, the α7 helix of active α_M I-domain slides around a low position in simulations. We believed the different dynamic behavior of active α_M I-domain is the result of the disruption in the hydrophobic core closed to the α7 helix. Previous research has revealed that a conserved hydrophobic intramolecular socket (SILEN, socket for isoleucine) on C-terminus is essential to fasten α_M I-domain in the closed conformation (132). The SILEN is formed by the hydrophobic side chains of Ile135, Leu164, Ile236, and Tyr267 as shown in Figure 3.14A. In a closed conformation, the Ile316 is incorporated into SILEN and holds the α7 helix on the top position (Figure 3.14A). NMR experiments also proved that even a single residue mutation of Ile316 to Gly316 is sufficient to change the stability of the α_M I-domain (data not shown). Therefore, for the active α_M I-domain construct used here, removing the entire segment after Ile316 will definitely disturb the stability of SILEN. It has been proposed that the α7 helix movement is a crucial step for integrin activation (95). This work confirmed that the position of the α7 helix is likely to be dynamic after the disruption of the SILEN pocket.

The second part of this study is to explore the binding mechanism between cationic ligands and α_M I-domain and the role of metal in their bindings. The MST data demonstrated that α_M I-domain and cationic ligands follow a unique metal independent

binding mechanism. Although there is one previous report of cationic peptide binding to α_2 I-domain (143), this study is the first proof that α_M I-domain can bind to ligands in a completely metal independent manner. Surprisingly, inactive α_M I-domain manifested higher ligand affinity than active α_M I-domain in the absence of Mg^{2+}. We think the answer is still dynamics. Specifically, because the inactive α_M I-domain has a more stable structure, the ligand has more chance to bind it through electrostatic interaction with a stable binding site that may have a higher chance of having stable interactions with the domain. Active α_M I-domain, on the other hand, experiences a constant conformation exchange, which makes the binding domain less stable. Thus, active α_M I-domain showed lower ligand binding affinity in the absence of divalent cations.

The interesting results from active and inactive α_M I-domain make the role of Mg^{2+} unusual. With increasing Mg^{2+} concentration, the cationic ligands' binding affinity is weakened in inactive α_M I-domain yet strengthened in active α_M I-domain. Our explanation for this observation is that Mg^{2+} plays different roles in the interaction between different forms of the α_M I-domain. In active α_M I-domain, because of the high structural flexibility, the exposed negative charged patch on the α_M I-domain is experiencing conformation exchanges that likely make ligand binding more difficult. Adding the Mg^{2+} helps to stabilize the open conformation of α_M I-domain and therefore cationic ligand has more chance to bind it. However, for inactive α_M I-domain, since it already has a rigid structure, Mg^{2+} has much less effect on its stability. In this case, the positive charged Mg^{2+} acts as a competitor to hinder the cationic ligand binding. As mentioned before, when metal binds to MIDAS, the active α_M I-domain shows an open

conformation and inactive shows a closed conformation. If we compare the electrostatic potential surface of the two conformations with the divalent cation embedded in MIDAS, we recognize that the open conformation exhibited a bigger negative charge patch than the closed conformation (Figure 3.14B, 3.14C, 3.14D). These may explain why PTN has a higher binding affinity to active α_M I-domain than inactive α_M I-domain in the presence of Mg^{2+}. Specifically, with Mg^{2+} in MIDAS, active α_M I-domain exposed more negative charges than inactive α_M I-domain so that cationic ligands bound tighter to active α_M I-domain.

In conclusion, we proposed the reason for this opposite effect of Mg^{2+} is that active and inactive α_M I-domain have distinctive dynamic and thermostable properties. Because active α_M I-domain is more dynamic, adding Mg^{2+} helps to stabilize the protein in active conformation which benefits the ligand binding. However, the inactive α_M I-domain already adopts in a very rigid and stable closed conformation, the Mg^{2+} with positive charge behaves more like a competitor to cationic ligands.

The case of PF4 is more complicated. Although Mg^{2+} still a negative effect on inactive α_M I-domain's PF4 binding and a positive effect on active α_M I-domain's PF4 binding, the active α_M I-domain still shows weaker binding affinity than inactive α_M I-domain even in the condition of high concentration of Mg^{2+}. The reasonable explanation for this is still protein stability and dynamics. Because PF4 is not soluble in neutral pH, we have to use a low pH buffer in binding tests. However, based on the CD data (data do not show), we have found that active α_M I-domain is much more sensitive to the pH change than inactive α_M I-domain. Lower the pH caused the active α_M I-domain

denaturation which could potentially lower its binding affinity to PF4. However, the inactive α_M I-domain is insensitive to the pH change, so the lower pH change does not affect its ligand-binding affinity.

In the previous study, our group has identified the PTN binding site on inactive α_M I-domain which is located near MIDAS using solution NMR. However, because of the limitation in the active α_M I-domain's spectral quality, we could not assign all the peaks for the active α_M I-domain HSQC spectrum. In order to reveal the interaction of PTN and active α_M I-domain, high-resolution structural information is absolutely necessary. Thus, we have endeavored to crystallize the protein complex between active α_M I-domain and PTN. We have already made promising progress. So far, we have found the preliminary crystallization condition and these crystals diffracted to a resolution of 3.02Å. Optimistically, if we could get a bigger and better crystal, the complex structure of active α_M I-domain and PTN will be revealed in the near future.

The goal of this research is to understand the reason behind $\alpha_M\beta_2$ promiscuity. The broad function and ligand binding complexity of this integrin may be attributable to dynamics and unique ligand-binding mechanisms. Based on our observation, different forms of the α_M I-domain show the dramatic dynamic difference which affects their ligand-binding properties. And also, those cationic ligands bind to the α_M I-domain with a novel mechanism. Furthermore, the role of metal is also not the same as in the canonical mechanism. Although this study paved a good way to know the uniqueness of integrin $\alpha_M\beta_2$ promiscuity, more research needed to be conducted to fully unveil the mask of $\alpha_M\beta_2$ complexities.

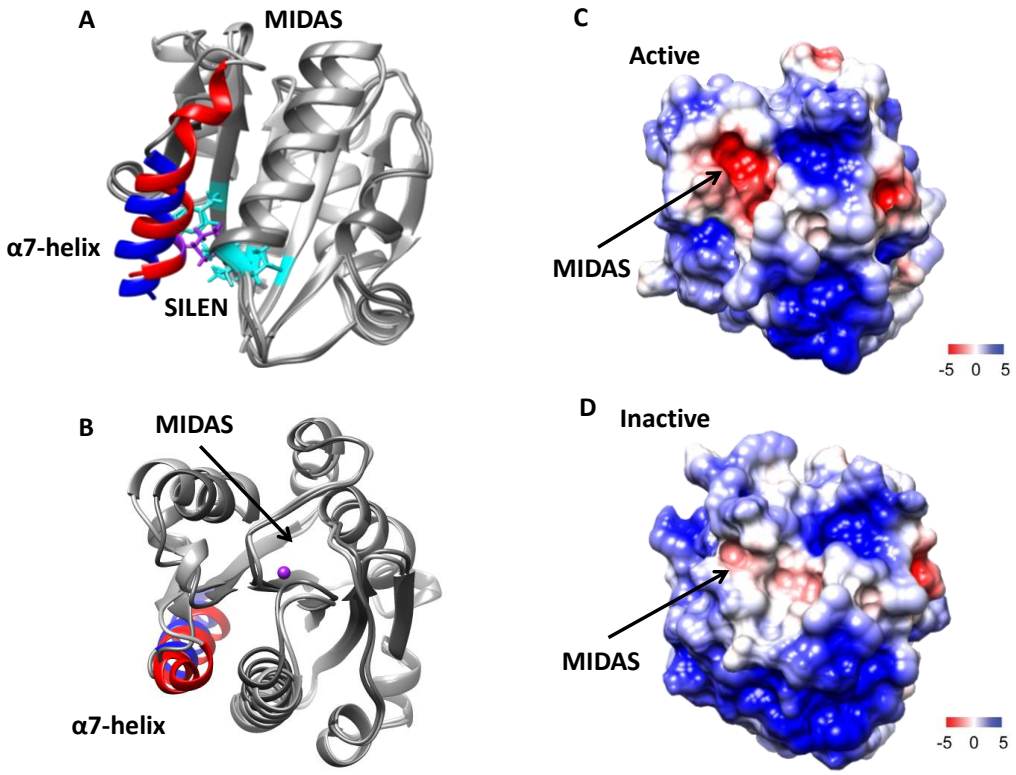

Figure 3.14 The Structures and Electrical Potential Surfaces of Active and Inactive α_M I-domain

(A)The structure comparison between active and inactive α_M I-domain. The α7 helices are highlighted with colors: red for inactive and blue for active. The hydrophobic core SILEN is labeled by cyan color, the Ile 316 residue is labeled by purple color. (B) the top view of MIDAS with Mg^{2+}, the Mg^{2+} ion is shown in purple. (C, D) the top view and electrostatic potential of active and inactive α_M I-domain MIDAS. The negative charge was labeled by red color and the positive charge was labeled by blue color. The electrostatic potential was calculated with the Mg^{2+} ion in MIDAS. The unit of potential is in kT·e-1. The active α_M I-domain shows more negative charges than the inactive α_M I-domain distinguished by more red color shown on surface.

CHAPTER 4

ELECTRON MICROSCOPY STUDIES OF FULL-LENGTH $\alpha_M\beta_2$ (MAC-1) INTERGRIN IN DETERGENT AND PHOSPHOLIPID NANODISCS

4.1 Abstract

Integrins are a family of non-covalent αβ heterodimer transmembrane proteins that regulate diverse physiological functions across the plasma membrane. Researchers have studied the relationship between conformation changes and the functional activation of integrin for many years using X-ray crystallography, nuclear magnetic resonance spectroscopy, and electron microscopy. Despite the significant advances, there is still no consensus agreement about some details of molecular mechanisms of integrin activation, especially concerning the activation of the integrin Mac-1 by cationic ligands. Although Mac-1 has been studied by electron microscopy (144), most of these data were obtained from Mac-1 ectodomain rather than the full-length integrin. Here, we endeavor to fill the gap by studying the structure of full-length intact Mac-1 in different conditions. The results show that the intact Mac-1 exhibits a very heterogeneous conformation distribution when solubilized in detergents, which may reflect the structural flexibility of Mac-1. On the other hand, we have also reconstituted intact Mac-1 into nanodiscs, a phospholipid biolayer mimic. Surprisingly, Mac-1 adopted the inactive bent conformation predominantly, which may be the result of the phospholipid biolayer supplying a more native environment for the transmembrane helices of the receptors. This Mac-1 nanodisc model provides a new platform for studying the intact Mac-1 activation mechanism in a more physiologically relevant manner.

4.2 Introduction

Integrins are a family of non-covalent αβ heterodimer transmembrane protein that regulates diverse physiological functions across the plasma membrane (145). Integrin is named for its ability to integrate signals from the extracellular and intracellular environment of the cell through inside-out and outside-in signaling. In outside-in signaling, cells receive the signal through direct ligand binding on integrin, leading to either conformation change or clustering, both of which may be necessary for integrin activation. In inside-out signaling, activated "adaptor" proteins, such as talin, bind to intracellular domains of integrins, separating the cytoplasmic domains of the subunits and subsequently changing the conformation of the ectodomain. No matter what the signaling mechanism is, the bidirectional communication is depended on the conformation change of integrin. As mentioned before, integrin consists of two subunits with single transmembrane helices, α and β. Both subunits have large multi-domain extracellular domains which are believed to be flexible to adopt different conformations. The enduring mystery is how the allosteric structure changes are related to signaling.

To understand the relationship between integrin conformation changes and its function comprehensively, much effort has been devoted to linking different integrin conformations to different activation states. Although the most detailed structures of the intact integrin ectodomains are provided by X-ray crystallography, it is also widely accepted that the flexibility of integrins means the likelihood of crystalizing integrin in its active, extended conformation is low. So far, only electron microscopy has given us glimpses into the activation mechanisms of integrins. Current evidence shows that

integrins exist in at least three overall conformational states: bent closed extended closed with adjacent αβ subunits and extended open with separate αβ subunits (Figure 4.1) (19, 95). It has been proposed that the non-covalent interaction between α and β TM/cytoplasmic domain is essential in stabilizing the inactive state of integrin (146). And this concept is confirmed by experimentally crosslinking membrane-proximal domains of α/β ectodomain with disulfide bond artificially (22, 147, 148). With the artificial clasps crosslinking on C terminus of α/β ectodomain, integrin ectodomain has been shown to exist in inactive bent conformation predominantly (22).

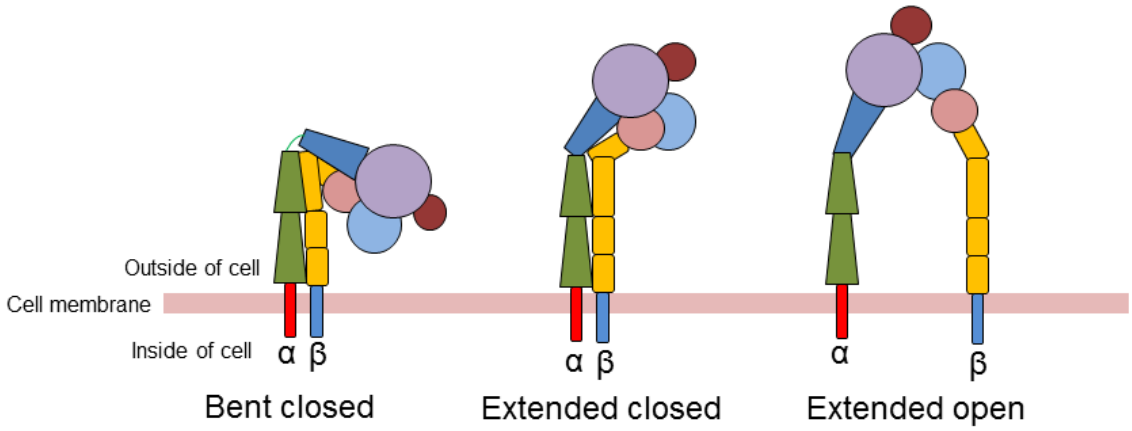

Figure 4.1 Integrin Architecture.
Three conformations of αI integrins. The bent conformation shows low ligand affinity with the closed headpiece, and extended open conformation shows the high ligand binding with open headpiece.
Adapted from Bing-Hao Luo, Christopher V. Carman. (2007). Structural Basis of Integrin. Annu. Rev. Immunol, 25:619–47.

Compared to X-ray crystallography and NMR techniques, electron microscopy (EM)'s unique advantages in studying large and heterogeneous samples manifests naturally in investigating the global structure rearrangements of integrin. EM structure data of integrin $\alpha_V\beta_3$ and $\alpha_X\beta_2$ demonstrated that both are predominantly in bent

conformation under inactive resting condition (20, 149, 150). Moreover, the activation of integrin triggers the structure rearrangement from a low-affinity state to a high affinity extended state (20). Two important key conformational changes have been revealed during the activation process. The first one is the extension at the knees of α and β subunits (147). And the other is the headpiece opening, in which the β I-domain, as well as the α I-domain if it is present, experiences a conformational change through a connecting rod-like movement of the α7-helix (95). The rearrangements of the extracellular domain and headpiece have also been confirmed by other techniques such as immunochemistry and small-angle X-ray scattering (20, 146, 151, 152). Nevertheless, many unanswered questions remain. For example, how does flexibility and dynamics of integrin relate to function, are there more intermediate states, how does the full integrin rather than ectodomain behave in a phospholipid membrane-embedded environment, and so on.

The αI containing integrin Mac-1 is the major integrin expressed in leukocytes which play a vital role in host immune responses by regulating extravasation of phagocytic cells into inflamed tissues and the phagocytosis of pathogens (153). In most cases, Mac-1 should adopt the inactive state in resting physiological conditions, which allow leukocytes to freely circulate in the blood system. However, as the most promiscuous integrin, Mac-1 demonstrates a broad ligand binding ability and wide function versatility. Furthermore, some of the evidence shows that even in the bent ectodomain conformation, Mac-1 can still bind to ligand with a small range of orientation

changes on the α I-domain (144). All these added a veil of mystery to the already mysterious activation and ligand binding mechanisms of integrin Mac-1.

Even though the first crystal structure of the integrin α I-domain was that of the α_M I-domain published in 1995 (58), attempts to crystalize the ectodomain of Mac-1 has not succeeded so far. Previous crystal structure work on an integrin homologous to Mac-1, the $\alpha_X\beta_2$ ectodomain, revealed that the connection between the ligand-binding αI domain and the propeller domains is highly flexible (154). Mac-1 is maybe more flexible than $\alpha_X\beta_2$ so that it is even harder to crystallize. Previous negative stain EM data showed that Mac-1 ectodomain can exist in both bent or extended conformation when complexed to ligands (144, 155). Recently, by using quantitative dynamic footprinting (qDF) microscopy, researchers revealed that β_2 integrins including Mac-1 on human neutrophils adopted an extended open conformation as well (156). So, there is still no conclusive verdict about the state of Mac-1 in the physiological situation. Although the qDF microscopy study probed the integrin conformations on native neutrophils using the conformation-specific antibodies, the direct structure information of intact Mac-1 in the physiological condition is still unknown. To completely understand the Mac-1 function promiscuity, more structure biology studies are still urgently needed.

Single-particle electron microscopy allows researchers to have an insight into the full-length integrin under detergent or lipid embedded environment (16). The most representative case is from a full-length $\alpha_{II}b\beta_3$ integrin EM study (16). People have studied full-length $\alpha_{II}b\beta_3$ integrin in both detergent and lipid embedded conditions. It has been reported that the β_3 integrin transmembrane domain can behave differently in

detergent micelles and phospholipid bilayers (15). So later on, to create a more accurate biological membrane mimic, the lipid nanodisc was applied in the full-length $\alpha_{IIb}\beta_3$ integrin study (157). The $\alpha_{II}b\beta_3$ integrin nanodisc study showed that ligand can activate integrin by converting it from the bent conformation to extended conformation in the absence of mechanical force or other membrane proteins (157). However, steered molecular dynamics modeling (158, 159) and other experimental studies (159-161) revealed that mechanical force can also cause integrin activation and extension. Furthermore, some studies show that the extension of unoccupied integrin requires either traction forces or collision with other membrane proteins (160). So far, it seems like the activation of full-length integrin is not only limited to one mechanism. More structural studies of lipid-embedded, full-length integrin are required to resolve the puzzles about the activation in a physiologically relevant manner.

In this chapter, we have endeavored to characterize the intact full-length Mac-1 conformations using single-particle negative stain electron microscopy. And to make the condition closer to the physiological environment, we have put effort into incorporating the full-length Mac-1 integrin into nanodiscs. 2D classification of EM images revealed that full-length Mac-1 integrin exhibits very heterogeneous conformations in detergent solution, which revealed that Mac-1 was very flexible in detergent micelles and maybe the mechanical force can change the conformation of Mac-1. However, in nanodiscs, Mac-1 adopts the bent conformation predominantly which is consistent with the concept that Mac-1 should exist in resting state in normal conditions. This Mac-1 nanodiscs

model paved the way for further study of the Mac-1 activation mechanism in physiological conditions.

4.3 Materials and Methods

1, Reagents

The mouse mAb 44a directed against the human integrin α_M subunit was purified from conditioned media of hybridoma cells obtained from the American Type Culture Collection (Manassas, VA) using protein G resin (GenScript, Piscataway, NJ. The CNBr-activated sepharose beads were purchased from GE Healthcare (Uppsala, Sweden). CD11B/integrin alpha M rabbit polyAb and CD18/integrin beta 2 rabbit polyAb antibodies were obtained from Proteintech (Rosemont, IL). The goat anti-rabbit IgG (H+L) HRP conjugate antibody was from Bio-Rad (Hercules, CA). The SuperSignal™ West Pico PLUS chemiluminescent substrate was purchased from Thermo Scientific (Rockford, IL). The n-Octyl-beta-D-thioglucopyranoside was from Biosynth Carbosynh (Itasca, IL). The lipids DMPC and DMPG were obtained from Anatrace (Maumee, OH). SM-2 Biobead was from Bio-Rad (Hercules, CA). The uranyl formate hydrate for negative stain was purchased from Electron Microscopy Sciences (Hatfield, PA).

2, Cells

Mac-1 HEK293 cells were cultured and maintained in the same condition as described in Chapter 2 and cell pellets were frozen in -80°C before the extraction of protein. The mouse mAb 44a antibody hybridoma cells were cultured in the DMEM media (Mediatech Inc., Manassas, VA) under the condition of 5% CO_2 and 37°C.

3, 44a antibody purification and 44a-CNBr column assembling

300 mL of culture media from mouse mAb 44a antibody hybridoma cells were diluted with PBS buffer in 1:1 ratio and loaded onto 1mL Protein G sepharose column with a speed of 1mL/min. The column was washed with PBS for 2 hours at 4°C and the monoclonal 44a antibody was eluted with 20mL 0.1M pH2.5 glycine buffer. The elution was immediately neutralized with 3 mL of 1 M Tris-HCl, pH7.4 neutralization buffer. The purity and activity of the antibody were confirmed by electrophoresis on SDS-PAGE gel and fluorescence-activated cell sorting (FACS) analysis on Mac-1-expressing HEK293 cells. For FACS, cells were harvested and washed with Hank's solution. Cells were then suspended to an approximate concentration of $2\text{-}2.5\times10^7$ cells/mL in Hanks buffer. And 10 μg/mL of 44a antibody was then added and incubated on ice for 30min. Then the cells were spun down and the supernatant was removed. The Alexa Fluor secondary antibody (Molecular Probe) in Hanks solution (final concentration 5 μg/mL) and then was added and incubate for 30 minutes on ice in the dark. Cells were spin down again and transfer to PBS buffer in FACS tubes. Then the cells were ready to load on the FACS machine for analysis.

The purified 44a antibody was coupled on cyanogen bromide (CNBr) activated sepharose beads based on the protocol that the manufacturer provided. In brief, 2.5g of dry resin was swelled and activated in the activation buffer (1 mM HCl). The antibody was dialyzed into coupling buffer (500 mM NaCl, 100 mM $NaHCO_3$, pH 8.3) and incubated with activated resin overnight at 4°C. The unbound antibody was washed with high pH wash buffer (500 mM NaCl, 100 mM Tris–HCl, pH 8.0) and low pH wash

buffer (500 mM NaCl, 100 mM NaOAc, pH 4.0). The unreacted CNBr site was blocked by quench buffer (100 mM Tris–HCl, pH 8.0). The coupling efficiency was calculated by dividing the total amount of antibody in the supernatant after reaction by the total amount of antibody loaded on the column. The typical coupling efficiency is more than 70%. Approximately 2mg of antibody was coupled to 1mL hydrate resin.

4, Purification of intact full integrin Mac-1

Purification of intact full integrin Mac-1 was performed as described previously (162). Briefly, Mac-1 HEK293 cells were lysed at 2×10^8 cells/mL with cell lysis buffer (100 mM Tris, pH 8.0, 150 mM NaCl, 2 mM $MgCl_2$, 1% Triton X-100 and protease inhibitor cocktail) at 4°C for 1 hour with shaking. And the lysate was centrifuged at 14,000g for 20 min at 4°C. The supernatant was loaded onto the 44a-CNBr column which was prewashed with equilibration buffer (50 mM Tris-HCl, pH 7.4, 150 mM NaCl, 2 mM $MgCl_2$, 0.1% Triton X-100) and incubated for 1 hour at 4°C. Then, the column was washed with equilibrium buffer and OG buffer (50 mM Tris-HCl, pH 7.4, 150 mM NaCl, 2 mM $MgCl_2$, 1% n-octyl β-D-glucopyranoside) sequentially. The intact integrin was eluted with elution buffer (50 mM triethylamine, pH 11.0, 150 mM NaCl, 2 mM $MgCl_2$, 1% n-octyl β-D-glucopyranoside) and was immediately neutralized with 15% by volume of neutralization buffer (1M Tris-HCl, pH 7.4). The elution was further concentrated and ran on TOSOH TSKgel G3000SW HPLC size exclusive column (30 cm × 7.5 mm, 10 μm particle size) with OG buffer at speed of 0.3 mL/min on Shimadzu HPLC system (Japan) to get rid of aggregations. The purity of the protein was checked by western blot and electrophoresis on an SDS-PAGE gel.

5, Western blot

After regular electrophoresis on SDS-PAGE, the protein was transferred to a nitrocellulose membrane by electrophoresis. The membrane was washed by TBST buffer 2 times with gentle agitation and blocked by a 5% dry milk solution for 2 hours. The primary antibodies (CD11B/integrin alpha M rabbit polyAb and CD18/integrin beta 2 rabbit polyAb antibodies) were diluted by 5% dry milk with a ratio of 1:1000 and 1:400 separately. The membrane was incubated with primary antibodies overnight at 4°C and washed by TBST buffer 5 times before developed in the chemiluminescent substrate.

6, Expression and purification of a recombinant membrane scaffold protein (MSP1D1)

The pMSP1D1 plasmid was kindly provided by Dr. Wade Van Horn. The expression of MSP1D1 was performed in *Escherichia coli* BL21 (DE3) cells in LB media. 1mM IPTG was added to induce the protein expression when cells grew to OD600 =1.3~1.4. After induction, the cell culture was shaken at room temperature overnight before harvesting. The cell pellets were centrifuged and harvested with lysis buffer. The cells were lysed by sonication and the lysate was centrifuged at 16,000g for 30 min at 4°C. The supernatant containing soluble MSP1D1 was collected and loaded on 5mL of Ni-NTA resin. The column was pre-equilibrated by 4 column volumes (CV) of Wash 1 buffer (40 mM Tris-HCl (pH 8), 300 mM NaCl, 1% Triton X-100). The supernatant was incubated with Ni-NTA resin at 4°C for 45 min with rotation. The resin was packed into the chromatography column and the flow-through was collected. Then, the resin was washed with 4 CV of Wash 1 buffer until OD_{280} does not go down during this wash. The resin was further washed by 4 CV of Wash 2 buffer (40 mM Tris-HCl, 300 mM NaCl, 50

mM cholate, pH 8.0), 4 CV of Wash 3 buffer (40 mM Tris-HCl, 300 mM NaCl, pH 8) and 4 CV of Wash 4 buffer (40 mM Tris-HCl, 300 mM NaCl, 50 mM imidazole, pH8.0) sequentially. Finally, the MSP1D1 protein was eluted by elution buffer (40 mM Tris-HCl, 300 mM NaCl, 300 mM imidazole, pH8.0). The fraction with elution peaks of MSP1D1 protein was combined and buffer exchanged to TEV reaction buffer (20 mM Tris-HCl, pH7.5, 100 mM NaCl, 1 mM EDTA, and 1mM DTT). The protein was digested by TEV protease by the ratio of 20:1(TEV: MSP1D1) at room temperature overnight. The digested MSP1D1 was collected from the flow-through in the further running on the Ni column. Lastly, the protein was purified by Superdex 75 size exclusion chromatography columns with a flow rate of 1mL/min. The MSP1D1 protein was then buffer exchanged to sodium bicarbonate buffer and lyophilized. The protein concentration was determined by BCA assay and the purity was confirmed by electrophoresis.

7, Integrin Mac-1 nanodiscs preparation

The Integrin Mac-1 nanodiscs were prepared by a modified protocol from the previous study on integrin $\alpha_{IIb}\beta_3$ (163). The synthetic lipids: 1,2-dimyristoyl-sn-glycerol-3-phosphocholine (DMPC), 1,2-dimyristoyl-sn-glycerol-3-phosphate-(1'-rac-glycerol) (DMPG) were solubilized in chloroform (DMPC) or chloroform/methanol mixture (2:1 volume ratio) at a concentration of 10 mg/mL and mixed into a glass tube by 1:1 ratio. The lipids were dried in a glass tube with a steady flow of nitrogen air for 30 min and lyophilized to remove the residue solvent. MSP1D1 dried powder was solubilized in deionized water at a concentration of 200μM. The lipids were dissolved in lipid resuspension buffer (10 mM Tris, 100mM NaCl, pH 7.4, 100 mM cholate) by vortex until

the lipids are fully solubilized, giving a lipid concentration of 50 mM. The lipids, MSP1D1, and integrin Mac-1 were mixed with the ratio of 90:1:0.002 and incubated at room temperature for 1 hour. 1mL of SM-2 Biobead was prewashed with methanol (3 times), water (7 times) and TBS (twice) before use. And 1mL of SM-2 Biobead was added to protein lipids mixture to remove the detergent overnight at room temperature with gentle agitation. The supernatant containing integrin nanodiscs were separated using a Superdex 200 increase size exclusion columns at a flow rate of 0.3mL/min on AKTA FPLC to get rid of aggregations with OG buffer. The integrin nanodiscs and empty nanodiscs were then separated and identified by running SDS-PAGE electrophoresis.

8, Preparation of negative stain EM grids and data collection

A negative stain solution was prepared by 0.75% uranyl formate and deionized water. 37.5 mg of uranyl formate was dissolved in 5mL boiling water with stirring in the dark. 5~10µl of 5M NaOH was added until the solution becomes slightly dark yellow and the solution was stirred for another 5min. The stain solution was filtered with a 0.2µm syringe filter to remove the precipitation into the falcon tube wrapped in aluminum foil. For making a negative stain EM grid, the protein was first diluted to proper concentration (~0.3µg/mL) and immediately absorbed to glow-discharged carbon-coated copper grids for 60 seconds. For the intact Mac-1 sample within OG buffer, the grids were washed with 40µl drops of deionized water, and for nanodisc samples, only two washes were required. 2 drops of 0.75% uranyl formate stain were applied on samples right after washes. The negative satin samples were first checked by a Philips CM12 transmission electron microscope (TEM). Then the data was collected on FEI Tecnai F20 TEM

operated at 200 kV and images were recorded at a magnification of 80000× with TVIPS XF416 CCD camera using Serial EM software.

9, Data processing and 2D classification

The micrographs were recorded as many stacks of 100 images in mrcs files. The stacks of mrc files were separated using IMAGIC EM2EM software and further processed in RELION for manual particle picking and 2D class average. 15 Å of low pass filter was applied and the pixel size was defined as 2.2 Å and 2.7 Å for intact Mac-1 and nanodisc Mac-1 classification. The particles were first classified into 200 classes with reference-free classification in RELION and further classified to 20~50 classes using sub-selected particles.

4.4 Results

1, 44a antibody and CNBr- 44a antibody column

To purify intact Mac-1 from the mammalian cell culture, a Mac-1 affinity column was prepared using a 44a monoclonal antibody and CNBr-activated sepharose. 44a antibody can specifically bind to the integrin α_M I-domain with a strong affinity (27). We cultured and collected the hybridoma culture supernatant after they have reached 80% cell confluency, and the cell was maintained by splitting and addition of fresh medium every 2 to 3 days. Because this antibody is an immunoglobulin G (IgG) antibody, we used protein G to purify the 44a antibody from the collected culture supernatant. As shown in Figure 4.2, the purified 44a antibody was loaded and separated by electrophoresis on 7.5 and 12 % SDS-PAGE gel in the reduced and non-reduced conditions respectively to check the purity. IgG antibodies have a molecular weight of

approximately 150 kDa, composed of two kinds of polypeptide chains linked by disulfide bonds. One of approximately 50 kDa, termed the heavy or H chain, and the other, of 25 kDa, termed the light or L chain shown in Figure 4.2C. Figure 4.2A shows two bands from heavy and light chains separately in reduced condition and Figure 4.2B presents the single band from the unreduced antibody. According to the SDS-PAGE gel, the protein G column purified antibody is pure.

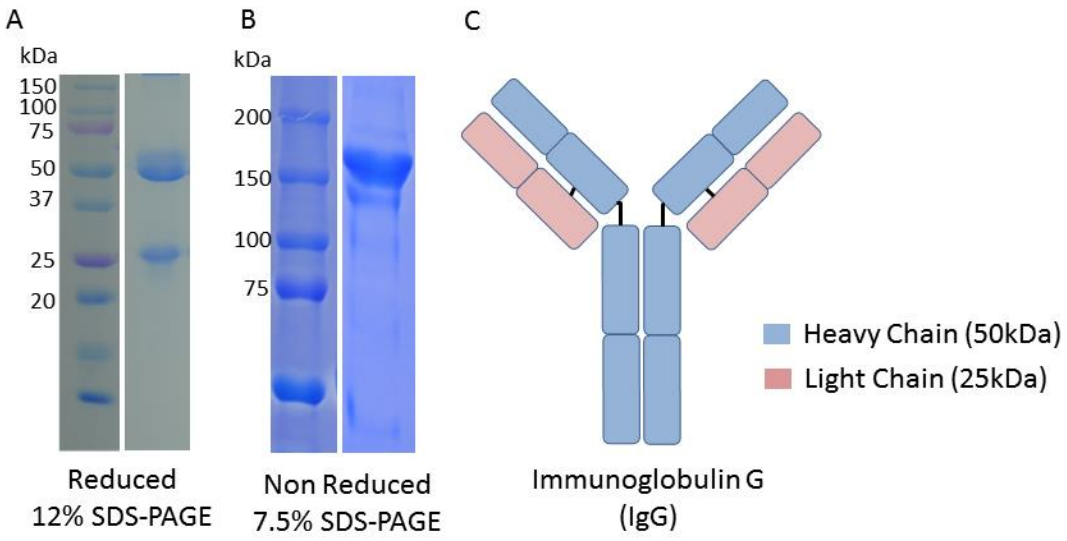

Figure 4.2 SDS-PAGE of 44a IgG Immunoglobulin
(A) 44a antibody electrophoresis on 12% SDS-PAGE, protein disulfide bonds were reduced by dithiothreitol before loading. (B) 44a antibody electrophoresis on 7.5% SDS-PAGE without reduction. (B) schematic representation of immunoglobulin G.

The integrin-binding activity of purified 44a antibody was tested using fluorescence-activated cell sorting (FACS) on Mac-1-HEK293 cells. In FACS, forward versus side scatter (FSC vs SSC) density plot is commonly used to identify the cells of interest. Cells with different sizes and granularity will show on the different positions at FSC vs SSC density plot. Typically, the forward scatter relates to the cell size and side

scatter relates granularity. By using a gating strategy, we can count only Mac-1-HEK293 cells for analysis and exclude the debris which is usually shown at the bottom left corner at the plot with lower FSC and SSC Figure 4.3A-C.

The stably transfected Mac-1 HEK293 cells were incubated with the purified 44a antibody and sorted by FACS. The 44a antibody was used as a primary antibody to probe the cells who expressed Mac-1 on their surface. Comparing to the negative control with secondary antibody only, the purified 44a antibody shows obvious binding as shown in Figure 4.3D. We have also tested the commercially available 44a antibody as a positive control with the same cell line and it showed a similar result as our purified 44a antibody. This confirmed that our purified 44a antibody has a good binding affinity to Mac-1 and ready to be used for Mac-1 purification.

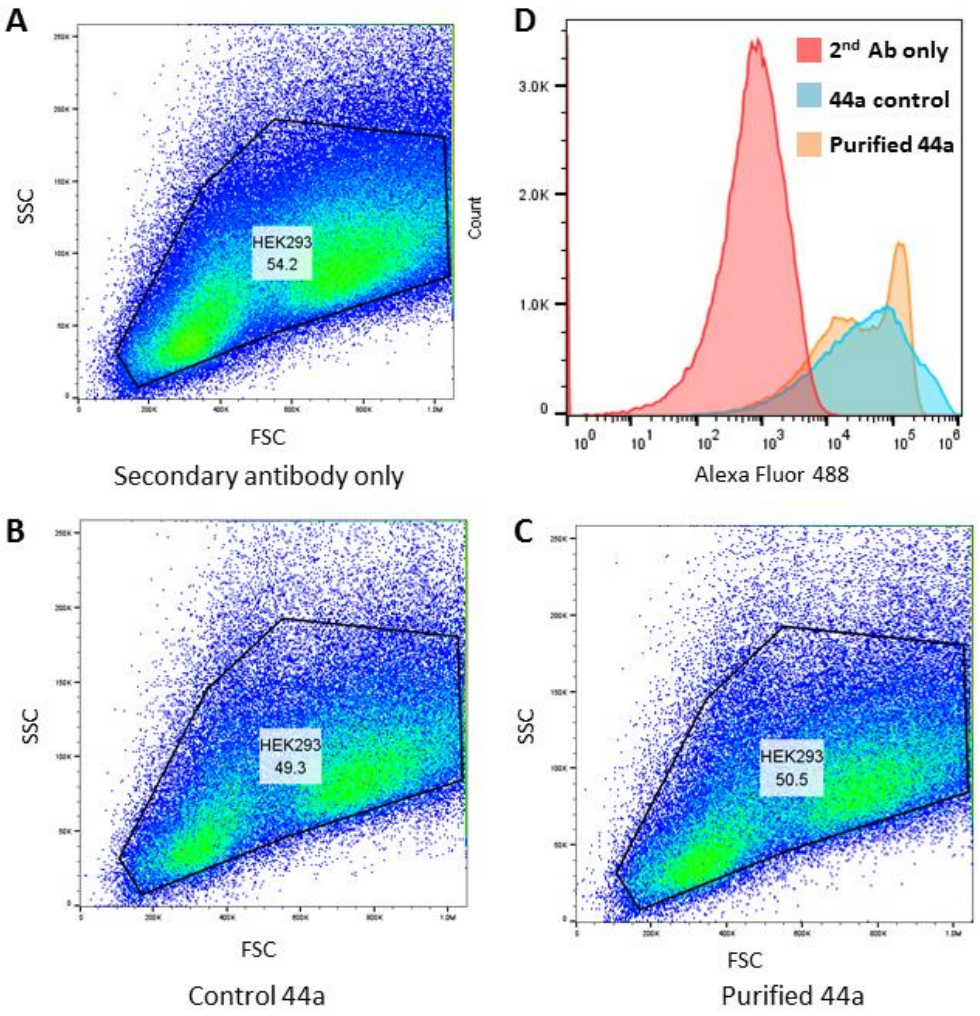

Figure 4.3 FACS of Mac-1 HEK293 with 44a Primary Antibody and Alexa Fluor 488 Secondary Antibody.
(A-C) FSC vs SSC density plots in different tests. Each dot on the plot represents an individual particle that passed through the laser. A gate has been applied to identify Mac-1 HEK293 cells shown as black wedges in the figure. (D) Single parameter histograms overlaid of negative control (pink) and positive control (blue). Purified 44a and commercial 44a show a similar stained cell population which proves the Mac-1 binding efficiency of our purified 44a antibody.

To purify full-length Mac-1 from Mac-1 HEK293 cells, 44a antibodies crosslinked cyanogen bromide (CNBr) sepharose resin was packed and used as a Mac-1 affinity column. For making this column, we directly coupled 44a antibody to the CNBr-active

resin by coupling amine groups on the antibody to cyanate ester group on the resin. The reaction was rapid and spontaneous(164). By measuring the concentrations of the remaining antibodies after the reaction, we estimated the coupling efficiency. In this case, 99% of the 44a antibody was cross-linked on to the resin.

2, Full-length Mac-1 integrin purification

Stably transfected Mac-1 HEK293 cells were cultured in common mammalian cell culture conditions (DMEM medium under 5% CO2 and 37°C), collected and split when cell confluency reach to 80%. We collected a total of 125mL of cell cultures for each trial of Mac-1 purification. The lysed cells were first passed through the 44a antibody column to capture Mac-1, which is eluted with a high pH elution buffer. The elution was then further purified by size exclusion column to get rid of protein aggregation and degradations. Because the protein concentration is too low to be detected by regular coomassie brilliant blue-stained SDS-PAGE, we have to use western blot to detect the fractions containing the target protein. Figure 4.4A and C showed the western blot results of different fractions from 44a column elution with anti-α_M antibody and the chromatogram from the second size exclusion column. As Figure 4.4B showed, we have also confirmed the purity of final Mac-1 integrin by electrophoresis and western blots.

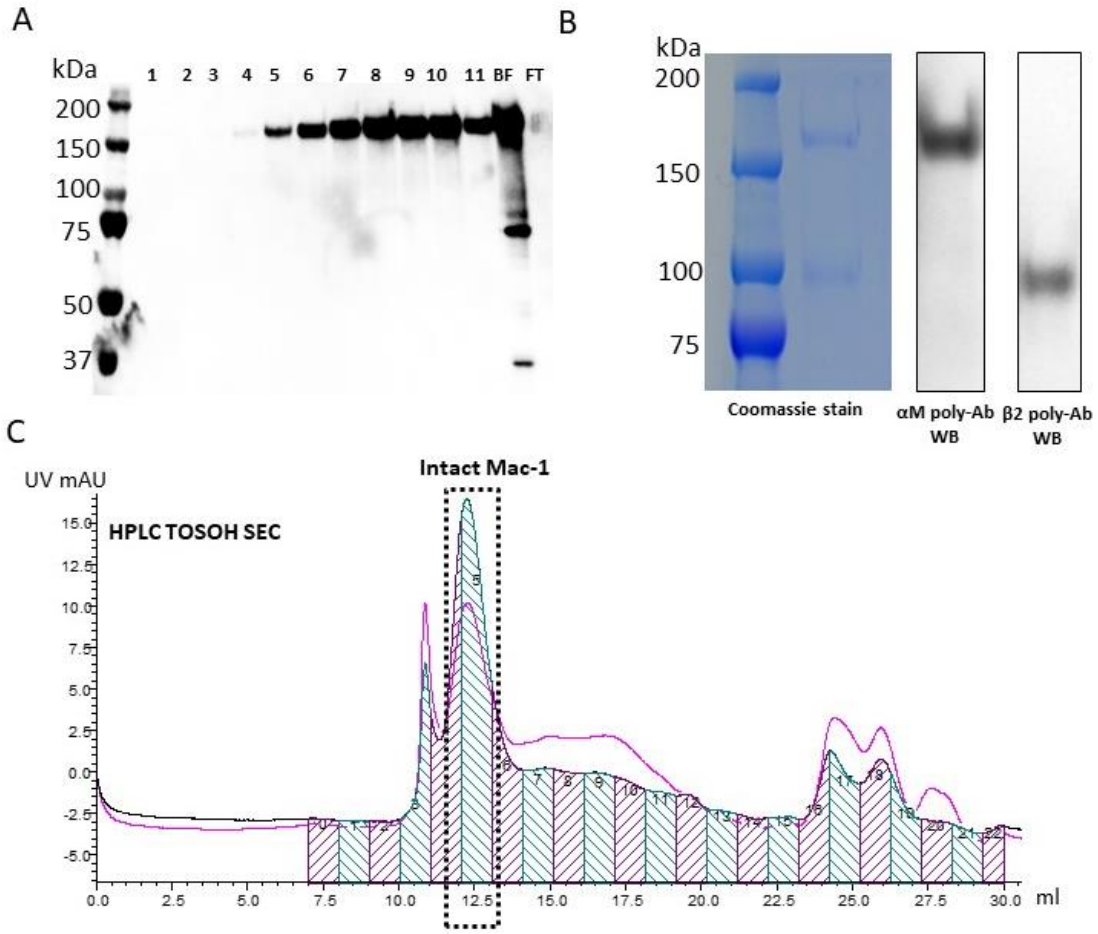

Figure 4.4 Purification of Intact Mac-1 Integrin
(A) Western blot with anti-α_M primary antibody for elution fractions from the 44a antibody column. Target protein Mac-1 was eluted from fraction number 4. The last two lanes showed the proteins before loading on column (BF) and flow through after elution (FT). (B) electrophoresis on 7.5% SDS-PGE showed the final purified Mac-1, the two bands on gel represented α_M and β_2 subunits proved by western blot (WB). (C) chromatography of Mac-1 from TOSOH HPLC size exclusion column. The monomer Mac-1 was eluted at 12.5 mL (dashed box) in fraction number 5. The UV 280nm was colored by purple and UV 230nm was colored by black.

3, Full-length Mac-1 integrin 2D classification

Negative stain EM analysis of the fractions showed that Mac-1 monomers were eluted at fraction number 5 at around 12 mL on the TOSOH size exclusive column. After the elution of Mac-1, we immediately coated intact Mac-1 protein on the copper grid and

stained it with uranyl formate for negative EM. The inactive Mac-1 integrin ectodomain is believed to adopt the bent conformation in the resting state, as has been observed in crystal structures of $\alpha_V\beta_3$ and $\alpha_X\beta_2$ ectodomains (154, 160, 165). However, the conformation states of intact full-length integrin are not very clear. Some results from $\alpha_{IIb}\beta_3$ integrin show that it adopts the bent conformation only in the absence of a phospholipid membrane (166). But there is also evidences that $\alpha_{IIb}\beta_3$ exists in a continuous conformational equilibrium clustered around four different states including bent, extended close and extended open conformations when embedded in the lipid nanodiscs (167). Here we sorted individual conformations of Mac-1 using unbiased, iterative, reference-free 2D class averaging as implemented in the software RELION (168). A total of 24116 particles from 1000 micrographs were used for analysis. The initial 200 classes were sub-selected and classified into 20 final classes. We identified three main conformational groups of intact Mac-1 when embedded in detergents (Figure 4.5). These confirmations include (A) a compact nodule which is similar to the bent conformation shown in $\alpha_X\beta_2$ crystal structure (154), (B) an intermediate conformation that has closed α and β subunits with different degrees of extension and (C) an extended open conformation with two clearly separated α and β subunits. We have analyzed the population of the three different conformers and showed that 54% particles can be assigned to bent conformation, 20% were assigned as extend closed conformation and 25% were in extend open conformation.

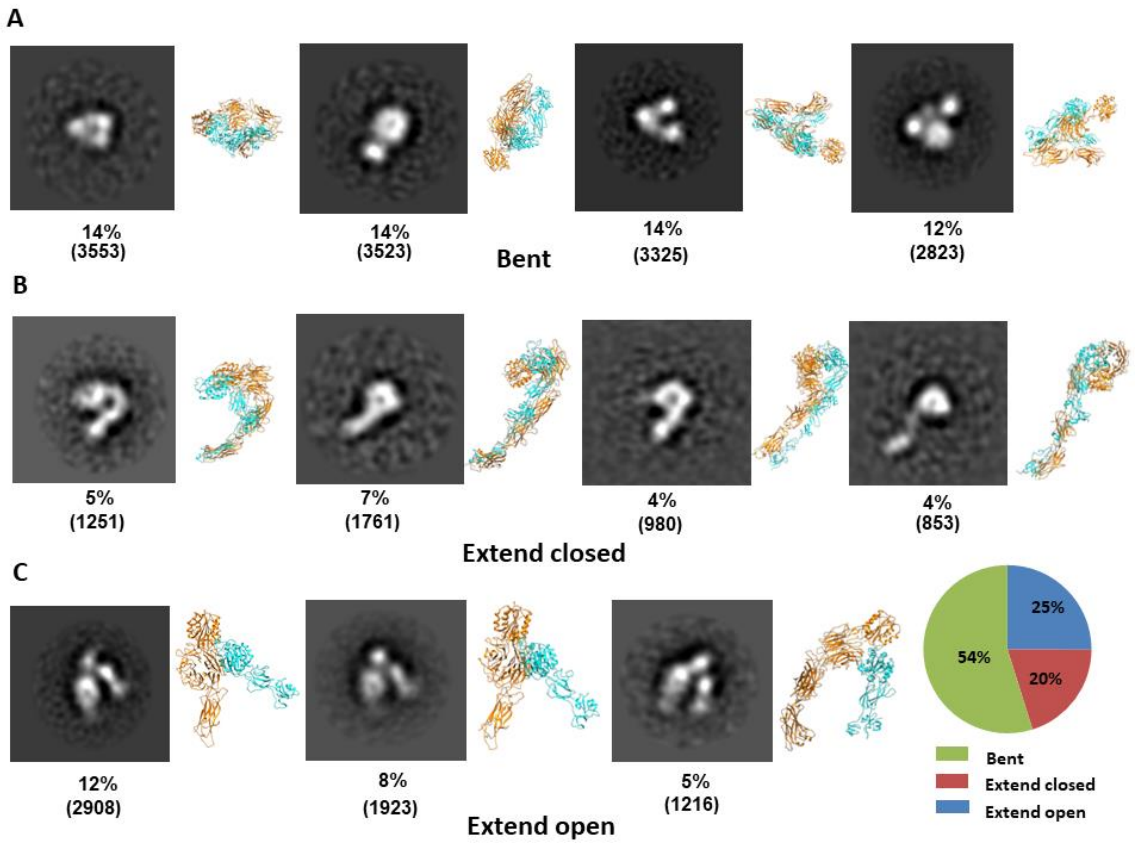

Figure 4.5 Class Averages of Intact Mac-1
These class averages come from a total of 24116 particles, the numbers under the images represent the percentage and the total numbers of particles in each class. (A-C) are the representatives of ns-EM class averages of bent, extend closed and extend open conformations. The pie chart shows the percentages of each conformation.

4, Preparation of MSP1D1 nanodiscs

Phospholipid nanodiscs are great tools developed in the last ten years to study membrane proteins in a considerably more native membrane environment (169). They are assembled from phospholipids and a class of amphipathic helical proteins derived from human apolipoprotein A-1 termed membrane scaffold proteins (MSP) (170). In this study, we used a deletion construct of MSP1 (MSP1D1) which forms nanodiscs of approximately 10nm in diameter (170). We have expressed and purified recombinant

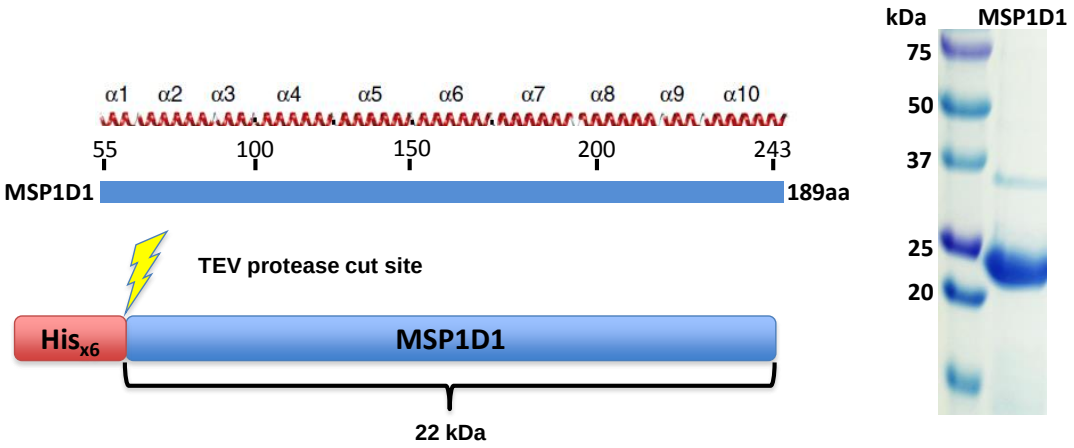

Figure 4.6 The MSP1D1 Construct and Its Purification
Adapted from Franz Hagn, Manuel Etzkorn, Thomas Raschle, and Gerhard Wagner (2013). Optimized Phospholipid Bilayer Nanodiscs Facilitate High-Resolution Structure Determination of Membrane Proteins. J Am Chem Soc. 135(5) 1919–1925.

MSP1D1 in *E.coli* cells. The final purified MSP1D1 protein without His-tag has a molecular weight of 22kDa (Figure 4.6).

The nanodiscs are formed by a self-assembly procedure initiated by gradual removal of detergents using Bio-Beads, a nonpolar polystyrene adsorbent. Here we have tested the removal efficiency of n-octyl β-D-glucopyranoside (OG), the detergent in integrin buffer, using 1D ^{1}H NMR (Figure 4.7). As the figure shows the ^{1}H signal of OG had decreased to a very low level after just 1-hour of incubation with Bio-Beads.

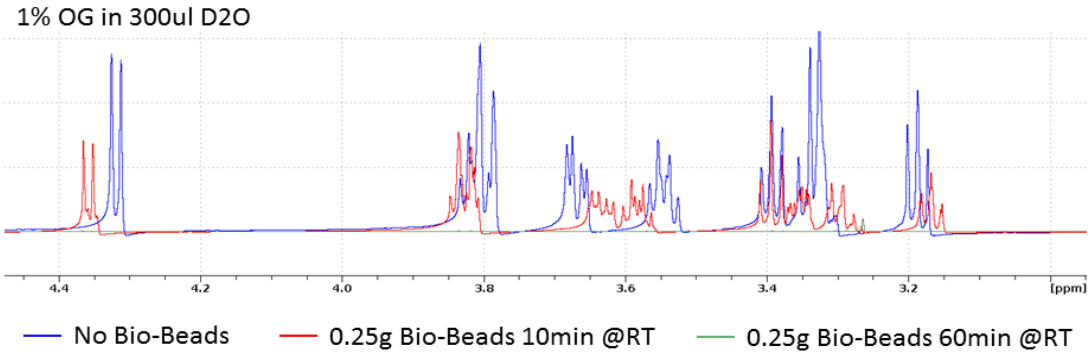

Figure 4.7 1D ^{1}H NMR Spectra of OG in the Presence of Bio-Beads.
The blue line represents the ^{1}H signal of 1% OG D2O buffer without Bio-Beads. The red line and green line represent the OG spectra after incubation with Bio-Beads for 10min and 60min at room temperature.

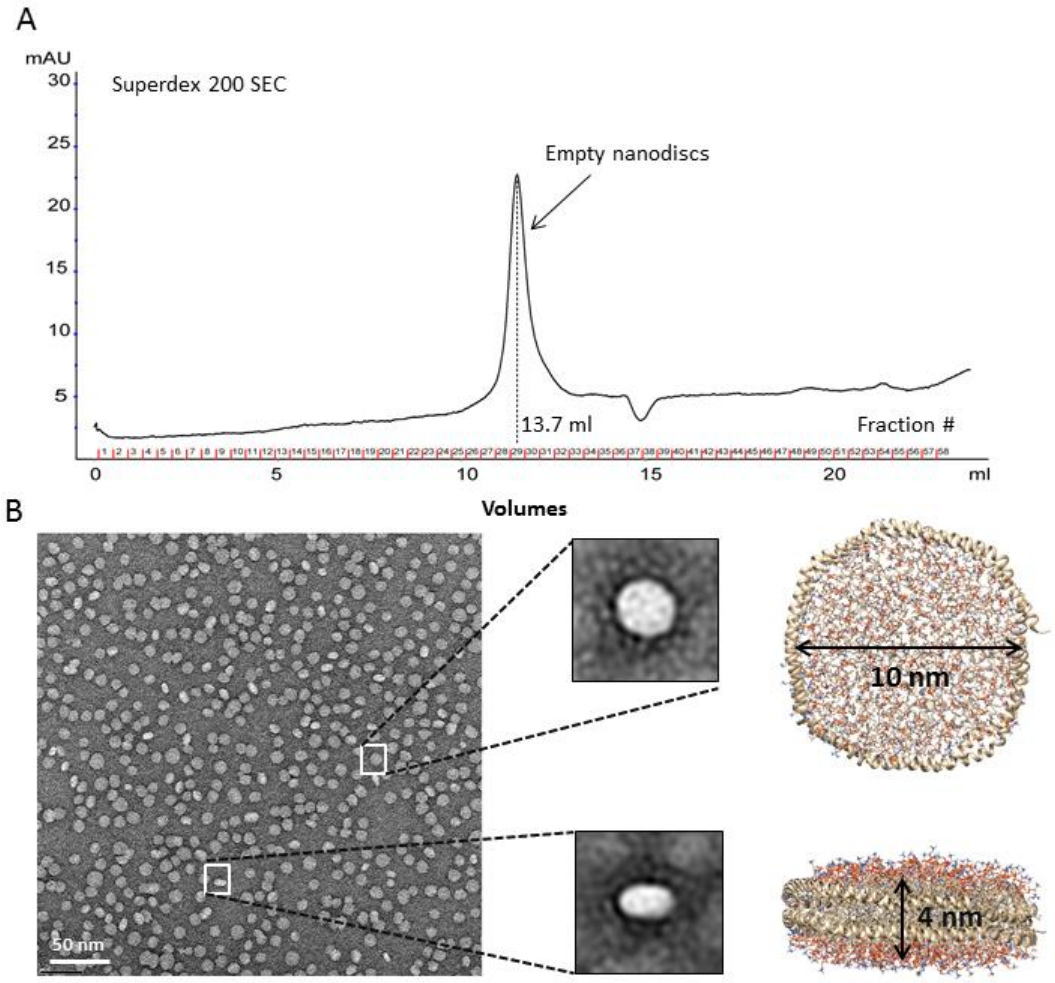

Figure 4.8 Characterization of Empty Self-assembly MSP1D1 Nanodiscs
(A) Size-exclusion chromatograms of DMPG/DMPC nanodiscs formed with MSP1D1 on superdex 200 column. (B) the ns-EM raw image and representative of 2D class average of the top and side view of empty nanodisc. The model of nanodisc was built from PDB: 6CLZ

Our self-assembly nanodiscs were analyzed on a Superdex 200 size exclusion column, using UV absorption for detection as shown in Figure 4.8A. The chromatography shows a single peak of empty nanodiscs eluted from 13.7mL which is consistent with a previous study (169). The homogeneity of nanodiscs was checked by negative stain EM shown in Figure 4.8B. The results confirmed that nanodiscs of the appropriate size have been made using our current protocol

5, Preparation of Mac-1 integrin nanodiscs

Many membrane proteins including integrins have been reported to be capable of being incorporated into nanodiscs, a more physiological condition, for structural studies (157, 171-173). In previous research, people have successfully incorporated full-length $\alpha_{IIb}\beta_3$, an αI domain less integrin, into the MSP1D1 nanodisc. And they revealed the full-length $\alpha_{IIb}\beta_3$ conformation changes through the talin activated inside-out signaling in nanodisc with negative stain EM (157). Here we were trying to imitate the same procedure and incorporate Mac-1 integrin into MSP1D1 nanodiscs. We reconstructed the Mac-1 integrin nanodiscs using modified protocols from the previous study (163) and purified them on the Superdex 200 increase size exclusive column. The chromatography shows the separation of integrin nanodiscs and empty nanodiscs (Figure 4.9A). The fractions which contain the integrin nanodiscs were analyzed by negative stain EM (ns-EM). In the ns-EM micrographs, we observed a round density for empty nanodiscs, and in the integrin nanodiscs, we observed an additional density of a protrusion which represented incorporated integrin (Figure 4.9). By measuring the distance from the top of the protrusion to the edge of nanodisc, we can estimate the conformation state of each integrin in nanodiscs. In bent conformation, the distance from the top of the integrin to edge of the nanodisc is around 10 nm, while as in extended conformation that distance should be more than 20 nm. We did the 2D class average using the same method as mentioned before for full length Mac-1 (Figure 4.9). And 577 Mac-1 nanodisc particles from 180 micrographs has been screened, the results showed that more than 90% (539

out of 577) of Mac-1 adopted the bent conformation which is greatly different with the results from Mac-1 in detergents.

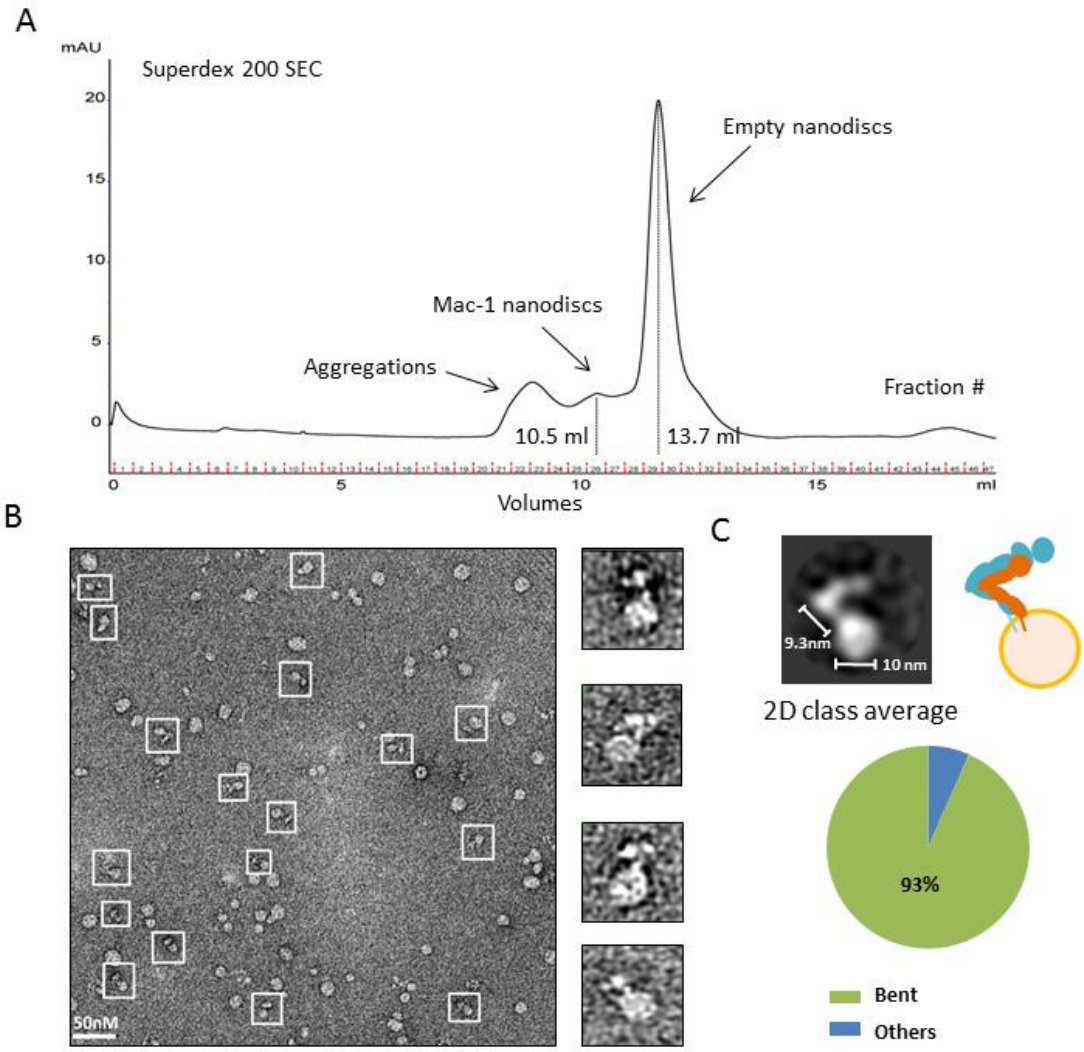

Figure 4.9 Characterization of Integrin Mac-1 Nanodiscs
(A) Superdex 200 size exclusion chromatogram of Mac-1. The fractions that contain the integrin Mac-1 nanodiscs and empty nanodiscs are shown. The Mac-1 nanodiscs were eluted from 10.5 mL separated from aggregations and empty nanodiscs which eluted at 13.7 mL. (B) the raw ns-EM micrograph of Mac-1 nanodiscs mixed with empty nanodisc. 4 selected representative particles are listed beside the micrograph. (C) the 2D class average of Mac-1 nanodiscs. The model besides the image represents the bent Mac-1 in nanodisc, the α sub-unit is drawn in cyan color and β sub-unit is in orange color. The pie chart shows the percentages of bent conformation from all selected particles.

4.5 Discussion

Integrin activation is central to various cell functions such as cell migration, immune response, extracellular matrix assembly and hemostasis (145). Previously, numerous studies have shown that integrin activation is correlated with its conformation changes (60, 152, 174-176). And a lot of understanding of how conformation change is communicated to other parts of integrin is based on the structure data from recombinantly expressed ectodomain or headpiece of integrin (20, 160, 177-179). Although these massive structures reveal that ectodomain can experience a conformation transition from bent to extended, which is accepted as an essential part of the integrin activation mechanism, there are still not many studies on intact integrin. Especially, there is no report on intact αI integrins to our best knowledge.

Here we used HEK293 cell to express intact Mac-1 integrin and purified it with a home-made antibody column. As visualized by negative stain EM, we found that the intact Mac-1 exhibited an exceptional conformational heterogeneity in detergent which is very different from the ns-EM study of intact $\alpha_{IIb}\beta_3$ (180). Specifically, researchers found detergent-solubilized $\alpha_{IIb}\beta_3$ predominantly (~90%) adopted a compact bent conformation until extended by activation with ligand binding (180). But in our case, the detergent-solubilized intact Mac-1 was displayed in three different conformations: 54% bent, 21% extend close and 25% extend open. There are several potential explanations for this difference between intact $\alpha_{IIb}\beta_3$ and Mac-1. First, Mac-1 contains an αI domain in the α subunit, whereas $\alpha_{IIb}\beta_3$ does not. This structure difference could possibly make Mac-1 more flexible than $\alpha_{IIb}\beta_3$. In addition, Mac-1 is more promiscuous ligand recognition

ability and high function versatility may require conformation heterogeneity to allow it to adapt to different ligands and situations. Second, it has been found that different detergents and micelles can affect the structure of the transmembrane segment of integrin (15). In the $\alpha_{IIb}\beta_3$ study, the protein was solubilized and kept in Triton X-100, yet we kept protein in n-octyl β-D-glucopyranoside (OG) solution in the final product. The benefit of OG is that it forms smaller micelles that are easier to remove, but the drawback is less protection on the transmembrane part of the protein. This difference in detergent can be another reason that causes Mac-1 changes conformation during the purification process. Lastly, the previous intact $\alpha_{IIb}\beta_3$ was purified from human platelets, a more natural resource which preserved the resting state of integrin. In our case, although we have tried to purify the native intact Mac-1 from human neutrophils, we are limited by the protein yield. So, we have to use HEK293 to overexpress the Mac-1 for this study. We do not know if this different expression system could cause the protein to behave differently. In this case, additional experiments need to be applied to determine the reason why Mac-1 shows higher heterogeneity in detergents. But there is a strong sign that Mac-1 may be more flexible than $\alpha_{IIb}\beta_3$ as a result of functional adaptation.

There is always a concern that negative stain EM will introduce conformation bias of protein because the sample preparation process involves heavy metal stain, absorbing on carbon film, and dehydration (157). To address this, people have studied the intact $\alpha_{IIb}\beta_3$ in a hydrated environment with cryo-EM recently. Surprisingly, their results show that $\alpha_{IIb}\beta_3$ exists in a conformational equilibrium clustered around four main states in a lipid embedded environment rather than just bent inactive conformation (167, 181).

Although these results contradict $\alpha_{IIb}\beta_3$ negative stain EM data, in some way it supports our observations of integrin Mac-1 which also shows a distribution of different conformations. In our study, Mac-1 exists in bent, extended closed and extended open conformation. Furthermore, in the class of extended closed conformation, we observed different extents of leg extension, which may represent an equilibrium process (Figure.4.5B). To confirm our hypothesis, the cryo-EM study of intact Mac-1 is probably the most direct way in the future.

Since detergent may cause the artefactual conformation change of intact Mac-1, we decided to put integrin into nanodiscs which are supposed to be closer to physiological lipid condition on the cell surface. Surprisingly, we found more than 90% of Mac-1 was in bent conformation in nanodiscs. This result is remarkably different from what we observed from detergent-solubilized Mac-1. It is possible that nanodisc phospholipid bilayers stabilize proteins better than detergent micelles so that most of the integrins are preserved in an intact inactive state. If this is true, this Mac-1 nanodisc model provides an excellent system that enables people to study an intact Mac-1 integrin activation mechanism by testing ligand-induced conformation change. But as mentioned before, this homogeneity of Mac-1 conformation could also be simply the result of a negative stain sample preparation artifact. So, there is the need to use cryo-EM to prove the authenticity of this observation.

In conclusion, these studies paved the way for future study on intact Mac-1 integrin which is a critical step in our understanding of the activation of Mac-1 in physiological conditions. By studying the conformation heterogeneity in the under

different conditions, we may find the crucial activation factor needed to change conformation which will finally lead us to understand the ligand promiscuity and functional diversity of Mac-1 integrin.

CHAPTER 5

CONCLUSION AND OUTLOOK

This thesis is focused on understanding the complicated functions of leukocyte integrin $\alpha_M\beta_2$ from the perspective of structural biology. As the major adhesion receptor on leukocytes, integrin $\alpha_M\beta_2$ is essential to numerous immune processes, including extravasation, phagocytosis, immune synapses formation and others (91, 182). Among all the integrins, $\alpha_M\beta_2$ stands out from the crowd in regard to its high ligand-binding promiscuity and function diversity (56). In Chapter 2, we discovered and explored the binding mechanism of a new $\alpha_M\beta_2$ cationic ligand: pleiotrophin (PTN). Chapter 3 investigated the role of dynamics in α_M I-domain and cationic ligand interactions. And chapter 4 discussed structure studies of full-length integrin $\alpha_M\beta_2$.

5.1 Pleiotrophin induced leukocyte integrin $\alpha_M\beta_2$ functions

Pleiotrophin (PTN) is a multi-functional, cationic, glycosaminoglycan-binding cytokine involved in numerous physiological and pathological processes such as cell growth, neural regeneration, tumor growth, angiogenesis, and inflammation (183, 184). This study is mainly focused on PTN's function in the immune response. Previous researches have shown that PTN can trigger tissue inflammation and regulate microglia-mediated neural inflammation (75, 185). However, the PTN receptor has not been identified. In this context, integrin as the important function receptor on immune cells attracted our attention. Before our research, one report showed that integrin $\alpha_v\beta_3$ is a PTN receptor regulating cell migration in angiogenesis (86). However, this PTN-induced integrin $\alpha_v\beta_3$ function was investigated on the endothelial cells rather than immune cells.

Although integrin $\alpha_v\beta_3$ is also expressed on immune cells, we did not find PTN induced cell behavior changes on $\alpha_v\beta_3$-transfected CHO cell through function assays (data not shown). Coincidentally, we found that PTN has a strong binding affinity to integrin $\alpha_M\beta_2$. After a series of rigorous cell-based function assays, we proved that PTN can trigger cell adhesion, spreading, migration through integrin $\alpha_M\beta_2$ both on HEK293 model cells and mice neutrophils. Moreover, by using different biophysical techniques, we demonstrated the binding between PTN and α_M I-domain at the molecular level and identified the $\alpha_M\beta_2$ binding epitope on PTN.

Nevertheless, this is just a small step towards understanding PTN induced integrin $\alpha_M\beta_2$ activation. In the future, a lot more experiments need to be conducted to fully understand how PTN induce leukocyte activation through integrin $\alpha_M\beta_2$. For example, to know what the signal pathway is during this activation, the genetic analysis during the signaling may need to be carried out. To understand how PTN recruit leukocytes and induce integrin $\alpha_M\beta_2$ outside-in signaling during the immune reaction, more cell biology experiments are needed. Furthermore, we do not know if other proteins work together with PTN and integrin such as receptor protein tyrosine phosphatase ζ, which has been shown to bind with PTN and integrin $\alpha_v\beta_3$ (86). In a word, many unknowns are waiting to be explored by researchers who have expertise from different fields. From the perspective of structure biology, we are interested in how cationic ligand like PTN binds to integrin $\alpha_M\beta_2$ and induce the structure changes. This is the reason we conducted research in chapter 3 and chapter 4.

5.2 The role of α_M I-domain structural dynamics in its interactions with cationic ligands

It is commonly accepted that integrin function is depended on its conformation rearrangement (5, 95). And α I-domain, when present, plays a crucial role in integrin activation through ligand binding and the subsequent induced conformation change. In this research, we demonstrated that active α_M I-domain showed much higher dynamics than inactive α_M I-domain. Secondly, we showed this dynamic plays an important role in cationic ligands binding. Moreover, we revealed the different roles of divalent cation Mg^{2+} in interactions between cationic ligands and different versions of the α_M I-domain. In a nutshell, two important discoveries were made in this study. First, we found a novel metal-ion independent binding mechanism between α_M I-domain and cationic ligands. This novel mechanism, to some extent, explains why the α_M I-domain has this broad ligand recognition ability and basic amino acid recognition preference. Second, we confirmed the role of dynamics in α_M I-domain and cationic ligand interactions. Although the cationic ligand-α_M I-domain binding does not require divalent cation, the Mg^{2+} may act as a structure stabilizer to exert a positive effect on the active α_M I-domain ligand binding. However, for the rigid inactive α_M I-domain, Mg^{2+} becomes a competitor to cationic ligands. This interesting observation diversified the role of divalent cations in the α_M I-domain function.

Integrin $\alpha_M\beta_2$ is a unique member among the integrin family for its ligand promiscuity and special basic amino acid recognition preference. The current investigation has begun to offer an explanation to the cause of integrin $\alpha_M\beta_2$ complexity

from the view of the structure dynamic and functional diversity of the α_M I-domain. Whether this dynamic feature and metal independent ligand-binding mechanism exist only in integrin α_M I-domain needs more exploration and confirmation. This study is by no means the first report of interactions between cationic ligands and integrins. The first report of such interactions showed that integrin α_2 I-domain can also bind to cationic ligands, yet in a metal ion-dependent manner (143). On the other hand, people also have shown that α_2 I-domain is able to bind echovirus 1 in the ion-independent manner (183, 186). Interestingly, we recently identified that the integrin α_2 I-domain is able to bind PF4 in a metal independent way similar to the α_M I-domain (Figure 5.1). The binding domain is also on a negative patch around the MIDAS site on α_2 I-domain shown in Figure 5.1B. From NMR and CD data, we noticed the α_2 I-domain structure is even more stable than inactive α_M I-domain. In this case, Mg^{2+} acts as an inhibitor for PF4 binding. These findings support our previous hypothesis. So maybe this metal ion-independent ligand-binding mechanism also exists in other integrins. However, more cell-based function assays are required to prove that PF4 is biologically relevant to α_2 integrin function in the future.

5.3 The characterization of full-length integrin $\alpha_M\beta_2$

For a more comprehensive understanding of cationic ligand-induced integrin $\alpha_M\beta_2$ activation, we also attempted to study the structure of full-length $\alpha_M\beta_2$ using negative stain EM. The present results manifested the complexity of integrin $\alpha_M\beta_2$. The conformation heterogeneity of integrin $\alpha_M\beta_2$ in detergent produced many questions. Is this heterogeneity caused by the detergent and mechanical force, or is this native to

integrin $\alpha_M\beta_2$? To answer the question, we need to carry out more rigorous experiments in the future.

The nanodisc integrin data showed that more than 90% of full-length $\alpha_M\beta_2$ adopted the bent conformation which is really different from what we observed from data in detergents. This implies that the environment surrounding protein may be the cause of the conformation heterogeneity. The nanodisc provided a more physiologically relevant environment for full-length $\alpha_M\beta_2$ so that most of it adopts a native inactive bent conformation. The ultimate goal of studying full-length $\alpha_M\beta_2$ includes two aspects. First, we want to know whether cationic ligand binding induces the $\alpha_M\beta_2$ integrin conformation change. Second, we look forward to solving the high-resolution structure of full-length $\alpha_M\beta_2$ integrin. To achieve these goals, higher quality proteins are required, the data of conformation distribution change induced by ligand are needed, and the cyro-EM study on full-length $\alpha_M\beta_2$ integrin is necessary.

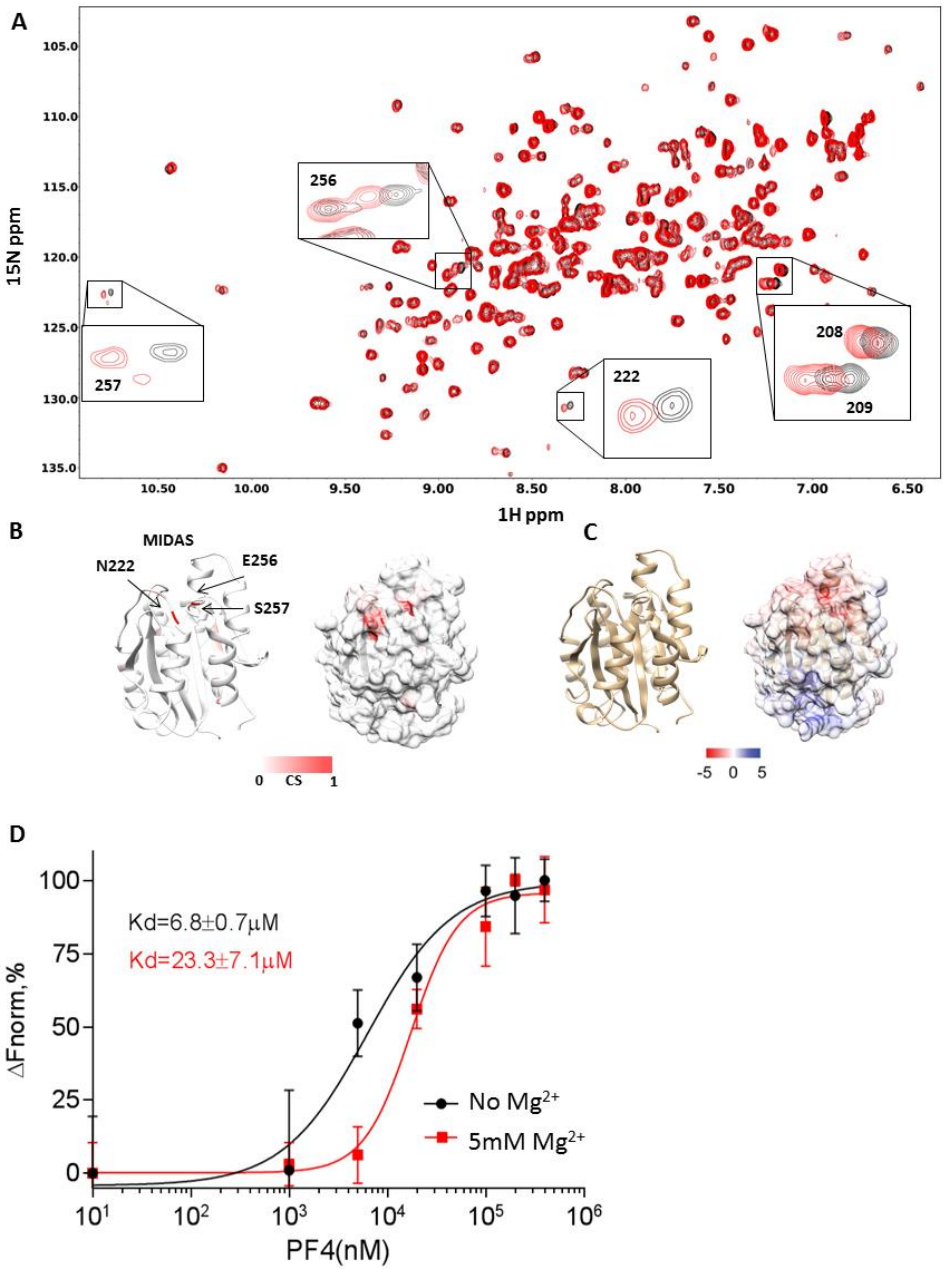

Figure 5.1 The Interaction Between PF4 and α_2 I-domain
(A) ^{1}H-^{15}N HSQC of integrin α_2 I-domain. The black peaks represent the α_2 I-domain without PF4, the red peaks represent α_2 I-domain in the presence of 6 molar equivalents PF4. Some representative peak shifts are magnified as shown in boxes. (B) The chemical shift mapping of PF4 perturbed residues. The most perturbed residues are color coded as 1 in red and the non-perturbed residues are labeled by white color as 0. (C) the structure and electrostatic potential surface of α_2 I-domain. The unit of potential is in kT·e-1. (D)The binding curve of PF4 and α_2 I-domain. Mg^{2+} as a competitor reduced the PF4 binding affinity.

REFERENCES

1. JW, T., DeSimone DW, Fonda D, Patel RS, Buck C, Horwitz AF, Hynes RO. (1986) Structure of integrin, a glycoprotein involved in the transmembrane linkage between fibronectin and actin. *Cell.*46(2):271-82.

2. Bing-Hao Luo, C.V.C. (2007) Structural Basis of Integrin. *Annu. Rev. Immunol.*25:619–47

3. Bouvard D, P.J., De Franceschi N, Ivaska J. (2013) Integrins are ubiquitously expressed transmembrane. *Nat Rev Mol Cell Biol.*14(7):430-42

4. Takada Y, Y.X., Simon S. (2007) The integrins. *Genome Biol.*8(5):215.

5. Humphries, I.D.C.a.M.J. (2011) Integrin Structure, Activation, and Interactions. *Cold Spring Harb Perspect Biol.*3(3): a004994.

6. Campbell, I.D. and M.J. Humphries. (2011) Integrin structure, activation, and interactions. *Cold Spring Harb Perspect Biol.* 3

7. Arnaout, M.A., S.L. Goodman, and J.P. Xiong. (2007) Structure and mechanics of integrin-based cell adhesion. *Curr Opin Cell Biol.* 19,495-507

8. Askari, J.A., et al. (2009) Linking integrin conformation to function. *J Cell Sci.* 122,165-70

9. Bennett, J.S., B.W. Berger, and P.C. Billings. (2009) The structure and function of platelet integrins. *J Thromb Haemost.* 7 Suppl 1,200-5

10. Xiong JP, S.T., Diefenbach B, Zhang R, Dunker R, Scott. (2001) Crystal structure of the extracellular segment of integrin. *Science.*294: 339–345.

11. Larson RS, C.A., Berman L, Springer T. (1989) Primary structure of the leukocyte function-associated molecule-1 a subunit: An integrin with an embedded domaindefining a protein superfamily. *J Cell Biol.*108: 703–712.

12. Liddington RC, G.M. (2002) Integrin activation takes shape. *J Cell Biol.*158:833–839

13. Xiao T, T.J., Coller BS, Wang JH, Springer TA. (2004) Structural basis for allostery in integrins and binding to fibrinogen-mimetic therapeutics. *Nature.*432: 59–67.

14. Lau TL, D.V., Ulmer TS. (2008a) Structure of the integrin aIIb transmembrane segment. *J Biol Chem.*283:16162–16168.

15. Lau TL, P.A., Ginsberg MH, Ulmer TS. (2008b) Structure of the integrin b3 transmembrane segment in phospholipid bicelles and detergent micelles. *Biochemistry.*47: 4008–4016.

16. Adair BD, Y.M. (2002) Three-dimensional model of the human platelet integrin alpha IIbbeta 3 based on electron cryomicroscopy and x-ray crystallography. *Proc Natl Acad Sci USA.*99:14059–14064

17. Vinogradova, O., et al. (2000) A structural basis for integrin activation by the cytoplasmic tail of the alpha(IIb)-subunit. *Proceedings of the National Academy of Sciences of the United States of America.* 97,1450-1455

18. Lee JO, R.P., Arnaout MA, Liddington R. (1995) Crystal structure of the A domain from the. *Cell.*80:631–638

19. Dustin, T.A.S.a.M.L. (2012) Integrin inside-out signaling and the immunological synapse. *Current Opinion in Cell Biology.*24:107–115

20. Takagi, J., et al. (2002) Global conformational rearrangements in integrin extracellular domains in outside-in and inside-out signaling. *Cell.* 110,599-11

21. Vinogradova, O., et al. (2002) A structural mechanism of integrin alpha(IIb)beta(3) "inside-out" activation as regulated by its cytoplasmic face. *Cell.* 110,587-97

22. Takagi, J., H.P. Erickson, and T.A. Springer. (2001) C-terminal opening mimics 'inside-out' activation of integrin alpha5beta1. *Nat Struct Biol.* 8,412-6

23. Yanbo Zhang, H.W. (2012) Integrin signalling and function in immune cells. *Immunology.*,135(4):268-75.

24. Harris ES, W.A., Zimmerman GA. (2013) Lessons from rare maladies: leukocyte adhesion deficiency syndromes. *Curr Opin Hematol.*20(1):16.

25. Nath, S.K., et al. (2008) A nonsynonymous functional variant in integrin-alpha(M) (encoded by ITGAM) is associated with systemic lupus erythematosus. *Nat Genet.* 40,152-4

26. Al-Herz W, B.A., Casanova JL, Chapel H, Conley ME, Cunningham-Rundles C, Etzioni A, Fischer A, Franco JL, Geha RS, Hammarström L, Nonoyama S, Notarangelo LD, Ochs HD, Puck JM, Roifman CM, Seger R, Tang ML. (2011) Primary immunodeficiency diseases: an update on the classification from the international union of immunological societies expert committee for primary immunodeficiency. *Front Immunol.* 8;2:54

27. Bunting M, H.E., McIntyre TM, Prescott SM, Zimmerman GA. (2002) Leukocyte adhesion deficiency syndromes: adhesion and tethering defects involving beta 2 integrins and selectin ligands. *Curr Opin Hematol.* .9(1):30-5.

28. Kuijpers TW, v.d.V.E., Weterman MA, de Boer M, Tool AT, van den Berg TK, Moser M, Jakobs ME, Seeger K, Sanal O, Unal S, Cetin M, Roos D, Verhoeven AJ, Baas F. (2009) LAD-1/variant syndrome is caused by mutations in FERMT3. *Blood.*113(19):4740-6.

29. Hom G, G.R., Modrek B, Taylor KE, Ortmann W, et al. (2008) Association of systemic lupus erythematosus with C8orf13-BLK and ITGAM-ITGAX. *N Engl J Med.*358: 900-909.

30. International Consortium for Systemic Lupus Erythematosus, G., et al. (2008) Genome-wide association scan in women with systemic lupus erythematosus identifies susceptibility variants in ITGAM, PXK, KIAA1542 and other loci. *Nat Genet.* 40,204-10

31. Nath SK, H.S., Kim-Howard X, Kelly JA, Viswanathan P, Gilkeson GS,. (2008) A nonsynonymous functional variant in integrin-αM (encoded by. *Nat Genet.*40(2):152–4

32. MacPherson M, L.H., Morrison and Fagerholm. (2013) Leukocyte Beta2-Integrins; Genes and Disease. *Genet Syndr Gene Ther.*4:6

33. Ross, G. (2000) Regulation of the adhesion versus cytotoxic functions of the Mac-1/. *Crit Rev Immunol.*20(3):197–222.

34. Solovjov DA, P.E., Plow EF. (2005) Distinct roles for the alpha and beta subunits in the functions of integrin alphaMbeta2. *J. Biol. Chem.*280:1336-1345

35. Plow EF, H.T., Zhang L, Loftus J, Smith JW. (2000) Ligand binding to integrins. *J Biol Chem.* .275(29):21785-8

36. Ruoslahti, E. (1996) RGD and other recognition sequences for integrins. *Annu Rev Cell Dev Biol.*12:697-715

37. Nataly P. Podolnikova, A.V.P., Thomas A. Haas, Valeryi K. Lishko, and Tatiana P. Ugarova. (2015) Ligand Recognition Specificity of Leukocyte Integrin αMβ2 (Mac-1, CD11b/CD18) and Its Functional Consequences. *Biochemistry.* 54(6): 1408–1420

38. Diamond, M.S., Staunton, D. E., de Fougerolles, A. R., Stacker, S. (1990) ICAM-1 (CD54): A counter-receptor for Mac-1 (CD11b/CD18). *J. Cell Biol.*,111, 3129−3139.

39. Hermand, P., et al. (2000) Binding sites of leukocyte beta(2) integrins (LFA-1, Mac-1) on the human ICAM-4/LW blood group protein. *Journal of Biological Chemistry.* 275,26002-26010

40. Davis, G.E. (1992) The Mac-1 and P150,95 Beta-2 Integrins Bind Denatured Proteins to Mediate Leukocyte Cell Substrate Adhesion. *Experimental Cell Research.* 200,242-252

41. Thompson, H.L. and K. Matsushima. (1992) Human polymorphonuclear leucocytes stimulated by tumour necrosis factor-alpha show increased adherence to extracellular matrix proteins which is mediated via the CD11b/18 complex. *Clin Exp Immunol.* 90,280-5

42. Monboisse, J.C., et al. (1991) Adhesion of Human Neutrophils to and Activation by Type-I Collagen Involving a Beta-2 Integrin. *Journal of Leukocyte Biology.* 50,373-380

43. Walzog, B., et al. (1995) The Leukocyte Integrin Mac-1 (Cd11b/Cd18) Contributes to Binding of Human Granulocytes to Collagen. *Experimental Cell Research.* 218,28-38

44. Schober, J.M., et al. (2002) Identification of integrin alpha(M)beta(2) as an adhesion receptor on peripheral blood monocytes for Cyr61 (CCN1) and connective tissue growth factor (CCN2): immediate-early gene products expressed in atherosclerotic lesions. *Blood.* 99,4457-65

45. Forsyth, C.B. and H.L. Mathews. (1996) Lymphocytes utilize CD11b/CD18 for adhesion to Candida albicans. *Cellular Immunology*. 170,91-100

46. Gustafson E. J., L.H., Wachtfogel Y. T., Norton K. J., Schmaier A. H., Niewiarowski S., Colman R. W. (1989) High molecular weight kininogen inhibits fibrinogen binding to cytoadhesins of neutrophils and platelets. *J. Cell Biol.*109:377–387

47. Altieri D. C., E.T.S. (1988) The saturable high affinity association of factor X to ADP-stimulated monocytes defines a novel function of the Mac-1 receptor. *J. Biol. Chem.*,63:7007–7015

48. DiScipio R. G., D.P.J., Schraufstatter I. U., Sriramarao P. (1998) Human Polymorphonuclear Leukocytes Adhere to Complement Factor H Through an Interaction That Involves αMβ2 (CD11b/CD18). *J Immunol.*160 (8) 4057-4066;

49. Kotovuori P., T.E., Pigott R., Shepherd M., Kiso M., Hasegawa A., Renkonen R., Nortamo P., Altieri D. C., Gahmberg C. G. (1993) THE VASCULAR E-SELECTIN BINDS TO THE LEUKOCYTE INTEGRINS CD11/CD18. *Glycobiology* 3:131–136.

50. Cai, T.Q., and Wright, S. D. (1996) Human leukocyte elastase isan endogenous ligand for the integrin CR3 (CD11b/CD18, Mac-1, αMβ2) and modulates polymorphonuclear leukocyte adhesion. *J. Exp.Med.* .184, 1213−1223.

51. Johansson, M.W., Patarroyo, M., Oberg, F., Siegbahn, A., and Nilsson, K. (1997) Myeloperoxidase mediates cell adhesion via the αMβ2 integrin (Mac-1, CD11b/CD18). *J. Cell Sci.*,110, 1133−1139.

52. Lishko, V.K., Novokhatny, V., Yakubenko, V. P., Skomorovska-Prokvolit, H., and Ugarova, T. P. (2004) Characterization of plasminogen as an adhesive ligand for integrins αMβ2(Mac-1) and α5β1(VLA-5). *Blood.*104, 719−726.

53. Diamond M. S., A.R., Parkos C. A., Quinn M. T., Springer T. A. (1995) Heparin is an adhesive ligand for the leukocyte integrin Mac-1 (CD11b/CD1). *J. Cell Biol.*,130:1473–1482.

54. Thornton B. P., V.V., Pitman M., Goldman R. C., Ross G. D. (1996) Analysis of the sugar specificity and molecular location of the beta-glucan-binding lectin site of complement receptor type 3 (CD11b/CD18). *J Immunol* 156 (3) 1235-1246;

55. Yakubenko VP, L.V., Lam SC, Ugarova TP. (2002) A molecular basis for integrin alphaMbeta 2 ligand binding promiscuity. *J Biol Chem.*,277(50):48635-42.

56. Podolnikova, N.P., et al. (2015) Ligand recognition specificity of leukocyte integrin alphaMbeta2 (Mac-1, CD11b/CD18) and its functional consequences. *Biochemistry.* 54,1408-20

57. Shen D, P.N., Yakubenko VP, Ardell CL, Balabiyev A, Ugarova TP, Wang X. (2017) Pleiotrophin, a multifunctional cytokine and growth factor, induces leukocyte responses through the integrin Mac-1. *J Biol Chem.* .292(46):18848-18861.

58. Lee, J.O., et al. (1995) Crystal structure of the A domain from the alpha subunit of integrin CR3 (CD11b/CD18). *Cell.* 80,631-8

59. Lee, J.O., et al. (1995) Two conformations of the integrin A-domain (I-domain): a pathway for activation? *Structure.* 3,1333-40

60. Rui Li, P.R., Diana L. Griffith, David Scott, M. Amin Arnaout. (1998) Two Functional States of the CD11b A-Domain: Correlations with Key Features of Two Mn2+-complexed Crystal Structures. *JCB.*143 (6): 1523

61. Claus Oxvig, C.L., and Timothy A. Springer. (1999) Conformational changes in tertiary structure near the ligand binding site of an integrin I domain. *PNAS.*96 (5) 2215-2220

62. Emsley J, K.C., Farndale RW, Barnes MJ, Liddington RC. (2000) Structural basis of collagen recognition by integrin alpha2beta1. *Cell.*101(1):47-56

63. Gonzalez-Castillo, C., et al. (2014) Pleiotrophin as a central nervous system neuromodulator, evidences from the hippocampus. *Front Cell Neurosci.* 8,443

64. Perez-Pinera, P., J.R. Berenson, and T.F. Deuel. (2008) Pleiotrophin, a multifunctional angiogenic factor: mechanisms and pathways in normal and pathological angiogenesis. *Curr Opin Hematol.* 15,210-4

65. Himburg, H.A., et al. (2012) Pleiotrophin regulates the retention and self-renewal of hematopoietic stem cells in the bone marrow vascular niche. *Cell Rep.* 2,964-75

66. Himburg, H.A., et al. (2014) Pleiotrophin mediates hematopoietic regeneration via activation of RAS. *J Clin Invest.* 124,4753-8

67. Hatziapostolou, M., et al. (2005) Heparin affin regulatory peptide is a key player in prostate cancer cell growth and angiogenicity. *Prostate.* 65,151-8

68. Papadimitriou, E., et al. (2009) Roles of pleiotrophin in tumor growth and angiogenesis. *Eur Cytokine Netw.* 20,180-90

69. Jager, R., et al. (1997) Differential expression and biological activity of the heparin-binding growth-associated molecule (HB-GAM) in lung cancer cell lines. *Int J Cancer*. 73,537-43

70. Mentlein, R. and J. Held-Feindt. (2002) Pleiotrophin, an angiogenic and mitogenic growth factor, is expressed in human gliomas. *J Neurochem*. 83,747-53

71. Zhang, N., et al. (1997) Human breast cancer growth inhibited in vivo by a dominant negative pleiotrophin mutant. *J Biol Chem*. 272,16733-6

72. Weber, D., et al. (2000) Pleiotrophin can be rate-limiting for pancreatic cancer cell growth. *Cancer Research*. 60,5284-5288

73. Kong, Y., et al. (2012) Pleiotrophin is a potential colorectal cancer prognostic factor that promotes VEGF expression and induces angiogenesis in colorectal cancer. *International Journal of Colorectal Disease*. 27,287-298

74. Koutsioumpa, M., et al. (2015) Receptor protein tyrosine phosphatase beta/zeta is a functional binding partner for vascular endothelial growth factor. *Molecular Cancer*. 14

75. Yokoi, H., et al. (2012) Pleiotrophin triggers inflammation and increased peritoneal permeability leading to peritoneal fibrosis. *Kidney Int*. 81,160-9

76. Ochiai, K., et al. (2004) The role of midkine and pleiotrophin in liver regeneration. *Liver Int*. 24,484-91

77. Besse, S., et al. (2013) Pleiotrophin promotes capillary-like sprouting from senescent aortic rings. *Cytokine*. 62,44-7

78. Fang, Q., et al. (2013) Pleiotrophin gene therapy for peripheral ischemia: evaluation of full-length and truncated gene variants. *PLoS One*. 8,e61413

79. Silver, K., et al. (2012) Expression of pleiotrophin, an important regulator of cell migration, is inhibited in intestinal epithelial cells by treatment with non-steroidal anti-inflammatory drugs. *Growth Factors*. 30,258-66

80. Yu, Y., et al. (2010) Construction of siRNA lentiviral expressing vector targeting pleiotrophin gene and its impact on growth and apoptosis in H446 cells of human small cell lung cancer. *Zhonghua Jie He He Hu Xi Za Zhi*. 33,289-94

81. Raulo, E., et al. (1994) Isolation of a neuronal cell surface receptor of heparin binding growth-associated molecule (HB-GAM). Identification as N-syndecan (syndecan-3). *J Biol Chem*. 269,12999-3004

82. Meng, K., et al. (2000) Pleiotrophin signals increased tyrosine phosphorylation of beta beta-catenin through inactivation of the intrinsic catalytic activity of the receptor-type protein tyrosine phosphatase beta/zeta. *Proc Natl Acad Sci U S A*. 97,2603-8

83. Maeda, N., et al. (1996) 6B4 proteoglycan/phosphacan, an extracellular variant of receptor-like protein-tyrosine phosphatase zeta/RPTPbeta, binds pleiotrophin/heparin-binding growth-associated molecule (HB-GAM). *J Biol Chem.* 271,21446-52

84. Koutsioumpa, M., et al. (2012) Pleiotrophin expression and role in physiological angiogenesis in vivo: potential involvement of nucleolin. *Vasc Cell.* 4,4

85. Take, M., et al. (1994) Identification of nucleolin as a binding protein for midkine (MK) and heparin-binding growth associated molecule (HB-GAM). *J Biochem.* 116,1063-8

86. Mikelis, C., et al. (2009) Integrin alpha(v)beta(3) is a pleiotrophin receptor required for pleiotrophin-induced endothelial cell migration through receptor protein tyrosine phosphatase beta/zeta. *FASEB J.* 23,1459-69

87. Ryan, E., D. Shen, and X. Wang. (2016) Structural studies reveal an important role for the pleiotrophin C-terminus in mediating interactions with chondroitin sulfate. *FEBS J.* 283,1488-503

88. Kilpelainen, I., et al. (2000) Heparin-binding growth-associated molecule contains two heparin-binding beta -sheet domains that are homologous to the thrombospondin type I repeat. *J Biol Chem.* 275,13564-70

89. Raulo, E., et al. (2005) The two thrombospondin type I repeat domains of the heparin-binding growth-associated molecule bind to heparin/heparan sulfate and regulate neurite extension and plasticity in hippocampal neurons. *J Biol Chem.* 280,41576-83

90. Podolnikova, N.P., J.A. Brothwell, and T.P. Ugarova. (2015) The opioid peptide dynorphin A induces leukocyte responses via integrin Mac-1 (alphaMbeta2, CD11b/CD18). *Mol Pain.* 11,33

91. Coxon, A., et al. (1996) A novel role for the beta 2 integrin CD11b/CD18 in neutrophil apoptosis: a homeostatic mechanism in inflammation. *Immunity.* 5,653-666

92. Lu, H.F., et al. (1997) LFA-1 is sufficient in mediating neutrophil emigration in Mac-1-deficient mice. *Journal of Clinical Investigation.* 99,1340-1350

93. Lishko, V.K., et al. (2004) Multiple binding sites in fibrinogen for integrin alphaMbeta2 (Mac-1). *J Biol Chem.* 279,44897-906

94. Lishko, V.K., et al. (2016) Identification of Human Cathelicidin Peptide LL-37 as a Ligand for Macrophage Integrin alphaMbeta2 (Mac-1, CD11b/CD18) that Promotes Phagocytosis by Opsonizing Bacteria. *Res Rep Biochem.* 2016,39-55

95. Luo, B.H., C.V. Carman, and T.A. Springer. (2007) Structural basis of integrin regulation and signaling. *Annu Rev Immunol.* 25,619-47

96. Yakubenko, V.P., et al. (2001) Identification of the binding site for fibrinogen recognition peptide g 383-395 within the αM I-domain of integrin αMβ2 *Journal of Biological Chemistry.* 275,13995-14003

97. Catanzariti, A.M., et al. (2004) An efficient system for high-level expression and easy purification of authentic recombinant proteins. *Protein Science.* 13,1331-1339

98. Frank, R. (1992) Spot-Synthesis - an Easy Technique for the Positionally Addressable, Parallel Chemical Synthesis on a Membrane Support. *Tetrahedron.* 48,9217-9232

99. Kramer, A. and J. Schneider-Mergener. (1998) Synthesis and screening of peptide libraries on continuous cellulose membrane supports. *Methods Mol Biol.* 87,25-39

100. Delaglio, F., et al. (1995) NMRPipe: a multidimensional spectral processing system based on UNIX pipes. *J Biomol NMR.* 6,277-93

101. Johnson, B.A. (2004) Using NMRView to visualize and analyze the NMR spectra of macromolecules. *Methods Mol Biol.* 278,313-52

102. Forsyth, C.B., et al. (2001) Integrin alpha(M)beta(2)-mediated cell migration to fibrinogen and its recognition peptides. *J Exp Med.* 193,1123-33

103. Lishko, V.K., V.P. Yakubenko, and T.P. Ugarova. (2003) The interplay between integrins alpha(M)beta(2) and alpha(5)beta(1), during cell migration to fibronectin. *Experimental Cell Research.* 283,116-126

104. Take, M., et al. (1994) Identification of Nucleolin as a Binding-Protein for Midkine (Mk) and Heparin-Binding Growth-Associated Molecule (Hb-Gam). *Journal of Biochemistry.* 116,1063-1068

105. Lu, K.V., et al. (2005) Differential induction of glioblastoma migration and growth by two forms of pleiotrophin. *J Biol Chem.* 280,26953-64

106. Schober J. M., C.N., Grzeszkiewicz T., Emeson E. E., Ugarova T. P., Ye, R. D., Lau L. F., Lam S. C. T. (2002) Identification of integrin αMβ2 as an adhesion receptor on peripheral blood monocytes for Cyr61 (CCN1) and connective tissue growth factor (CCN2): immediate-early gene products expressed in atherosclerotic lesions. *Blood.* 99:4457–4465.

107. Cavanagh, J., *Protein NMR spectroscopy : principles and practice*. 2nd ed. 2007, Amsterdam ; Boston: Academic Press. xxv, 885 p.

108. Ding, Z.M., et al. (1999) Relative contribution of LFA-1 and Mac-1 to neutrophil adhesion and migration. *Journal of Immunology.* 163,5029-5038

109. Lishko, V.K., et al. (2016) Identification of Human Cathelicidin Peptide LL-37 as a Ligand for Macrophage Integrin alphaMbeta2 (Mac-1, CD11b/CD18) that Promotes Phagocytosis by Opsonizing Bacteria. *J Biol Chem.* 2016,39-55

110. Ori, A., et al. (2009) Identification of heparin-binding sites in proteins by selective labeling. *Mol Cell Proteomics.* 8,2256-65

111. Diamond, M.S., et al. (1995) Heparin is an adhesive ligand for the leukocyte integrin Mac-1 (CD11b/CD1). *J Cell Biol.* 130,1473-82

112. Ajroud, K., et al. (2004) Binding Affinity of Metal Ions to the CD11b A-domain Is Regulated by Integrin Activation and Ligands. *J Biol Chem.* 279,25483-8

113. Yeh, H.J., et al. (1998) Upregulation of pleiotrophin gene expression in developing microvasculature, macrophages, and astrocytes after acute ischemic brain injury. *J Neurosci.* 18,3699-707

114. Muramatsu, T. (2014) Structure and function of midkine as the basis of its pharmacological effects. *Br J Pharmacol.* 171,814-26

115. Takada, T., et al. (1997) Midkine, a retinoic acid-inducible heparin-binding cytokine, is a novel regulator of intracellular calcium in human neutrophils. *Biochem Biophys Res Commun.* 241,756-61

116. Horiba, M., et al. (2000) Neointima formation in a restenosis model is suppressed in midkine-deficient mice. *Journal of Clinical Investigation.* 105,489-495

117. Sato, W., et al. (2001) Midkine is involved in neutrophil infiltration into the tubulointerstitium in ischemic renal injury. *Journal of Immunology.* 167,3463-3469

118. Kadomatsu, K. (2005) The midkine family in cancer, inflammation and neural development. *Nagoya J Med Sci.* 67,71-82

119. Muramatsu, H., et al. (2004) alpha4beta1- and alpha6beta1-integrins are functional receptors for midkine, a heparin-binding growth factor. *J Cell Sci.* 117,5405-15

120. Weckbach, L.T., et al. (2014) The cytokine midkine supports neutrophil trafficking during acute inflammation by promoting adhesion via beta2 integrins (CD11/CD18). *Blood.* 123,1887-96

121. Achour, A., et al. (2008) Pleiotrophin induces expression of inflammatory cytokines in peripheral blood mononuclear cells. *Biochimie.* 90,1791-5

122. Hynes, R.O. (1992) Integrins: versatility, modulation, and signaling in cell adhesion. *Cell.* 69,11-25

123. Michishita, M., V. Videm, and M.A. Arnaout. (1993) A novel divalent cation-binding site in the A domain of the beta 2 integrin CR3 (CD11b/CD18) is essential for ligand binding. *Cell.* 72,857-67

124. Kamata, T. and Y. Takada. (1994) Direct binding of collagen to the I domain of integrin alpha 2 beta 1 (VLA-2, CD49b/CD29) in a divalent cation-independent manner. *J Biol Chem.* 269,26006-10

125. Tuckwell, D., et al. (1995) Integrin alpha 2 I-domain is a binding site for collagens. *J Cell Sci.* 108 (Pt 4),1629-37

126. Mould, A.P., et al. (1997) Defining the topology of integrin alpha5beta1-fibronectin interactions using inhibitory anti-alpha5 and anti-beta1 monoclonal antibodies. Evidence that the synergy sequence of fibronectin is recognized by the amino-terminal repeats of the alpha5 subunit. *J Biol Chem.* 272,17283-92

127. Larson, R.S. and T.A. Springer. (1990) Structure and function of leukocyte integrins. *Immunol Rev.* 114,181-217

128. Graff, J.C. and M.A. Jutila. (2007) Differential regulation of CD11b on gammadelta T cells and monocytes in response to unripe apple polyphenols. *J Leukoc Biol.* 82,603-7

129. Ehlers, M.R. (2000) CR3: a general purpose adhesion-recognition receptor essential for innate immunity. *Microbes Infect.* 2,289-94

130. Kinashi, T. (2007) Integrin regulation of lymphocyte trafficking: lessons from structural and signaling studies. *Adv Immunol.* 93,185-227

131. Emsley, J., et al. (2000) Structural basis of collagen recognition by integrin alpha2beta1. *Cell.* 101,47-56

132. Xiong, J.P., et al. (2000) An isoleucine-based allosteric switch controls affinity and shape shifting in integrin CD11b A-domain. *J Biol Chem.* 275,38762-7

133. Kamata, T., W. Puzon, and Y. Takada. (1994) Identification of putative ligand binding sites within I domain of integrin alpha 2 beta 1 (VLA-2, CD49b/CD29). *J Biol Chem.* 269,9659-63

134. Bajic, G., et al. (2013) Structural insight on the recognition of surface-bound opsonins by the integrin I domain of complement receptor 3. *Proc Natl Acad Sci U S A.* 110,16426-31

135. Lishko, V.K., et al. (2018) Leukocyte integrin Mac-1 (CD11b/CD18, alphaMbeta2, CR3) acts as a functional receptor for platelet factor 4. *J Biol Chem.* 293,6869-6882

136. D.A. Case, R.M.B., D.S. Cerutti, T.E. Cheatham, III, T.A. Darden, R.E. Duke, T.J. Giese, H. Gohlke,, et al. (2016) AMBER 2016.

137. Debiec, K.T., et al. (2016) Further along the Road Less Traveled: AMBER ff15ipq, an Original Protein Force Field Built on a Self-Consistent Physical Model. *Journal of Chemical Theory and Computation.* 12,3926-3947

138. Kufareva, I. and R. Abagyan. (2012) Methods of protein structure comparison. *Methods Mol Biol.* 857,231-57

139. Greenfield, N.J. (2006) Using circular dichroism spectra to estimate protein secondary structure. *Nature Protocols.* 1,2876-2890

140. Calderwood, D.A., et al. (1997) The integrin alpha1 A-domain is a ligand binding site for collagens and laminin. *J Biol Chem.* 272,12311-7

141. Gotwals, P.J., et al. (1999) Divalent cations stabilize the alpha 1 beta 1 integrin I domain. *Biochemistry.* 38,8280-8

142. Diamond, M.S., et al. (1993) The I domain is a major recognition site on the leukocyte integrin MAC-1 (CD11b/CD18) for four distinct adhesion ligands. *Journal of Cell Biology.* 120,1031-1043

143. Lambert, L.J., et al. (2008) Competitive interactions of collagen and a jararhagin-derived disintegrin peptide with the integrin alpha2-I domain. *J Biol Chem.* 283,16665-72

144. Adair, B.D., et al. (2013) EM structure of the ectodomain of integrin CD11b/CD18 and localization of its ligand-binding site relative to the plasma membrane. *PLoS One.* 8,e57951

145. Hynes, R.O. (2002) Integrins: bidirectional, allosteric signaling machines. *Cell.* 110,673-87

146. Luo, B.H., T.A. Springer, and J. Takagi. (2003) Stabilizing the open conformation of the integrin headpiece with a glycan wedge increases affinity for ligand. *Proc Natl Acad Sci U S A.* 100,2403-8

147. Xiong, J.P., et al. (2009) Crystal structure of the complete integrin alphaVbeta3 ectodomain plus an alpha/beta transmembrane fragment. *J Cell Biol.* 186,589-600

148. Askari, J.A., et al. (2010) Focal adhesions are sites of integrin extension. *J Cell Biol.* 188,891-903

149. Chen, X., et al. (2012) Molecular basis for complement recognition by integrin alphaXbeta2. *Proc Natl Acad Sci U S A.* 109,4586-91

150. Schurpf, T. and T.A. Springer. (2011) Regulation of integrin affinity on cell surfaces. *EMBO J.* 30,4712-27

151. Lu, C., et al. (2001) Epitope mapping of antibodies to the C-terminal region of the integrin beta 2 subunit reveals regions that become exposed upon receptor activation. *J Immunol.* 166,5629-37

152. Mould, A.P., et al. (2003) Conformational changes in the integrin beta A domain provide a mechanism for signal transduction via hybrid domain movement. *J Biol Chem.* 278,17028-35

153. Arnaout, M.A. (1990) Leukocyte adhesion molecules deficiency: its structural basis, pathophysiology and implications for modulating the inflammatory response. *Immunol Rev.* 114,145-80

154. Xie, C., et al. (2010) Structure of an integrin with an alphaI domain, complement receptor type 4. *Embo j.* 29,666-79

155. Xu, S., et al. (2017) Distinct recognition of complement iC3b by integrins alphaXbeta2 and alphaMbeta2. *Proc Natl Acad Sci U S A.* 114,3403-3408

156. Fan, Z., et al. (2016) Neutrophil recruitment limited by high-affinity bent beta2 integrin binding ligand in cis. *Nat Commun.* 7,12658

157. Ye, F., et al. (2010) Recreation of the terminal events in physiological integrin activation. *J Cell Biol.* 188,157-73

158. Alon, R. and K. Ley. (2008) Cells on the run: shear-regulated integrin activation in leukocyte rolling and arrest on endothelial cells. *Curr Opin Cell Biol.* 20,525-32

159. Puklin-Faucher, E., et al. (2006) How the headpiece hinge angle is opened: new insights into the dynamics of integrin activation. *Journal of Cell Biology.* 175,349-360

160. Zhu, J., et al. (2008) Structure of a complete integrin ectodomain in a physiologic resting state and activation and deactivation by applied forces. *Mol Cell.* 32,849-61

161. Friedland, J.C., M.H. Lee, and D. Boettiger. (2009) Mechanically activated integrin switch controls alpha5beta1 function. *Science.* 323,642-4

162. Cai, T.Q. and S.D. Wright. (1995) Energetics of leukocyte integrin activation. *J Biol Chem.* 270,14358-65

163. Gingras, A.R., F. Ye, and M.H. Ginsberg. (2013) Reconstructing integrin activation in vitro. *Methods Mol Biol.* 1046,1-17

164. Kavran, J.M. and D.J. Leahy. (2014) Coupling antibody to cyanogen bromide-activated sepharose. *Methods Enzymol.* 541,27-34

165. Xiong, J.P., et al. (2001) Crystal structure of the extracellular segment of integrin alpha Vbeta3. *Science.* 294,339-45

166. Adair, B.D. and M. Yeager. (2002) Three-dimensional model of the human platelet integrin alpha IIbbeta 3 based on electron cryomicroscopy and x-ray crystallography. *Proc Natl Acad Sci U S A.* 99,14059-64

167. Xu, X.P., et al. (2016) Three-Dimensional Structures of Full-Length, Membrane-Embedded Human alpha(IIb)beta(3) Integrin Complexes. *Biophys J.* 110,798-809

168. Fernandez-Leiro, R. and S.H.W. Scheres. (2017) A pipeline approach to single-particle processing in RELION. *Acta Crystallogr D Struct Biol.* 73,496-502

169. Hagn, F., et al. (2013) Optimized phospholipid bilayer nanodiscs facilitate high-resolution structure determination of membrane proteins. *J Am Chem Soc.* 135,1919-25

170. Denisov, I.G., et al. (2004) Directed self-assembly of monodisperse phospholipid bilayer Nanodiscs with controlled size. *J Am Chem Soc.* 126,3477-87

171. Katayama, H., et al. (2010) Three-dimensional structure of the anthrax toxin pore inserted into lipid nanodiscs and lipid vesicles. *Proc Natl Acad Sci U S A.* 107,3453-7

172. Denisov, I.G. and S.G. Sligar. (2011) Cytochromes P450 in nanodiscs. *Biochim Biophys Acta.* 1814,223-9

173. Raschle, T., et al. (2009) Structural and functional characterization of the integral membrane protein VDAC-1 in lipid bilayer nanodiscs. *J Am Chem Soc.* 131,17777-9

174. Liddington, R.C. and M.H. Ginsberg. (2002) Integrin activation takes shape. *J Cell Biol.* 158,833-9

175. Carman, C.V. and T.A. Springer. (2003) Integrin avidity regulation: are changes in affinity and conformation underemphasized? *Curr Opin Cell Biol.* 15,547-56

176. Bazzoni, G. and M.E. Hemler. (1998) Are changes in integrin affinity and conformation overemphasized? *Trends Biochem Sci.* 23,30-4

177. Takagi, J., et al. (2003) Structure of integrin alpha5beta1 in complex with fibronectin. *EMBO J.* 22,4607-15

178. Chen, X., et al. (2010) Requirement of open headpiece conformation for activation of leukocyte integrin alphaXbeta2. *Proc Natl Acad Sci U S A.* 107,14727-32

179. Nishida, N., et al. (2006) Activation of leukocyte beta2 integrins by conversion from bent to extended conformations. *Immunity.* 25,583-94

180. Eng, E.T., et al. (2011) Intact alphaIIbbeta3 integrin is extended after activation as measured by solution X-ray scattering and electron microscopy. *J Biol Chem.* 286,35218-26

181. Hanein, D. and N. Volkmann. (2018) Conformational Equilibrium of Human Platelet Integrin Investigated by Three-Dimensional Electron Cryo-Microscopy. *Subcell Biochem.* 87,353-363

182. Lu, C.F. and T.A. Springer. (1997) The α subunit cytoplasmic domain regulates the assembly and adhesiveness of integrin lymphocyte function-associated antigen-1. *Journal of Immunology.* 159,268-278

183. Bergelson, J.M., et al. (1993) The integrin VLA-2 binds echovirus 1 and extracellular matrix ligands by different mechanisms. *J Clin Invest.* 92,232-9

184. Gonzalez-Castillo, C., et al. (2015) Pleiotrophin as a central nervous system neuromodulator evidences from the hippocampus. *Frontiers in Cellular Neuroscience.* 8

185. Fernandez-Calle, R., et al. (2017) Pleiotrophin regulates microglia-mediated neuroinflammation. *J Neuroinflammation.* 14,46

186. Jokinen, J., et al. (2010) Molecular mechanism of alpha2beta1 integrin interaction with human echovirus 1. *EMBO J.* 29,196-208

187. Tonks, N.K. and B.G. Neel. (1996) From form to function: signaling by protein tyrosine phosphatases. *Cell.* 87,365-8

188. Ostman, A., C. Hellberg, and F.D. Bohmer. (2006) Protein-tyrosine phosphatases and cancer. *Nat Rev Cancer.* 6,307-20

189. Druker, B.J., et al. (1996) Effects of a selective inhibitor of the Abl tyrosine kinase on the growth of Bcr-Abl positive cells. *Nat Med.* 2,561-6

190. Hynes, N.E. and H.A. Lane. (2005) ERBB receptors and cancer: the complexity of targeted inhibitors. *Nat Rev Cancer.* 5,341-54

191. He, R., et al. (2013) Small molecule tools for functional interrogation of protein tyrosine phosphatases. *FEBS J.* 280,731-50

192. Hunter, T. and B.M. Sefton. (1980) Transforming gene product of Rous sarcoma virus phosphorylates tyrosine. *Proc Natl Acad Sci U S A.* 77,1311-5

193. Nikolaienko, R.M., B. Agyekum, and S. Bouyain. (2012) Receptor protein tyrosine phosphatases and cancer: new insights from structural biology. *Cell Adh Migr.* 6,356-64

194. Schlessinger, J. (2002) Ligand-induced, receptor-mediated dimerization and activation of EGF receptor. *Cell.* 110,669-72

195. Julien, S.G., et al. (2011) Inside the human cancer tyrosine phosphatome. *Nat Rev Cancer.* 11,35-49

196. Krueger, N.X. and H. Saito. (1992) A human transmembrane protein-tyrosine-phosphatase, PTP zeta, is expressed in brain and has an N-terminal receptor domain homologous to carbonic anhydrases. *Proc Natl Acad Sci U S A.* 89,7417-21

197. Harroch, S., et al. (2000) No obvious abnormality in mice deficient in receptor protein tyrosine phosphatase beta. *Molecular and Cellular Biology.* 20,7706-7715

198. Lamprianou, S., et al. (2006) Receptor protein tyrosine phosphatase gamma is a marker for pyramidal cells and sensory neurons in the nervous system and is not necessary for normal development. *Molecular and Cellular Biology.* 26,5106-5119

199. Milner, P.G., et al. (1989) A novel 17 kD heparin-binding growth factor (HBGF-8) in bovine uterus: purification and N-terminal amino acid sequence. *Biochem Biophys Res Commun.* 165,1096-103

200. Rauvala, H. (1989) An 18-kd heparin-binding protein of developing brain that is distinct from fibroblast growth factors. *EMBO J.* 8,2933-41

201. Li, Y.S., et al. (1990) Cloning and expression of a developmentally regulated protein that induces mitogenic and neurite outgrowth activity. *Science.* 250,1690-4

202. Li, Y.S., M. Gurrieri, and T.F. Deuel. (1992) Pleiotrophin gene expression is highly restricted and is regulated by platelet-derived growth factor. *Biochem Biophys Res Commun.* 184,427-32

203. Mikelis, C. and E. Papadimitriou. (2008) Heparin-binding protein pleiotrophin: an important player in the angiogenic process. *Connect Tissue Res.* 49,149-52

204. Papadimitriou, E., et al. (2016) Pleiotrophin and its receptor protein tyrosine phosphatase beta/zeta as regulators of angiogenesis and cancer. *Biochim Biophys Acta.* 1866,252-265

205. Chauhan, A.K., Y.S. Li, and T.F. Deuel. (1993) Pleiotrophin transforms NIH 3T3 cells and induces tumors in nude mice. *Proc Natl Acad Sci U S A.* 90,679-82

206. Fang, W., et al. (1992) Pleiotrophin stimulates fibroblasts and endothelial and epithelial cells and is expressed in human cancer. *J Biol Chem.* 267,25889-97

207. Wellstein, A., et al. (1992) A heparin-binding growth factor secreted from breast cancer cells homologous to a developmentally regulated cytokine. *J Biol Chem.* 267,2582-7

208. Tsutsui, J., et al. (1993) A new family of heparin-binding growth/differentiation factors: increased midkine expression in Wilms' tumor and other human carcinomas. *Cancer Res.* 53,1281-5

209. Nakagawara, A., et al. (1993) Association between high levels of expression of the TRK gene and favorable outcome in human neuroblastoma. *N Engl J Med.* 328,847-54

210. Fukada, M., et al. (2006) Protein tyrosine phosphatase receptor type Z is inactivated by ligand-induced oligomerization. *FEBS Lett.* 580,4051-6

211. Maeda, N., et al. (2003) Heterogeneity of the chondroitin sulfate portion of phosphacan/6B4 proteoglycan regulates its binding affinity for pleiotrophin/heparin binding growth-associated molecule. *J Biol Chem.* 278,35805-11

212. Kuboyama, K., et al. (2016) Role of Chondroitin Sulfate (CS) Modification in the Regulation of Protein-tyrosine Phosphatase Receptor Type Z (PTPRZ) Activity: PLEIOTROPHIN-PTPRZ-A SIGNALING IS INVOLVED IN OLIGODENDROCYTE DIFFERENTIATION. *J Biol Chem.* 291,18117-28

213. Maeda, N., et al. (1994) Multiple receptor-like protein tyrosine phosphatases in the form of chondroitin sulfate proteoglycan. *FEBS Lett.* 354,67-70

214. Fujikawa, A., et al. (2003) Mice deficient in protein tyrosine phosphatase receptor type Z are resistant to gastric ulcer induction by VacA of Helicobacter pylori. *Nat Genet.* 33,375-81

215. Huang, P., et al. (2018) Chemotherapy-driven increases in the CDKN1A/PTN/PTPRZ1 axis promote chemoresistance by activating the NF-kappaB pathway in breast cancer cells. *Cell Commun Signal.* 16,92

APPENDIX A

BINDING STUDY BETWEEN PLEIOTROPHIN AND PROTEIN TYROSINE PHOSPHATASE RECEPTOR TYPE Z

Abstract

Protein tyrosine phosphorylation has been studied for many years because of its critical role in cell signaling pathways that control various cellular events such as cell proliferation, differentiation, migration, and death. It has been commonly accepted that many cancers are associated with aberrant phosphotyrosine signaling issued from the unbalanced activities of tyrosine kinases and tyrosine phosphatases. Compared to the understanding of protein tyrosine kinases, our understanding of the regulatory mechanism of protein tyrosine phosphatase is very limited. Protein tyrosine phosphatase receptor type Z (PTPRZ) is one of the protein tyrosine phosphatase receptors which have been overexpressed in many cancers including glioblastoma, a malignant brain cancer. Previous research revealed a ligand of PTPRZ, a glycosaminoglycan binding growth factor called pleiotrophin (PTN), induced glioblastoma metastasis through regulating PTPRZ activity. Although many pieces of evidence suggested that PTN can induce deactivation of PTPRZ phosphatase activity by inducing PTPRZ oligomerization, some details in the molecular mechanism of PTN and PTPRZ interaction remain unclear. In this study, we test the hypothesis that PTN may crosslink PTPRZ monomer by interacting with PTPRZ extracellular core protein. To confirm the hypothesis, we expressed a short peptide based on the sequence of PTPRZ and confirmed the binding between PTN and PTPRZ peptide using solution NMR.

Introduction

Tyrosine phosphorylation of protein plays an essential role in signal regulatory pathways controlling various cellular events such as cell proliferation, differentiation,

migration, and death (187). For many years, people have endeavored to associate aberrant phosphotyrosine signaling to cancers and tried to develop potential therapeutic targets based on crucial proteins in those signaling pathways (188-192). Many studies have shown that aberrant cellular functions of cancer cells are caused by an imbalance in phosphorylation states of key signaling molecules (193). And in the eukaryotic cell, the net tyrosine phosphorylation level is controlled by the activity balance between protein tyrosine kinases (PTKs) and protein tyrosine phosphatase (PTPs). The function regulatory mechanism of the receptor-type PTK (RPTK) has been well studied: the ligand-induced RPTK dimerization leads to transphosphorylation of key tyrosine residues on PTK which causes the increase in PTK activity (194). In contrast, the regulatory mechanism of the receptor-type PTP (RPTP) is understudied.

There are 107 members in the PTP family which are classified into four classes based on the amino acid sequence of catalytic domains. Among those PTPs, 21 PTPs exist in a receptor form (RPTPs) (195). Most of RPTPs are comprised of a large multi-component extracellular domain, a single transmembrane helix, and two intracellular catalytic protein tyrosine phosphates domains. Protein tyrosine phosphatase receptor type Z (PTPRZ/PTPξ/RPTPβ) is one of the RPTP which is prevailingly found in the central nervous system and glioblastoma, an aggressive malignant brain cancer (196-198). Comparing to other RPTP, PTPRZ has a unique extracellular domain comprised of a carbonic anhydrase domain, a fibronectin type III domain and a long unstructured chondroitin sulfate glycosylated “stem” region (Figure A.1).

In 1996, Masaharu Noda and his colleagues first found a ligand of PTPRZ: pleiotrophin (PTN) (83). PTN is a multi-functional, cationic, glycosaminoglycan-binding cytokine and growth factor that is expressed mainly in the neural system (199-202). And PTN plays crucial roles in numerous physiological and pathological processes such as cell growth, neural regeneration, angiogenesis, inflammation, and tumor growth (201, 203, 204). It has been confirmed that *Ptn* gene is a protooncogene, and the deregulation of *Ptn* gene expression caused tumor progression and metastasis (205). Many human tumors and tumor-derived cell lines overexpress PTN (206-209).

Four years later, after the first identification of PTN as the PTPRZ ligand, Meng and colleagues demonstrated that PTN binds and deactivates PTPRZ function on glioblastoma cells U373MG (82). And in 2006, Noda's group revealed that the activity of PTPRZ is depended on its oligomerization state, and PTN induced PTPRZ dimerization which caused the deactivation of PTPRZ (Figure A.1) (210). Although, these researches gave us a better understanding of PTPRZ function regulation, the structural biology study of PTPRZ and PTN interaction is still lacking because of difficulties in studying long unstructured PTPRZ stem regions.

As mentioned before, PTPRZ is a chondroitin sulfate proteoglycan. And PTN, as a glycosaminoglycan (GAG)-binding cytokine, naturally has been assumed to bind to PTPRZ through GAG. In addition, there is evidence shown that chondroitin sulfate glycosylation plays a crucial role in the regulation of PTPRZ activity and the deglycosylation of PTPRZ using chondroitinase ABC caused a decrease in PTN's affinity for PTPRZ (211, 212). Even though many results pointed out that PTN can bind to

PTPRZ through GAG, there are still some unexplained observations. For example, PTPRZ has been found to exist in three splicing variants: PTPRZ-A, a full-length form; PTPRZ-B, a short receptor form; and PTPRZ-S a secretory variant (213). And some of them were expressed in a non-proteoglycan form (214). The study has shown that PTN still inhibited non-proteoglycan PTPRZ in cancers (215). Furthermore, although deglycosylation of PTPRZ reduced the PTN binding affinity, the chondroitinase ABC digested PTPRZ still exhibited significant affinity to PTN with a Kd in nM range (211). Those observations caused us to ask the question： does PTN also bind to the PTPRZ core protein?

Initially, we hypothesized that PTN deactivated PTPRZ by crosslinking of two PTPRZ monomers. Based on observations from previous researches, we proposed two hypothetical crosslinking mechanisms: 1. PTN crosslinks the PTPRZ through the interaction with chondroitin sulfate; 2. PTN crosslinks the PTPRZ through the interaction with PTPRZ core protein (Figure A.1). To test our second hypothesis, we examined the sequence of the PTPRZ ectodomain and found a region of the stem region that contains a high proportion of acidic amino acids. Because of the basic nature of PTN, we believe this part of PTPRZ may constitute an ideal binding site for PTN. To prove this hypothesis, we recombinantly expressed the peptide and tested its interaction with PTN using solution NMR. Data showed that PTN has a significant affinity for this PTPRZ derived peptide. This result supported the second hypothesis to some extent and opens the possibility that PTN has a functional effect on both proteoglycan and non-proteoglycan

forms of the PTPRZ as a result of its interactions with both chondroitin sulfate and PTPRZ core protein itself.

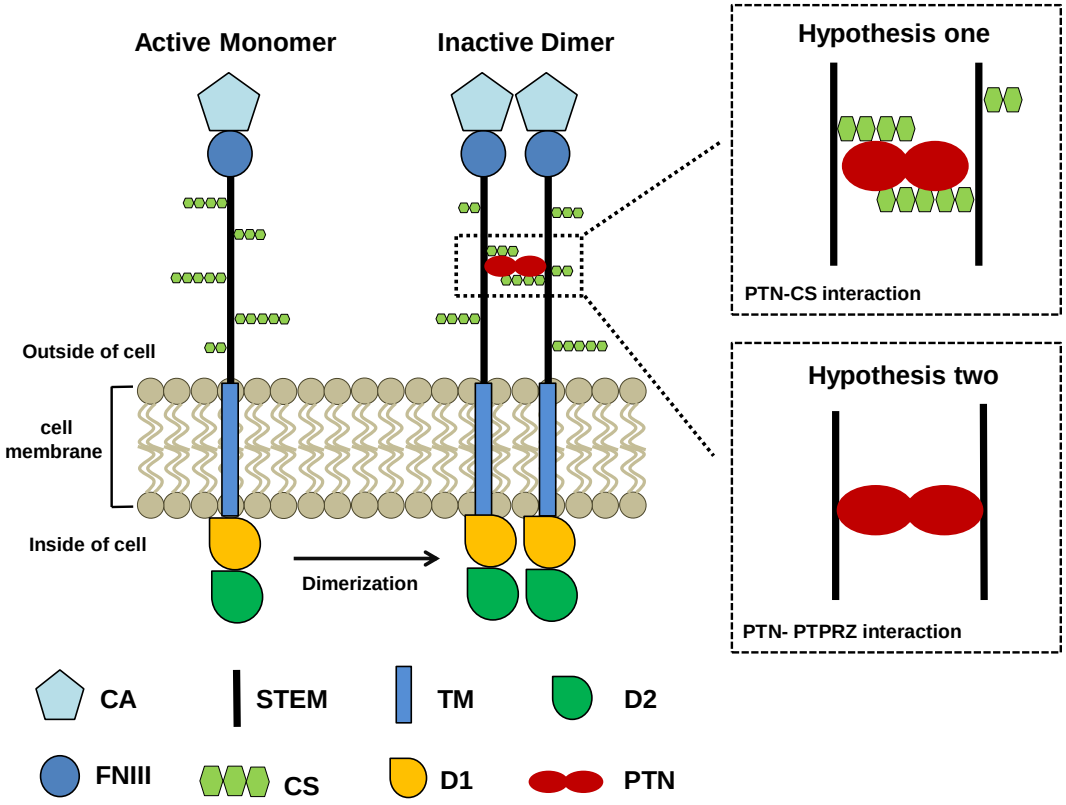

Figure A.1 Architecture of PTPRZ and the Schematic of Proposed Ligand-induced PTPRZ Dimerization

The extracellular part includes a carbonic anhydrase domain (CA), a fibronectin type III domain (FNIII) and an unstructured core protein region (STEM). The STEM region is glycosylated with chondroitin sulfate (CS). The transmembrane domain is labeled as TM. The intracellular regions are composed of two tyrosine phosphatase domains named D1 and D2. D1 is a catalytic domain whereas D2 is not. Pleiotrophin as the PTPRZ ligand is label as PTN. We propose the following PTN induced PTPRZ dimerization mechanisms: PTN crosslinking PTPRZ trough the binding to chondroitin sulfate, and PTN crosslinking PTPRZ trough the binding to PTPRZ STEM core protein.

Materials and Methods

1, PTPRZ residues charge mapping and molecular cloning

The sequence of the PTPRZ extracellular domain (A22- K1636) is mapped with the EMBOSS bioinformatics server to make the charge plot. The ORF (G1414- K1441) for the 28 amino acid PTPRZ-acidic (PTPRZ-ac) peptide was cloned into the pHUE plasmid using SacII and HindIII restriction sites. The correct cloning was confirmed by Sanger sequencing.

2, Expression and purification of recombinant protein and peptide

PTN expression and purification were performed in the same way as mentioned in chapter 2 and chapter 3 (87). The purified PTN was buffer exchanged and stored in buffer 10 mM MES and 150 mM NaCl, pH 6.0 before use.

The PTPRZ-ac pHUE vector was transformed into BL21 DE3 for expression. The cells were grown in M9 media and the protein expression was induced by adding 0.5 mM IPTG when culture OD_{600} reached 0.8. Then the culture was incubated at room temperature overnight and the cell pellets were collected and harvested on the second day. To prepare ^{15}N isotopically labeled proteins, NH_4Cl was replaced by $^{15}NH_4Cl$ in M9 media. The purification procedure is the same as His-tagged-ubiquitin-integrin αM I-domain described in chapter 3. In brief, the His-tagged ubiquitin-PTPRZ-ac fusion protein was purified by Ni-affinity chromatography, and the ubiquitin His-tag was removed by USP2 ubiquitinase. The final product was confirmed using tricine SDS-PAGE electrophoresis.

3. Collection and analysis of NMR data

NMR data for ^{15}N PTN and ^{15}N PTPRZ-ac peptide was collected from Bruker 600 MHz Avance III HD spectrometer (Bruker Instruments, Inc., Bellerica, MA, USA) equipped with a Prodigy probe. The assignment of PTN ^{1}H-^{15}N HSQC abstained from previous research (87). All data were processed using NMRPipe (100) and analyzed using NMRView (101). For the titration of ^{15}N PTN with PTPRZ-ac peptide, 50 μM ^{15}N PTN was mixed with PTPRZ-ac peptide stock solution to produced final PTPRZ-ac peptide concentration of 25, 50, 100, 150, 200μM. For the titration of ^{15}N PTPRZ-ac peptide with PTN, 50 μM ^{15}N PTPRZ-ac peptide was mixed with PTN stock solution to reach the PTN concentrations of 25, 50,100, 150, 200, 250μM. At each increment in the titrations, a ^{1}H-^{15}N HSQC spectrum was acquired individually. The chemical shift changes in the ^{1}H and ^{15}N dimensions were measured and normalized to a single value using the equation $\delta=(\Delta\delta_H^2+ (0.17\times \Delta\delta_N)^2)^{1/2}$, in which $\Delta\delta_H$ and $\Delta\delta_N$ represent the chemical shift changes in ^{1}H and ^{15}N dimensions in ppm. The proton chemical shifts were referenced to internal sodium 3-(trimethylsilyl) propane-1-sulfonate and ^{15}N resonances were referenced indirectly to sodium 3-(trimethylsilyl) propane-1-sulfonate. The Kd values calculated based on the fitting curves of normalized chemical shift changes versus ligand concentration using the one site-specific binding with Hill slope fitting model in GraphPad Prism software. The equation to fit the Kd is: Y=Bmax*X^h/(Kd^h + X^h), where X is the ligand concentration, Y is the normalized chemical shift changes, Bmax is the maximum binding in the same unit as Y, Kd is the same unit as X and h is the Hill slope. If the h=1, this is the ordinary binding equation, if the h=2, this is for binding of a dimer.

Results

1. Titration of PTPRZ-ac peptide with PTN

Because PTN is a highly positively charged protein, we assumed that the PTN binding region on PTPRZ should be the region that is negatively charged. By calculating the amino acid charge distribution in the unstructured STEM region of PTPRZ, we identified a region exhibiting high negative charges (Figure A.2A). Here, we have successfully cloned this negatively charged sequence and inserted it into an expression vector. This short peptide was named "PTPRZ-ac peptide", in which "ac" stands for acidic. The PTPRZ-ac peptide was expressed in ^{15}N M9 media and purified to investigate its interaction with PTN using solution NMR techniques. As shown in Figure A.2B, we

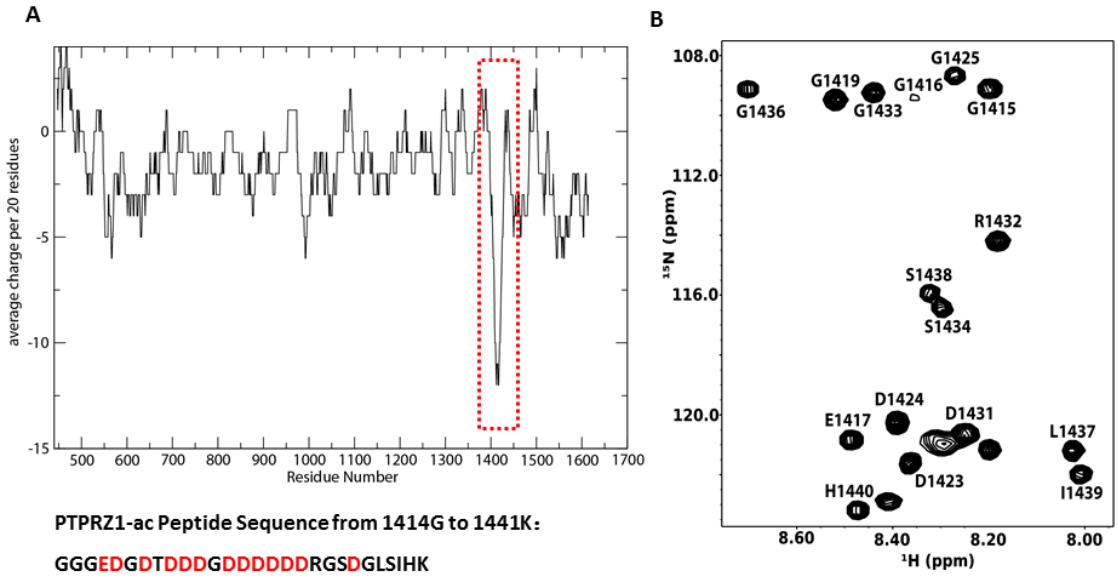

Figure A.2 PTPRZ-ac Peptide
(A) The average amino acid charge mapping through PTPRZ extracellular stem segment. The highly negatively charged sequence was highlighted by the red box. The PTPRZ-ac peptide sequence was shown below the plot. The acidic amino acids including aspartic acid and glutamic acid are labeled red. (B) the ^{15}N-HSQC spectrum of PTPRZ-ac peptide with assignments.

were able to assign 16 residues in PTPRZ-ac peptide $^{1}H^{15}N$ HSQC. However, as a result of sequence repetition, we cannot assign all the adjacent aspartic acids and some of the residues did not produce a signal in the spectrum.

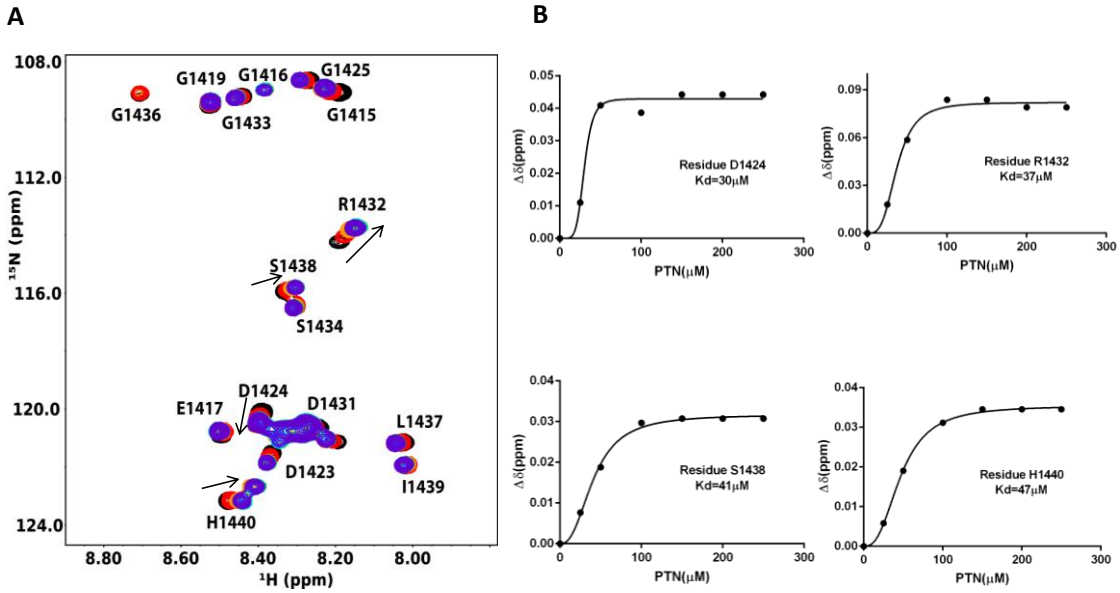

Figure A.3 Titration of PTPRZ-ac Peptide with PTN
(A) ^{15}N HSQC overlay of PTPRZ-ac peptide at different concentrations of PTN. The residues with large chemical shift changes are labeled and their movements are indicated by arrows. (B) the binding curves of four residues showed perturbation in PTN binding. The Kd was calculated individually and labeled on each plot.

For estimating the binding affinity between PTPRZ-ac peptide and PTN, we performed ^{15}N PTPRZ-ac peptide titration with the PTN. As shown in Figure A.3A, the PTN binding induced some PTPRZ-ac peptide peak chemical shift changes. The spectra, collected with various concentrations of PTN, were labeled with different colors. By fitting the chemical shift change as the function of the concentration of PTN, we were able to calculate the equilibrium dissociation constant (Kd) for those peaks that exhibited a significant shift. Figure A.3B shows the Kd fitting curve of four residues whose

chemical shifts were perturbed significantly. Based on the data from those four residues, the average Kd is 39 μM which confirmed that PTN can bind to PTPRZ core protein with significant affinity. Interestingly, the Hill coefficient of the fitting is ~ 1.9, indicating as many as two molecules of PTN may bind to the peptide simultaneously.

2. Titration of PTN with PTPRZ-ac peptide

To further study the interaction of PTN and PTPRZ-ac peptide, we have also performed the ^{15}N PTN titration with the various concentrations of PTPRZ-ac peptide. Compared to PTPRZ-ac peptide titration, PTN titration showed more chemical shift perturbations as shown in Figure A.4. Figure A.4A is the overlap of PTN ^{15}N HSQC spectra in the presence of different concentrations of PTPRZ-ac peptide.

We have chosen eight peaks which showed large chemical shift changes for calculating the binding disassociate constants (Kd) shown in Figure A.4B. The Kd values from different residues are in the range from 30μM to 88 μM, which is in agreement with previous PTPRZ-ac peptide titration data. The HSQCs data showed that PTPRZ-ac peptide-binding induced the PTN chemical shift change in the residues throughout the protein. However, the largest perturbed residues (Q62, F63, G64, C67, N96, L94) are from the hinge region on the C-terminal domain (CTD) shown in Figure A.5 the chemical shift perturbation mapping. This indicated that CTD may be the major PTN binding site for this acidic peptide.

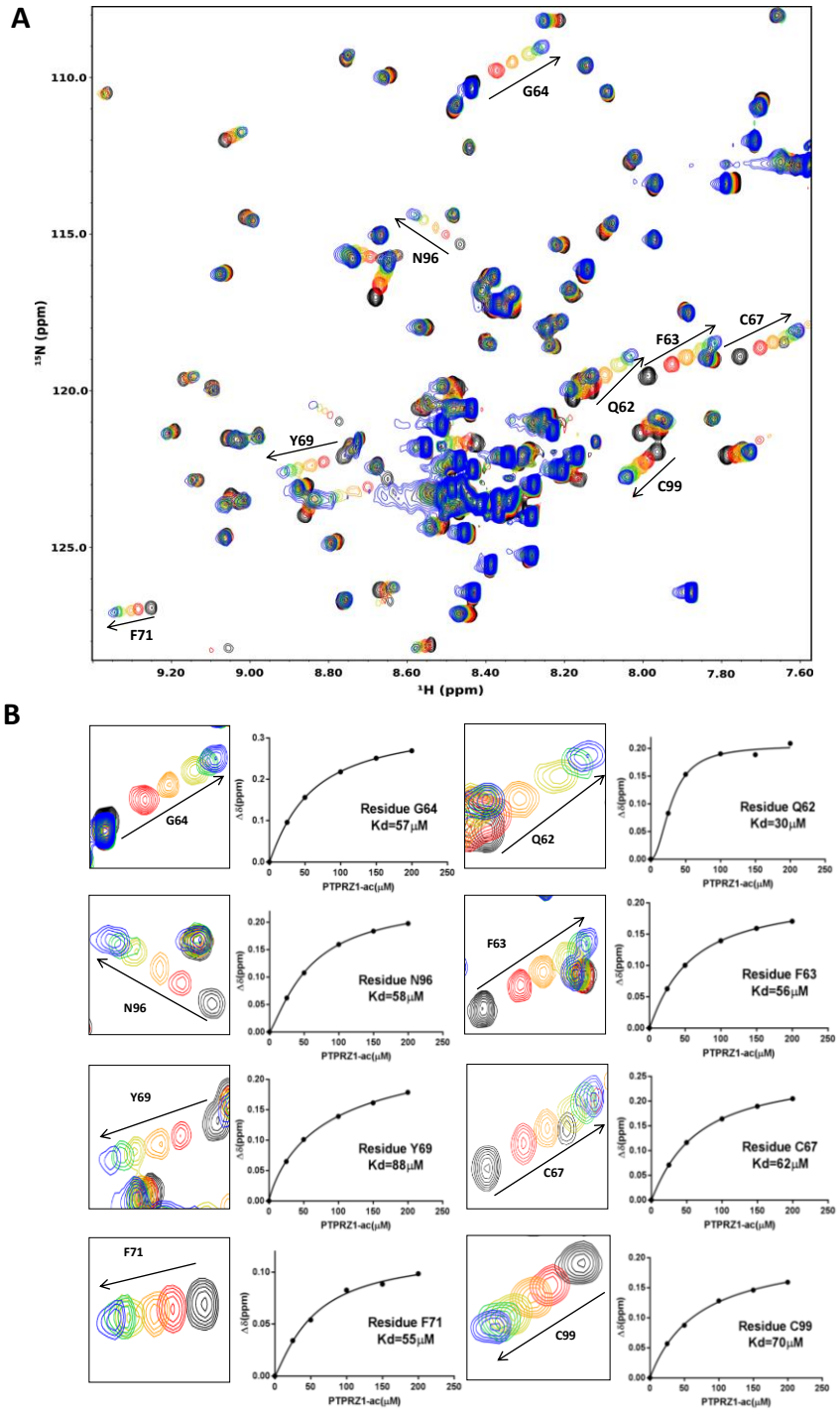

Figure A.4 Titration of PTN with PTPRZ-ac Peptide
(A) ^{15}N HSQC overlay of PTN at different concentration of PTPRZ-ac peptide. The residues with large chemical shift changes are labeled and their movements are indicated by arrows. (B) Representative peak shifts and the binding curves of each residue. The Kd was calculated individually and labeled on each plot.

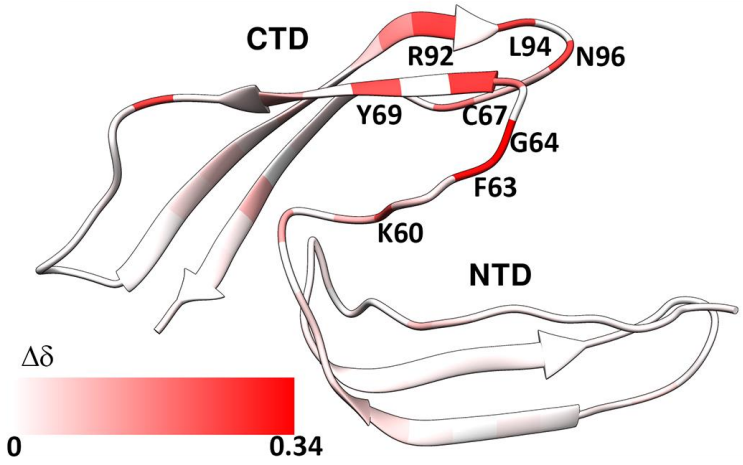

Figure A.5 PTPRZ-ac Peptide Induced Chemical Shift Changes in PTN
The magnitude of chemical shift perturbation is indicated by the color gradient on the ribbon diagram of PTN. The darker the red color, the stronger perturbation. The color scale is shown at the bottom.

Discussion

To find the answer why PTN can bind to non-proteoglycan forms of PTPRZ and regulates its function, we proposed that PTN is able to bind the PTPRZ core protein. The PTPRZ extracellular region contains a long unstructured stem region that has been found in two forms: the chondroitin sulfate glycosylated form and non-glycosylated form. In order to test if PTN can bind to the PTPRZ stem region core protein, we have analyzed the entire sequence of PTPRZ and mapped the electrical charges through the PTPRZ stem region. Since PTN is a strong positively charged protein (Figure A.6), we suspected that the region with the most negative charges on PTPRZ stem could be a PTN bind site. As shown in Figure A.2 we identified a region that is composed mostly of acidic amino acids such as aspartic acid and glutamic acid. Because this region is full of acidic amino acids, the charges of this region are exceptionally low. Thus, this negatively charged

region becomes our primary target to test PTN binding. According to the sequence, we have cloned, expressed and purified this acidic region into a short peptide (PTPRZ-ac peptide). And by using solution NMR titration, we have tested the binding affinity between PTN and the PTPRZ-ac peptide. The titration results lived up to the expectation that the binding affinity between PTN and PTPRZ-ac peptide is in ~30μM-80μM range. From the fitting curve data, we noticed that this binding between PTN and PTPRZ-ac peptide may not be one-to-one binding. We applied the Hill model to fitting the binding curve, and the Hill coefficient h was not 1 for most of the fitting curves from PTPRZ-ac peptide residues. In fact, the average value of h was ~ 2. This indicates that the one PTPZ1-ac peptide can possibly bind two PTN molecules.

Although this data showed that PTN can potentially bind to the stem region of PTPRZ core protein, there is still the need to develop an assay to test the binding in whole PTPRZ rather than just the short peptide. Unexpectedly, before we developed the experiment to confirm the hypothesis, the Noda's group revealed the mechanism of PTN induced PTPRZ dimerization. In their research, they found that instead of crosslinking PTPRZ, PTN acted as a neutralizer which neutralized the negative charges on PTPRZ. When the glycosaminoglycan's charges are neutralized by PTN, PTPRZ automatically formed an inactive dimer by itself. However, this does not explain why the non-proteoglycan form PTPRZ can also be deactivated PTN. We believe several mechanisms may be responsible for inducing PTPRZ crosslinking, including crosslinking through the core protein by proteins such as PTN and even crosslinking of C-mannosyl residues by lectins such as Galectin.

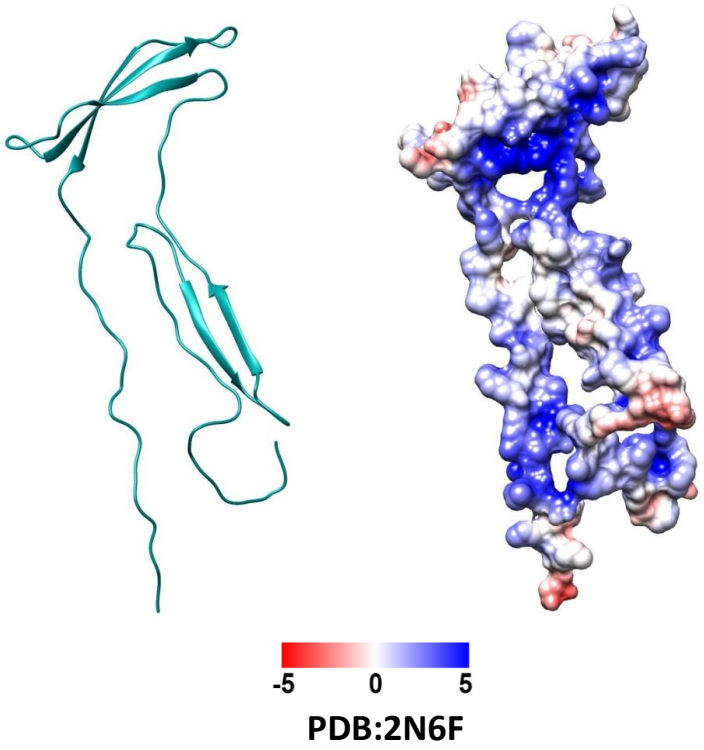

Figure A.6 Pleiotrophin Structure and Electrostatic Surface Potential
The structure of pleiotrophin is shown on the left side. And the right-side image shows the electrostatic surface potential mapped onto the ribbon diagram. The negative charge is labeled red and the positive charge is labeled blue. The electrostatic potential was calculated in absence of salt. The unit of potential is in kT·e-1.

APPENDIX B

PERMISSION FOR TABLE 1.1

SPRINGER NATURE LICENSE TERMS AND CONDITIONS

Jul 20, 2019

This Agreement between 320 E 14TH ST ("You") and Springer Nature ("Springer Nature") consists of your license details and the terms and conditions provided by Springer Nature and Copyright Clearance Center.

License Number	4633280872008
License date	Jul 20, 2019
Licensed Content Publisher	Springer Nature
Licensed Content Publication	Nature Reviews Molecular Cell Biology
Licensed Content Title	Integrin inactivators: balancing cellular functions in vitro and in vivo
Licensed Content Author	Daniel Bouvard, Jeroen Pouwels, Nicola De Franceschi, Johanna Ivaska
Licensed Content Date	May 30, 2013
Licensed Content Volume	14
Licensed Content Issue	7
Type of Use	Thesis/Dissertation
Requestor type	academic/university or research institute
Format	print and electronic
Portion	figures/tables/illustrations
Number of figures/tables/illustrations	1
High-res required	no
Will you be translating?	no
Circulation/distribution	<501
Author of this Springer Nature content	no
Title	Research assistant
Institution name	Arizona State University
Expected presentation date	Dec 2019
Order reference number	1
Portions	Table 1
Requestor Location	320 E 14TH ST 320 E 14TH ST TEMPE, AZ 85281 United States Attn: 320 E 14TH ST
Total	0.00 USD
Terms and Conditions	

APPENDIX C

PERMISSION FOR TABLE 1.2

JOHN WILEY AND SONS LICENSE TERMS AND CONDITIONS

Aug 03, 2019

This Agreement between 320 E 14TH ST ("You") and John Wiley and Sons ("John Wiley and Sons") consists of your license details and the terms and conditions provided by John Wiley and Sons and Copyright Clearance Center.

License Number	4641491321648
License date	Aug 03, 2019
Licensed Content Publisher	John Wiley and Sons
Licensed Content Publication	Immunology
Licensed Content Title	Integrin signalling and function in immune cells
Licensed Content Author	Yanbo Zhang, Hongyan Wang
Licensed Content Date	Mar 2, 2012
Licensed Content Pages	10
Type of use	Dissertation/Thesis
Requestor type	University/Academic
Format	Print and electronic
Portion	Figure/table
Number of figures/tables	1
Original Wiley figure/table number(s)	Table 1
Will you be translating?	No
Title of your thesis / dissertation	Research assistant
Expected completion date	Dec 2019
Expected size (number of pages)	1
Requestor Location	320 E 14TH ST 320 E 14TH ST TEMPE, AZ 85281 United States Attn: 320 E 14TH ST
Publisher Tax ID	EU826007151
Total	0.00 USD
Terms and Conditions	

APPENDIX D

PERMISSION FOR FIGURE 1.2

Brown, Carol
to me

Hello Di,

Permission is granted for the use of Fig 3 in the article detailed below in your PhD thesis only. Please include complete reference and copyright to Cold Spring Harbor Laboratory Press.

Best wishes for success with your thesis,

Carol C. Brown
Permissions Coordinator